

**APPLICATIONS OF ATOMIC MAGNETOMETRY IN
MAGNETIC RESONANCE IMAGING AND MAGNETIC
MOLECULAR SENSING**

A Dissertation

Presented to

the Faculty of the Department of Chemistry

University of Houston

In Partial Fulfillment

of the Requirements for the Degree

Doctor of Philosophy

By

Dindi S. Yu

August 2012

APPLICATIONS OF ATOMIC MAGNETOMETRY IN
MAGNETIC RESONANCE IMAGING AND MAGNETIC
MOLECULAR SENSING

Dindi S. Yu

APPROVED:

Dr. Shoujun Xu, Chairman
Dept. of Chemistry

Dr. Steven Baldelli
Dept. of Chemistry

Dr. Donald Kouri
Dept. of Chemistry

Dr. Jeremy May
Dept. of Chemistry

Dr. Yuhong Wang
Dept. of Biology

Dean, College of Natural Sciences and Mathematics

**APPLICATIONS OF ATOMIC MAGNETOMETRY IN
MAGNETIC RESONANCE IMAGING AND MAGNETIC
MOLECULAR SENSING**

An Abstract of a Dissertation
Presented to
the Faculty of the Department of Chemistry
University of Houston

In Partial Fulfillment
of the Requirements for the Degree
Doctor of Philosophy

By
Dindi S. Yu
August 2012

Abstract

Atomic magnetometry was presented as a technique suitable in magnetic resonance imaging (MRI) and magnetic molecular sensing. The magnetometer was based on nonlinear magneto-optical rotation promoted by Cs atoms in a vapor cell with anti-relaxation coating. A sensitivity of $150 \text{ fT/Hz}^{1/2}$ for dc magnetic fields was achieved. Applications of atomic magnetometry in MRI were demonstrated using the remote detection scheme. Using a gadolinium chelate as the pH contrast agent, we demonstrated the response as $0.6 \text{ s}^{-1}\text{mM}^{-1}$ per pH unit at the ambient magnetic field for the pH range 6–8.5. A stopped flow scheme was used to directly measure spin-lattice relaxation time T_1 to determine the relaxivity values. The unknown pH value of a solution was measured using only $50 \mu\text{M}$ of this contrast agent.

For magnetic molecular sensing, three key parameters were considered, namely sensitivity, spatial resolution and molecular specificity. To enhance the sensitivity of the magnetometer, the sample region was separated from the detection region. This arrangement lessened noise due to air turbulence and altered the design of the magnetic shields that would allow a gradiometer configuration. With an improved sensitivity of $80 \text{ fT/Hz}^{1/2}$, we demonstrated that 7000 streptavidin-coated magnetic microparticles could produce 650 pT predicting single particle detection during one second measuring time. Spatial information was obtained using a scanning magnetic imaging scheme. The spatial resolution was $20 \mu\text{m}$ with a detection distance of more than 1 cm . Using force-induced remnant magnetization spectroscopy, the molecular specificity was achieved. Magnetically labeled human CD4^+ T cells were used as an example. Quantitative correlation was shown, which could be used in human immunodeficiency virus diagnosis. Future works were discussed.

Contents

1	Introduction	1
2	Basic principles in nonlinear magneto-optical rotation	8
2.1	Linear magneto-optical rotation	9
2.1.1	The Faraday effect	9
2.1.2	Macaluso-Carbino effect	11
2.2	Nonlinear magneto-optical rotation	14
2.2.1	Saturation parameter	14
2.2.2	Optical pumping	15
2.2.3	Contributions to nonlinear magneto-optical rotation	17
2.2.4	Spin relaxation	20
2.3	Measurement of nonlinear magneto-optical rotation:Polarimetry	24
2.4	Nonlinear magneto-optical rotation with modulated light	25
2.4.1	NMOR with frequency-modulated light	25
2.4.2	NMOR with amplitude-modulated light	26
2.5	Intrinsic sensitivity	27
3	Cs-based magnetometer instrumentation	30
3.1	Atomic magnetometer for magnetic resonance imaging	31
3.1.1	Laser	31

3.1.2	Laser lock	31
3.1.3	Optical layout	33
3.1.4	Magnetic shielding	38
3.1.5	Paraffin-coated Cs cells	40
3.1.6	Internal coils and the piercing solenoid	42
3.1.7	Polarimeter	43
3.1.8	Electronics and communications system	44
3.1.9	Characterization of the instrument	48
3.2	Atomic magnetometer for magnetic particle sensing	55
3.2.1	Magnetic shields	55
3.2.2	Divider	56
3.2.3	Cs cell and internal coils	56
3.2.4	Quadrant photodiode	61
3.2.5	Characterization of the instrument	62
4	Applications of atomic magnetometry in magnetic resonance imaging	65
4.1	Motivation of the study	66
4.2	Detection schemes	70
4.2.1	Remote detection scheme	70
4.2.2	Radiofrequency detection scheme	72
4.3	Basic concepts in contrast MRI	74
4.3.1	Nuclear magnetic resonance phenomenon	74
4.3.2	Contrast magnetic resonance imaging	82
4.4	pH contrast in MRI	84
4.4.1	Experimental section	85
4.4.2	Matlab scripts	93

4.4.3	Results and discussion	102
4.5	Challenges and possible solutions	109
5	Applications of atomic magnetometry in magnetic molecular sensing	113
5.1	Motivation of the study	114
5.2	Magnetic properties of nanoparticles	117
5.2.1	Paramagnetism	118
5.2.2	Superparamagnetism	120
5.2.3	Ferromagnetism	121
5.3	Specific biomedical applications of magnetic nanoparticles	123
5.4	Cell-binding interactions	124
5.5	Experimental section	127
5.5.1	Scanning magnetic imaging	127
5.5.2	Cell binding	127
5.6	Results and discussion	128
5.6.1	Spatial resolution	128
5.6.2	Specificity	131
6	Conclusions	135
	Bibliography	139

List of Figures

1.1	General scheme for atomic magnetometry.	5
2.1	Linear Faraday effect. When light interacts with a medium in a magnetic field, its polarization is rotated by an angle φ	9
2.2	Level-shift effect. Optical rotation is due to the difference in resonance frequencies and refractive indices.	12
2.3	Optical pumping. Incident beam pumps spins on states with the same polarization as the light, leaving the rest as dark states. After the relaxation time, excited spins fall back to the ground state. Without relaxation, all spins will occupy $m_J = +1/2$ with the $\sigma+$ light.	16
3.1	Littman-Metcalf configuration. A piezoelectric element controls the mirror next to the diffraction grating.	32
3.2	a. DAVLL system. A portion of the beam is directed to another Cs cell immersed in a stronger magnetic field. The deviation from the tuned frequency is recorded by an amplifier and sent to the laser head. b. Iron shield for the Cs sensor.	34
3.3	Magneto-optical rotation in DAVLL.	35
3.4	Optical layout for Cs magnetometer.	36
3.5	Optical elements for the Cs magnetometer.	37
3.6	Double-pass arrangement of the beam provides optimum positioning of the cells and reduces heating requirement of the cell.	38
3.7	a. Magnetic shields. The ports are used for optical access, sample inlet, piercing solenoid and electrical connections. b. Styrofoam introduced in the shields to provide insulation.	39

3.8	a. Cs sensor on the cell holder. b. Cell holder has a gap in the middle to provide space for the sample holder. Picture view is upside-down. .	41
3.9	Internal coils comprise of a. Maxwell coil, b. Golay coil and; c)solenoid.	43
3.10	Electronics and communications system.	45
3.11	a. Circuit diagram for resistor load for power monitoring. b. Circuit diagram for ac-dc mixer.	46
3.12	LABVIEW interface for GPIB communication and frequency modulation.	47
3.13	a. Absorption of Cs sensor of the D1 transition. b. Highest signal was found to be from the hyperfine transition $F = 4 \rightarrow F' = 3$	50
3.14	In-phase and out-phase resonance signals of Cs magnetometer	51
3.15	Signal for instrument calibration at 100 pT, 0.1 Hz magnetic field. The in-phase signals correspond to A1 and B1, while the out-phase signals correspond to A2 and B2.	52
3.16	Temperature optimization. Highest sensitivity is achieved at 37 °C .	53
3.17	Comparison between stabilized and nonstabilized modes.	54
3.18	a. Three main components of Cs magnetometer: a sample inlet system, magnetic shields and optics enclosed by an aluminum enclosure. b. Internal magnetic caps with different port shapes.	57
3.19	a. Cross-section view of the internal part of magnetic shield. A plastic divider separates two regions of the shield. b. Comparison between the Cs sensor and a dime.	58
3.20	Technical design for coil holder located inside the shield.	59
3.21	Resistor box for the internal coils.	60
3.22	Quadrant photodiode for signal detection.	61
3.23	Magneto-optical resonances for calibrating magnetic fields.	62
3.24	Square signal from -0.1 V to 0.1 V.	63
3.25	Square signal produced from test calibration.	63
4.1	Nuclear magnetic resonance dispersion profiles of clinical contrast agents. Relaxivity is significantly high at lower magnetic fields.	69

4.2	Remote detection scheme for nuclear magnetic resonance detection. Three regions are pre-polarization, encoding and detection.	71
4.3	Pulse sequence of two-dimensional phase encoding. Four-step phase cycling is employed on the second $\pi/2$ pulse to overcome drifting noise.	72
4.4	RF detection scheme with atomic magnetometer A long solenoid provides a leading field B_0 for the sample nuclei, whereas the alkali atoms do not experience this field. A tunable ac field B_a is applied to the atomic magnetometer so that the atomic precession matches the nuclear precession in order to observe resonance.	73
4.5	Cross-sectional magnetic resonance image of two water-filled channels.	74
4.6	Zeeman splitting in nuclear spins. As magnetic field increases, the energy difference between sublevels increases and the number of parallel spins in the lower energy state also increases.	75
4.7	Larmor precession of nuclear spins. A radiofrequency field perpendicular to the magnetic field causes the nuclear spin moment to precess around the z-axis.	77
4.8	a. Spin-lattice (T_1) relaxation of nuclear spins. The recovery of magnetization along the z-axis is measured. b. After time T_1 , 63% of the magnetization returns to equilibrium. At $3T_1$, 100% of magnetization is recovered	78
4.9	a. Spin-spin (T_2) relaxation of nuclear spins. The magnetization along the xy plane is measured. b. After time T_2 the signal along the xy plane decays due to the dephasing of spins.	79
4.10	Free induction decay signal as detected by the radiofrequency coil. When the rf pulse is turned off, the signal along the transverse plane decreases.	80
4.11	Signal encoding using phase-encoding gradients. Signals along the y-positions are encoded by repeated scanning with different phase gradients. K-space records the signal in the presence of gradients.	81
4.12	Fourier transform of K-space results in a magnetic resonance image. .	82
4.13	Paramagnetic effect of gadolinium ion on water molecules. The inner-sphere experiences a net dipole from the paramagnetic gadolinium ion. This effect is transferred to the outer-sphere molecules.	83
4.14	a. Tecmag LF1 Apollo unit for sending rf pulses. b. Rf amplifier. . .	86

4.15	a. Saddle coil configuration. Optimum angle was $\theta = 60^\circ$; length/diameter = 1.41 b. Direction of current flow. c. Saddle coil on a Teflon tube.	88
4.16	Gradient coils wound around a plastic tube. Length and dimensions are measured based on the efficiency parameters.	89
4.17	Detection region of the remote detection scheme. A copper tube holds the sample to be measured. Detection axis is define by a bias field.	90
4.18	Remote detection setup. Sample is driven by a micropump (not shown) and is recycled back to the reservoir.	91
4.19	a.Stopped-flow scheme. b. Valve stops the flow in a systematic manner.	92
4.20	Pulse sequence for the stopped-flow experiment.	92
4.21	Flow profile of water in remote detection scheme. The magnetization is recorded from the maximum signal detected in the curve.	102
4.22	pH responses of $\text{Gd}(\text{TTHA})^{3-}$ and $\text{Gd}(\text{DTPA})^{2-}$. $\text{Gd}(\text{TTHA})^{3-}$ showed a non-monotonic response, a characteristic property for tumor sensing.	103
4.23	T_1 relaxation profiles of pure water and $100 \mu\text{M}$ $\text{Gd}(\text{DTPA})^{2-}$	104
4.24	Relaxivity of $\text{Gd}(\text{TTHA})^{2-}$ vs pH	106
4.25	pH response of $\text{Gd}(\text{TTHA})^{3-}$ at $50 \mu\text{M}$	107
4.26	One-dimensional MR images of a two-channel phantom (inset) with pure water and $150 \mu\text{M}$ $\text{Gd}(\text{TTHA})^{3-}$	108
5.1	Magnetic domains in a bulk material.	121
5.2	Magnetization as a function of applied magnetic field on a ferromagnetic system.	122
5.3	Structure of CD4. The four domains are numbered. CHO are glycosylation sites. TM is transmembrane segment; Cyt is the cytoplasmic portion.	125
5.4	Comparison between D-biotin (top) and D-desthiobiotin(bottom).	126
5.5	a. Scanning configuration for magnetic particle detection. b. Magnetic field profiles for two trials at different d values.	130
5.6	FIRMS profile for magnetically labeled CD4 cells.	132

List of Tables

2.1	Spin-destruction cross section (in cm^2) of potassium, rubidium and cesium	22
5.1	The results of fitted parameters in scanning magnetic imaging	129

Chapter 1

Introduction

Magnetic-based detection has been used extensively in medical diagnostics and biomedical research. In the scope of this dissertation, two distinct approaches are presented, namely detection of nuclear polarization such as in nuclear magnetic resonance (NMR) and magnetic resonance imaging (MRI), and sensing of functionalized magnetic particles such as in in vitro assays involving magnetic labels. Both fields were explored using atomic magnetometers.

The motivation in using atomic magnetometers for NMR and MRI is to perform detection in ambient magnetic field. While conventional methods are considered as powerful non-invasive techniques, the presence of a superconducting magnet maintained by cryogenics imposes cost and accessibility constraints. Moreover, the commonly used gadolinium-based contrast agents have much lower performance at high magnetic fields, which is normally compensated for by increasing the concentration of the gadolinium chelate. This has been reported to be potentially harmful especially

to patients with renal failures [1].

Low-field detection can address these issues. However, low-field measurements are typically challenging for conventional methods since the Faraday detection suffers at fields much less than 1 Tesla [2]. Thus, the use of the atomic magnetometer has been proposed as another detection method for NMR and MRI. Savukov and co-workers [3, 4] first presented the application of atomic magnetometers in nuclear magnetic resonance detection of water polarization. Xu and co-workers [5] first demonstrated the feasibility of atomic magnetometers in obtaining MR images of nuclear polarization at ambient magnetic field.

One of the unique aspects of low-field MRI is contrast enhancement. The spin-lattice relaxation time (T_1) of protons is significantly shortened at low field, resulting in higher MR signal and better image contrast. Thus, contrast agents perform better at low magnetic fields. In this dissertation, atomic magnetometer is used in order to take advantage of this feature. The instrument is also used to explore its capabilities in pH contrast and direct T_1 measurement.

In detecting magnetic particles, the purpose of using atomic magnetometers is to take advantage of the excellent sensitivity and long detection range. While surface techniques such as magnetic resonance force microscopy [6], magnetic exchange force spectroscopy [7] and the use of giant magneto-resistive sensors [8] can achieve the resolution of nanometers or microns, the detection range is also limited in nano or micron scale. This makes them inapplicable to applications in which the magnetic particles are far from the detectors, on the order of several millimeters to a few centimeters.

Yao and co-workers [9] first demonstrated the ability of atomic magnetometers in detecting magnetic particles at a long detection range (i.e. order of millimeters). In addition, they were able to resolve spatial information, quantify the amount of particles and obtain a two-dimensional magnetic image of the sample. In this dissertation, the atomic magnetometer is applied in order to provide spatial resolution using streptavidin-coated magnetic particles and to demonstrate its use in single particle detection.

A recent method discovered involving detection of magnetic particles with atomic magnetometers is force-induced remnant magnetization spectroscopy (FIRMS) [10]. In this technique, magnetic particles conjugated with ligand molecules are used to probe their corresponding receptor molecules. An external force is applied to the system in order to de-bind physisorbed molecules. This would allow measurement of the magnetization that is due to specific binding between the conjugated magnetic particles and receptor molecules. With this technique, molecular information can be obtained. In this dissertation, quantitative correlation between magnetic particles and human CD4+ T-cells is demonstrated using FIRMS. This is specifically helpful in human immunodeficiency virus (HIV) diagnosis.

The ability of atomic magnetometers to perform weak magnetic field measurements at ambient conditions is due to its all-optical configuration. A general scheme for atomic magnetometers is shown in Figure 1.1. Typically, two laser beams are used - one for polarizing the atomic spins and the other for monitoring (probing) the

Larmor precession of atoms in the magnetic field, which is given by Equation 1.1:

$$\omega = \gamma B \tag{1.1}$$

where ω is the Larmor frequency, γ is the gyromagnetic ratio of the alkali atom and B is the magnetic field. Alkali atoms in the vapor state are used because each has a single valence electron, which makes approximations simpler. The spins are polarized via optical pumping. Probing can be done by either using another laser beam orthogonal to the pumping beam, or using the same laser used for pumping. The rotation of light is probed and detected electronically. Source of magnetic field can be a calibration coil, the sample introduced, or both [11].

The main rival of atomic magnetometers is the superconducting quantum interference device (SQUID), in which weak magnetic fields are measured using a superconducting loop interrupted by two Josephson junctions. It has achieved a sensitivity of 1 fT/Hz^{1/2}. However, it still requires cryogenics, which adds additional cost burdens. Advances in atomic magnetometry, such as the use of effective and easily tunable diode lasers and new methods for enhancing atomic polarization times, has made the technique reach or even exceed the performance of SQUID. The spin-exchange relaxation-free (SERF) magnetometer is the most sensitive atomic magnetometer reported so far [12]. First presented by Allred and co-workers [13], this technique operates at very high cell temperature to overcome the relaxation due to spin-exchange collision, which is the collision between atoms that promotes decoherence of spins. Relaxation due to spin-destruction collision is overcome by introducing buffer gas into the sensor. From their experiment, the sensitivity obtained was 10 fT/Hz^{1/2}.

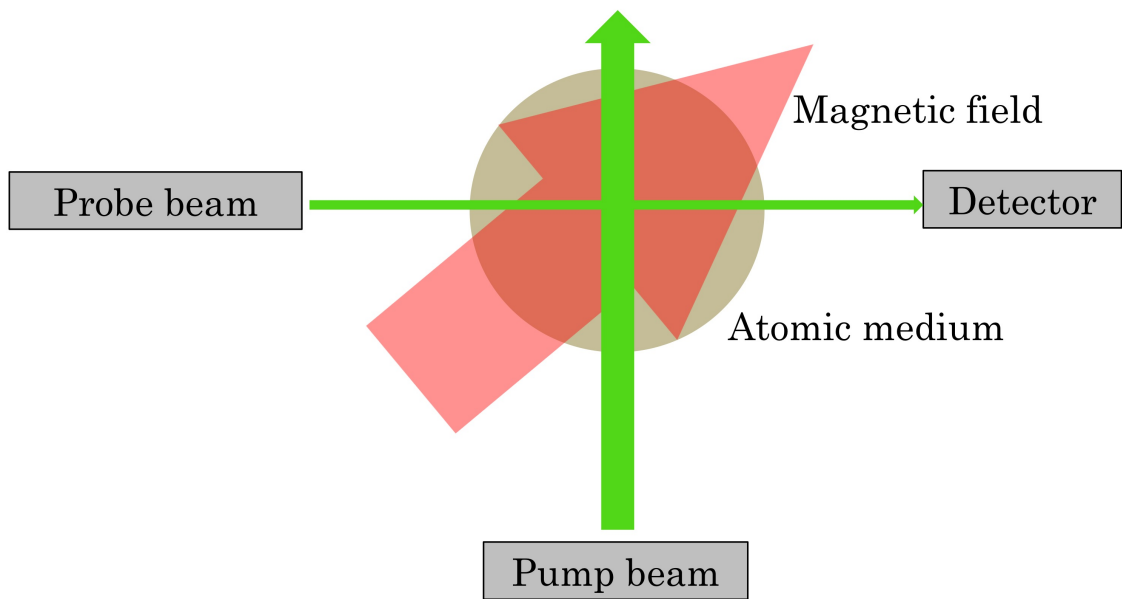


Figure 1.1: General scheme for atomic magnetometry.

SERF magnetometer can potentially achieve the sensitivity of ~ 1 aT/Hz^{1/2}. Modifications on SERF were done by Kominis and co-workers [14], in which they used two adjacent magnetometer channels to cancel the common magnetic field noise. They were able to achieve a sensitivity of 0.54 fT/Hz^{1/2} using a measurement volume of 0.3 cm³. A major fallback of this technique is the use of ferrite oven, which highly contributes to the over-all noise of the magnetometer, as it introduces excess magnetic field in the detection region. Potential applications of SERF magnetometer include sample magnetization measurements, especially rock samples, nuclear magnetic resonance (NMR) detection [15, 16] and high performance magnetoencephalographic imaging [17].

While the SERF magnetometer has remarkable sensitivity, its high temperature requirement limits its applications to biological samples that may denature if placed in the vicinity of high-temperature sensors without thermal insulation. In this dissertation, we present an atomic magnetometer that is based on nonlinear magneto-optical rotation, which operation does not involve elevated temperature conditions. A detailed discussion can be found in the next chapter. Briefly, this technique is based on the interaction of alkali atoms contained in a paraffin-coated cell with low-powered light. The frequency of the beam is modulated, and resonances in optical rotation are observed when the modulation frequency is twice the Larmor precession frequency. The use of frequency-modulated light reduces the noise level significantly. A bias magnetic field B_{bias} stronger than the sample field is applied to define the detection axis. Based on the relationship given in Equation 1.2,

$$\omega_M \approx 2g\mu(B_{bias} + B_{sample}) \quad (1.2)$$

where g is the atomic gyromagnetic ratio and μ is the Bohr magneton, the magnetic field of the sample B_{sample} can be deduced. This technique has been explored in radio-frequency detection [18], magnetic resonance imaging [5, 19], and magnetic particle detection [20].

As an overview, this dissertation presents detailed discussion on nonlinear magneto-optical rotation phenomenon (Chapter 2), atomic magnetometer instrumentation (Chapter 3), the results of MRI studies (Chapter 4), and the results in detecting magnetically labeled cells (Chapter 5). Lastly, summary, conclusions and future works are presented in Chapter 6.

Chapter 2

Basic principles in nonlinear magneto-optical rotation

This chapter provides some basic concepts in magneto-optical rotation. The mechanisms contributing to both linear and nonlinear rotation are presented. Other important information, which include saturation parameter, optical pumping, sources of relaxation, measurement of magneto-optical rotation, and intrinsic shot-noise sensitivity are also discussed.

2.1 Linear magneto-optical rotation

2.1.1 The Faraday effect

Michael Faraday presented the first experimental evidence of the interaction of light and magnetic field in a medium [21]. Using a light source, a polarizer and polarimeter, a medium, and a controllable magnetic field, he observed that upon interaction of light with the magnetized medium, the plane of polarization of light rotated by an angle proportional to the magnetic field (Figure 2.1).

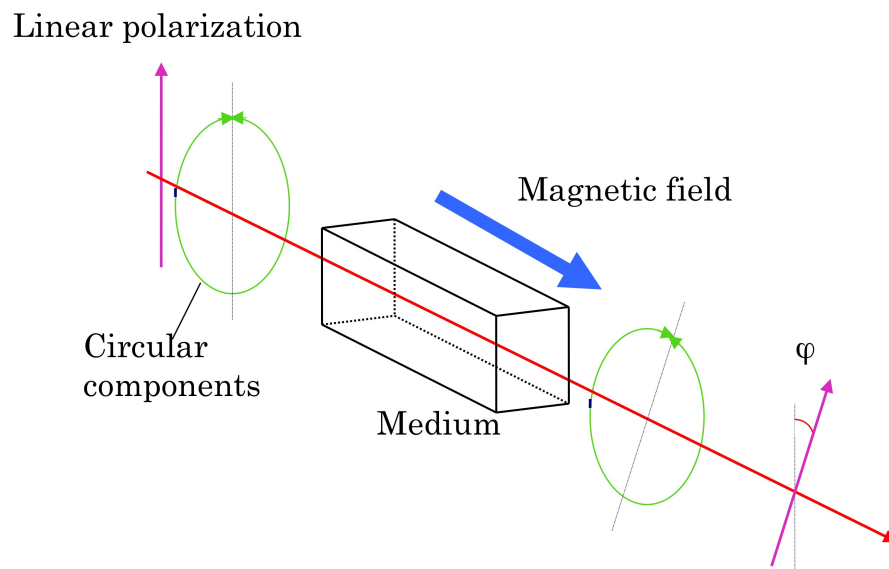


Figure 2.1: Linear Faraday effect. When light interacts with a medium in a magnetic field, its polarization is rotated by an angle φ .

In physical terms, Faraday effect can be explained by considering the linearly polarized light as a superposition of two circularly polarized components. Circular coordinates can be transformed into the Cartesian basis using the following equations:

$$\hat{E}_x = \frac{1}{\sqrt{2}}(\hat{E}_+ + \hat{E}_-) \quad (2.1)$$

$$\hat{E}_y = \frac{-i}{\sqrt{2}}(\hat{E}_+ - \hat{E}_-) \quad (2.2)$$

where \hat{E}_x and \hat{E}_y are the unit vectors representing light polarized along x and y, respectively, and \hat{E}_+ and \hat{E}_- are the vectors representing right- and left-circularly polarized light, respectively.

Suppose the light is y-polarized and the wavevector \mathbf{k} propagates along z. The electric field vector \mathbf{E} can be written as

$$\mathbf{E} = E_0 \hat{E}_y \cos(kz - \omega t) \quad (2.3)$$

$$\mathbf{E} = -\frac{iE_0}{2\sqrt{2}}(\hat{E}_+ e^{-i(kz - \omega t)} - \hat{E}_- e^{-i(kz - \omega t)}) + c.c., \quad (2.4)$$

where E_0 is the amplitude of the electric field, ω is the frequency of light and c.c. is the complex conjugate. The wavenumber k is given by

$$k = \frac{2\pi}{\lambda} = \frac{\eta\omega}{c} \quad (2.5)$$

where λ is the wavelength of light and η is the complex refractive index given by

$$\eta = n + i\kappa. \quad (2.6)$$

The real part of the complex refractive index is the refractive index n , which is associated to the dispersion of the medium, while the imaginary part is given by the absorption coefficient κ , which describes its absorptive properties.

For $n_+ \neq n_-$, each component travels at different velocity, which causes a difference in the phase of the beam, as given by

$$\varphi = \frac{\omega l}{c}(n_+ - n_-) \quad (2.7)$$

where φ leads to rotation of the plane of polarization by the angle ϕ

$$\phi = \frac{\varphi}{2}. \quad (2.8)$$

In Faraday effect, the change in refractive indices is caused by the introduced magnetic field.

2.1.2 Macaluso-Carbino effect

Domenico Macaluso and Orso Carbino investigated the Faraday effect in atomic gases fifty years after Faraday's discovery [22]. They conducted a similar experiment as Faraday's, except that their source of light was the sun and their medium was atomic sodium atoms produced by a flame. They also used a diffraction grating to sort out frequencies from the sunlight. From their experiment, they observed that the rotation of light was significantly enhanced when they tuned the frequency of the incident light near an atomic resonance frequency in sodium.

Three mechanisms have been postulated to explain the Macaluso-Carbino effect namely, level-shift effect, hyperfine mixing and paramagnetic effect.

Level – shift effect

As explained by Voigt in 1898 [23], the Macaluso-Carbino effect is based on Zeeman splitting of energy levels. Consider the simple $F=1 \rightarrow F'=1$ transition (Figure 2.2). The linearly polarized light is considered as a combination of right- and left- circular components represented as σ_+ and σ_- , respectively, Without the presence of magnetic field, the ground state M sublevels are equal; therefore the resonance frequencies and the refractive indices of the circular components are equal.

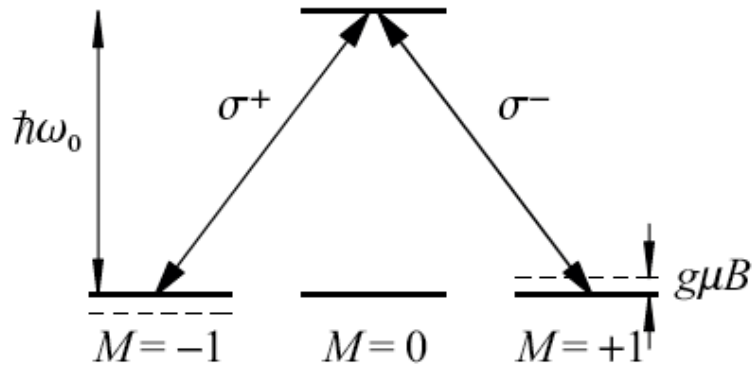


Figure 2.2: Level-shift effect. Optical rotation is due to the difference in resonance frequencies and refractive indices.

When a magnetic field is applied to the atomic medium, the degeneracy of these sublevels is removed, resulting in a change in the resonance frequencies for the two circular polarizations. As a result, the plane of polarization rotates through an angle $\varphi = \pi(n_+ - n_-)l/\lambda$ where l is the length of the sample and λ is the wavelength of light.

In addition to change in refraction (circular birefringence), the absorption properties also become different (circular dichroism). Therefore, light passing through the medium becomes elliptically polarized.

For a monochromatic light and zero frequency detuning from the resonance, the optical rotation can be estimated using the equation:

$$\varphi \simeq \frac{2g\mu B/\hbar\Gamma}{1 + (2g\mu B/\hbar\Gamma)^2} \frac{l}{l_0} \quad (2.9)$$

where g is the Lande factor, μ is the Bohr magneton, Γ is the linewidth and l_0 is the absorption length [24]. This approximation considers the resonance value of the imaginary part of the refractive index (responsible for absorption). The dependence of the optical rotation on the magnitude of the magnetic field follows the Lorentzian model with a characteristic dispersion-like shape: ϕ is linear with B at small values of the field, highest at $2g\mu B = \hbar\Gamma$, and falls off in large magnetic fields.

Hyperfine mixing

The hyperfine mixing mechanism explains the Macaluso-Carbino effect in atoms with non-zero nuclear spins. Magneto-optical rotation near the resonant frequency of the atoms is observed in a similar way as the level-shift effect, except that the hyperfine states of the atom couple with each other [25]. This can be approximated by the equation:

$$\varphi \simeq \frac{g\mu B}{\Delta_{hfs}} \frac{l}{l_0} \quad (2.10)$$

Unlike the level-shift effect, it only leads to a change in the refractive indices and not the resonance frequencies. The profile is dispersion-like around the hyperfine components of the transition.

Paramagnetic effect

The change in the refractive index depends on the population of the ground-state Zeeman sublevels according to the Boltzmann distribution. For gaseous systems, this effect is relatively small. However, it can be enhanced by creating unequal population distribution via optical pumping, which is a nonlinear process [24].

2.2 Nonlinear magneto-optical rotation

Nonlinear magneto-optical rotation (NMOR) is a typical nonlinear optical effect. It is a process that depends on the intensity of polarized light that propagates through a medium in a magnetic field. NMOR was first measured using laser by Gawlik and co-workers in 1974 [26]. They found out that NMOR signals as a function of magnetic field had a distinct feature. Compared to the Doppler-broadened linear magneto-optical rotation (LMOR) signal, the new signal was narrower than Doppler widths and the rotation of polarization plane depended on the light intensity.

2.2.1 Saturation parameter

Nonlinear optical condition is achieved when there is saturation of the upper-state energy level. This is normally done via the process called *optical pumping*. Saturation parameter is a useful tool to describe the nonlinear process near resonance [27]. Generally, the saturation parameter can be written as

$$\kappa = \frac{\textit{excitation rate}}{\textit{relaxation rate}}. \quad (2.11)$$

When $\kappa_1 \ll 1$, spontaneous emission dominates and the lower sublevels are mostly populated. For $\kappa_1 \gg 1$, atoms experience regular Rabi oscillations (cyclical absorption and emission of photons) at a rate much faster than spontaneous emission and the average population of the upper and the lower state become equal.

Nonlinear processes are known to occur using high intensity beams. However, earlier studies have shown that these processes can still occur even using weak-powered light, such as the conventional spectral lamps [28].

2.2.2 Optical pumping

Nonlinear condition can be achieved via optical pumping. Optical pumping is a process that creates population distribution among Zeeman sublevels in order to achieve a higher-order atomic spin coherence at the ground state. This entire redistribution promotes optical anisotropy.

Certain lower energy sublevels absorb light more strongly than others. Thus, the weakly absorbing sublevels will tend to be more populated than the strongly absorbed sublevels. Using polarized light, uneven population distribution between hyperfine states is produced. Consider an atom with two hyperfine ground-state levels (1,2) and one excited state level (3). If the incident light resonant to the transition between level 1 and level 3 is used, all of the atoms from level 1 will be pumped out, while all of the atoms in level 2 will remain in their state since the pumping light is off-resonance for the transition $2 \rightarrow 3$. The atoms can relax back to either of the two ground-state levels. Eventually, in the absence of relaxation, all

atoms will eventually be pumped into level 2.

Any depolarization of the excited state by collisions (collisional mixing) will decrease the efficiency of the process. At higher buffer gas pressures, depolarization of excited state due to collision is almost complete and almost no repopulation can occur, though the ground state may still be strongly polarized by depopulation. This is because the ground state depolarization cross section is 10^{10} times smaller than the excited state depolarization cross sections.

A general picture of optical pumping is shown in Figure 2.4.

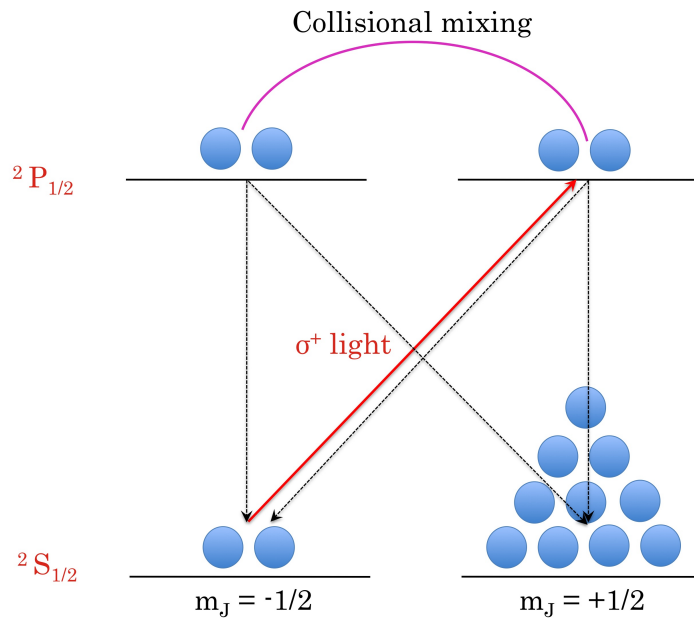


Figure 2.3: Optical pumping. Incident beam pumps spins on states with the same polarization as the light, leaving the rest as dark states. After the relaxation time, excited spins fall back to the ground state. Without relaxation, all spins will occupy $m_J = +1/2$ with the $\sigma+$ light.

2.2.3 Contributions to nonlinear magneto-optical rotation

Broadly speaking, nonlinear magneto-optical rotation is a process in which both the properties of the medium and light are changed. Atomic population is changed via optical pumping, and polarization of light is altered via optical probing. Pumping and probing can be done using a single beam. However, the mechanisms will be easily understood if we consider two separate beams.

Two primary mechanisms behind nonlinear magneto-optical rotation were identified by Barkov and co-workers [29]: the Bennett-structure formation and Zeeman coherences. The primary determining factor between these two effects is the magnitude of magnetic field B_{max} at which rotation is maximum. B_{max} is related to a linewidth Γ :

$$B_{max} = \frac{\hbar\Gamma}{2g\mu} \quad (2.12)$$

For Bennett-structure effects, the smallest linewidth that can be obtained corresponds to the natural width of the atomic transition ($\sim 2\pi \times 1 - 10$ MHz). For coherence effects, linewidth depends on the rate of atomic depolarization, which smallest value was found to be $\sim 2\pi \times 1$ Hz.

Bennett – structure effects

If we consider the $F=1/2 \rightarrow F'=1/2$ transition, the coherence effects can be ignored. In this transition, the excited spins relax back to levels that are not necessarily ground states. Atoms in the $|M = \pm 1/2\rangle$ states will be depopulated, creating Bennett holes. When a magnetic field is applied, the sublevels are split into more resolved energy levels or Zeeman sublevels and therefore shifts the Bennett-structure

features of the dispersive profile of light. As the weak probe beam interacts with the medium, the refractive indices of $\sigma+$ and $\sigma-$ are changed. As an effect, rotation of the plane of polarization of light is observed, since the difference between the real part of the refractive indices $Re(n_+ - n_-)$ is proportional to the rotation of light φ .

Coherence effects

When considering coherence effects, the mechanism of NMOR can be separated into three stages, provided that a sufficiently low light was used. The first step is the polarization of atoms via optical pumping, followed by the evolution of the atomic polarization. The last step involves optical rotation of light, in which the atoms are probed with either another weak beam or same beam used for pumping. These processes can occur simultaneously and continuously. These events result in narrower linewidths, therefore promoting higher small-field Faraday rotation.

The mechanism involving coherence effects is due to the coherent superposition of Zeeman sublevels when a linearly polarized light propagates along the direction of a chosen quantization axis. In the presence of magnetic field, these Zeeman sublevels are shifted, which results in the evolution of the relative phase between the component states of the coherent superposition. Thus, evolution of atomic coherence and relaxation of these coherences are considered to understand coherence effects.

The evolution of atomic coherences depends on the intensity of light. When the light used is sufficiently low, the effect of optical field can be ignored. Consider atoms with total angular momentum $F = 1$. In its initial state, the atoms are unpolarized and the atomic states can be considered as an incoherent mixture of three different

states:

$$|z \rangle = |M = 0 \rangle, \quad (2.13)$$

$$|x \rangle = \frac{1}{\sqrt{2}}(|M = 1 \rangle - |M = -1 \rangle), \quad (2.14)$$

$$|y \rangle = \frac{1}{\sqrt{2}}(|M = 1 \rangle + |M = -1 \rangle). \quad (2.15)$$

Suppose that a beam propagates along the z-axis and its frequency correspond to a transition to a $F' = 0$ state. The z-state can only be polarized by z-polarized light, leaving the other states unpolarized. Similarly, the other two states (which are coherent superpositions of the Zeeman sublevels) can only absorb x-polarized light (for the x-state) and y-polarized light (for the y-state).

If the laser light is x-polarized, spins in the x-state will be excited, leaving the atoms in the "dark" y-state and z-state. The medium is now transparent for the x-polarized light but can still go transitions when an orthogonal beam is applied. Atoms are now in the aligned state and possess linear dichroism and birefringence.

When the light used is of higher intensity, alternating current Stark shift or the shift of energy caused by electric field has a contribution to the evolution of atomic coherences. If the alignment of atomic states is parallel to the electrical field, ac Stark shift will not be observed. However, in the presence of magnetic field along the propagation of light, the bright and dark states will undergo superposition, which result in quantum beats. These quantum beats produce atomic orientation along the propagation axis, which increases with time and cause optical rotation due to circular birefringence.

2.2.4 Spin relaxation

Coherence effects have been found to cause greater optical rotation than the Bennett-structure effects. Barkov and co-workers [29] observed that the rotation due to coherence effects was $\sim 10^4$ times larger than that of the linear Macaluso-Carbino effect. Therefore, anything that destroys coherence, and consequently the over-all spin polarization, has a major effect on the magneto-optical signal being measured.

When experimental parameters such as pumping light and external fields are maintained, the optically pumped vapor will eventually reach a steady state. If one of the parameters is changed, the system will relax to a new steady state after a certain time. Relaxation can be caused by many mechanisms. Some of the most common are spin-exchange collisions, spin-destruction collisions and wall collisions. Optical pumping itself can be therefore considered as a relaxation mechanism in which a collection of atoms relaxes to a polarized state because of repeated collisions with the polarized photons of the pumping light [30].

Relaxation due to spin – exchange collisions

When two atoms collide, the orientation of the individual spins may change while preserving the total angular momentum of the system. For example, if atoms A and B are oppositely polarized, a spin-exchange collision reverses the spins:



This kind of interaction is typical to alkali metal atoms. The collisions occur so fast that only the electron spins are changed and not the nuclear spins. Thus, the hyperfine state of the atoms can be changed while preserving the total angular

momentum of the colliding pair. In effect, spin-exchange collisions destroy coherence in ensembles of polarized atoms precessing in the presence of a magnetic field.

For vapor of alkali atoms, the time of spin-exchange collisions is given by

$$T_{se} = (\sigma_{se}n\bar{v})^{-1} \quad (2.17)$$

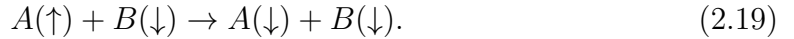
where σ_{se} is the spin-exchange cross section (2×10^{14} cm² for alkali atoms), n is the vapor density, and \bar{v} is the average relative velocity given by the Maxwell-Boltzmann distribution:

$$\bar{v} = \sqrt{\frac{8RT}{\pi m}} \quad (2.18)$$

where R is the ideal gas constant, T is the temperature, and m is the molar mass of the atoms.

Spin – destruction collisions

In a spin-destruction collision, the total spin angular momentum is not preserved. This type of collision may occur in alkali atoms or with the buffer and quenching gases. Such collisions between alkali atoms transfer spin angular momentum to the rotational angular momentum of the colliding pair of atoms. It can be represented using the equation below:



Wu and co-workers [31] explained a theory for the spin-rotational coupling. In the excited state, the electrons are easily depolarized upon collisions with noble gas atoms. In contrary, atoms in the ground state collide with noble gas atoms several

times before losing polarization. It is for this reason that noble gas is used to slow down alkali diffusion to the walls of the cell.

This interaction is significant in polarized alkali atoms. Table 1 shows a summary of spin-destruction cross section σ_{SD} of alkali atoms due to interatomic collisions and collision with gases [30].

Alkali Metal	Potassium	Rubidium	Cesium
σ_{SD}^{self}	1.0E-18	1.6E-17	2.0E-16
σ_{SD}^{He}	8.0E-15	9.0E-24	2.8E-23
σ_{SD}^{Xe}	1.8E-19	2.0E-19	2.3E-19
$\sigma_{SD}^{N_2}$	7.9E-23	1.0E-22	5.5E-22

Table 2.1: Spin-destruction cross section (in cm^2) of potassium, rubidium and cesium

Wall collisions

When an alkali atom hits the glass surface of the cell wall, it gets adsorbed for a finite time and released back into the cell volume. The atom interacts with the large local and magnetic fields produced by ions and molecules on the glass. These fields are affected by the motion of an atom on the surface and are changed over time. Adsorption happens shortly. However, when the atom is released back to the volume, polarization is completely randomized. It is for this reason that wall collision has a significant contribution to the over-all spin-relaxation that should be suppressed.

There are two common ways to decrease the depolarizing effect due to wall collision namely, the use of surface coatings and the introduction of buffer gas. Surface coatings are anti-relaxation coatings that cover the surface and prevent the alkali

atoms from directly interacting with the glass walls. These coatings must be chemically inactive and can ideally allow the atoms to bounce off the surface thousands of times without depolarizing.

In anti-relaxation-coated vapor cells, there are two mechanisms that may occur namely, the transit effect and the wall-induced Ramsey effect. In the transit effect, pumping and probing occur with the single pass of light, since atoms traverse along the beam. In the wall-induced Ramsey effect, atoms that are pumped leave the light beam for a certain amount of time, then return to the volume after colliding with the wall of the coated cell to interact with the probing light. Thus, the time between the pumping and probing can be much longer, leading to ultranarrow linewidths, which signifies enhanced sensitivity. In addition, the maximum optical rotation due to this effect occurs at much lower magnetic field than that of the transit effect [32].

The use of high buffer gas increases the time it takes for the atoms to reach the cell wall, provided that the atoms' mean free path λ_t in the buffer gas is comparable to or less than the dimensions of the cell. The classical diffusion constant is related to the "transport" mean free path λ_t and the mean atomic velocity \bar{v} by the equation:

$$D = \frac{\lambda_t \bar{v}}{3}. \quad (2.20)$$

While buffer gas suppresses wall collision, it is important to take note that it increases the spin-destruction collision. Therefore, it is important to optimize the buffer gas pressure in order to minimize the effect due to spin-destruction collisions.

2.3 Measurement of nonlinear magneto-optical rotation: Polarimetry

In order to succeed in employing NMOR methods, a precision polarimeter should be present [24]. Two ways of polarimetry have been in use: the balanced polarimeter and the use of polarization modulator.

In a balanced polarimeter, the sample to be measured is situated in between a polarizer and a beam splitter (analyzer) 45° from each other. From this configuration, the rotation of light can be obtained from the equation:

$$\varphi = \frac{I_1 - I_2}{2(I_1 + I_2)} \quad (2.21)$$

where I_1 and I_2 are the light intensities detected in the two output channels of the analyzer [24].

In a polarimeter that involves a polarization modulator, a Faraday rotator is placed between the polarizer and analyzer. The rotator modulates the polarization at a frequency of 1 kHz. The rotation angle is measured via the first harmonic of the signal from a photodetector in the dark channel of the analyzer. This configuration allows measurement of signals at high frequencies, which reduce sensitivity to low frequency-noise.

The intensity signal in the dark channel is given by the equation:

$$I_s(t) \simeq \chi I_0 (r_e + \frac{1}{2} \alpha_m^2 + \varphi^2) + 2\chi I_0 \alpha_m \varphi \sin \omega_m t - \frac{1}{2} \chi I_0 \alpha_m^2 \cos 2\omega_m t \quad (2.22)$$

where χ is the coefficient defined by absorption and scattering of light by the atomic

vapor cell, I_0 is the total photon flux of the linearly polarized light (in photons per unit time) transmitted through the polarizer, r_e is the polarizer/analyzer extinction ratio, and α_m and ω_m are polarization modulation amplitude and frequency, respectively [24].

Based on this equation, the sensitivity of an ideal polarimeter is given by the equation below:

$$\delta\varphi_s \simeq \frac{1}{2\sqrt{\chi I_0 T}}. \quad (2.23)$$

2.4 Nonlinear magneto-optical rotation with modulated light

2.4.1 NMOR with frequency-modulated light

In measuring rotation, low-frequency noise limits the sensitivity of polarimeters if modulation is not present. This limitation can be overcome by some form of fast modulation. Though using a polarization modulator reduces the sensitivity of the polarimeter to low-frequency noise, it is still sensitive to drifting zero problem, which is a signal detected from changes between relative rotation of the polarizer and analyzer or an alteration in the birefringence of optical elements. This signal cannot be distinguished from the signal due to rotation from the atoms.

This limitation can be overcome using the frequency modulation technique [33]. Additional optical elements, such as the Faraday modulator, are not needed. The

drift zero problem and other unwanted rotations are not sensitively detected.

In the frequency modulation technique, the piezo actuator of a diode laser is modulated. As the laser frequency is modulated, the rate of optical pumping differs with the laser detuning from the atomic transition. The optical pumping rate changes periodically as dictated by the modulation frequency ω_m . The atomic polarization also changes periodically but is also dependent on the magnetic field. When the atomic polarization alignment is transverse to the magnetic field, the change occurs at frequency $2\omega_L$. If periodicity of optical pumping synchronizes with Larmor precession, a resonance is observed and the atoms are pumped into aligned states rotating at ω_L . This results in dispersive resonances in optical rotation detected as the signal at the corresponding harmonic ω_m [24].

2.4.2 NMOR with amplitude-modulated light

An alternative to the use of frequency-modulated light is the use of amplitude-modulated (AM) light. First experiments with AM in NMOR were performed by Gawlik and co-workers [34] and Balabas and co-workers [35]. Using AM light, macroscopic polarization of a medium can be generated, which occurs when the frequency of light modulated is synchronized with the Larmor precession. The pumping rate is modulated by periodic changes of the light intensity. The rotation signals show uncommon features such as narrowed non-Lorentzian line shapes and multicomponent resonances.

This method produce ultranarrow resonances at zero magnetic field and at higher

fields. Thus, it can be used for magnetic fields ranging from the microgauss level to the Earth field with sensitivity approaching 10^{-11} G/Hz.

Compared to FM NMOR method, the use of AM light minimizes distortions due to possible spurious AM of laser light and the ac Stark-effect shifts. NMOR with AM can be used when it is difficult or impossible to change the light-source frequency. It also provides additional parameter in optimizing the modulation wave for better control of the atomic dynamics and observed signals.

2.5 Intrinsic sensitivity

According to the uncertainty principle, the intrinsic sensitivity of an atomic magnetometer follows the equation:

$$\delta B = \frac{1}{\gamma\sqrt{N\tau t}} \quad (2.24)$$

where γ is the gyromagnetic ratio, N is the number of atoms, τ is the coherence lifetime (time the spins maintain their polarization in the absence of pumping) and t is the measuring time [36]. From this equation, it can be noted that the coherence lifetime and density of atoms are the primary factors affecting the sensitivity of a magnetometer.

As mentioned earlier, anti-relaxation molecules enhances ground state atomic coherence, and so is the coherence lifetime. Commonly used anti-relaxation agent is paraffin, a long-chained hydrocarbon compound [32]. With paraffin, a coherence time as long as 1 s has been observed, which indicates that the atomic coherence survives

thousands of collisions between the atoms and the cell wall. A sensitivity of ~ 0.3 fT/Hz^{1/2} was projected for a rubidium cell of 500 cm³. A recent improvement done by Balabas and co-workers [37] used the alkene 1-nonadecene for cell-coating instead of the conventional alkane coating. Results showed that this alkene has a coherence time of 60 s and can allow up to 10⁶ alkali-metal-wall collisions before relaxation of spins occurs, which demonstrates an improvement over traditional coatings by about a factor of 100. In addition, the coating was tested under room temperature conditions, which makes the magnetometer to be more practically useful.

From a purely experimental point of view, the magnetometer sensitivity depends on the signal-to-noise ratio (S/N) of the Zeeman resonance signal as well as the linewidth,

$$\delta B = \frac{\Delta B}{S/N}. \quad (2.25)$$

Therefore, the magnetic field noise needs to be reduced and the optical detection system needs to be stable. Diode lasers are stable and can be easily tuned, which allows measurements of optical rotation with low noise. The resonance signal is typically enhanced by increasing the number of atoms in the spin ensemble by increasing the vapor density or using a larger vapor cell. But since the rate of depolarization scales with density, traditional sensitive magnetometers utilize large vapor cells and operated at low density, at or near room temperature. To overcome this issue, Romalis and co-workers [14] used a high-pressure buffer gas in order to minimize the spin-destructive collisions. Helium is often used. At high buffer gas pressure, the alkali atoms need a much longer time to reach the cell wall, minimizing the number of wall collisions. This is essential in order to achieve the spin-exchange relaxation-free

(SERF) condition in a near-zero magnetic field. Paraffin coating is not applicable because the cell temperature is higher than its melting point. The SERF atomic magnetometer has achieved a sensitivity of $\sim 0.5 \text{ fT/Hz}^{1/2}$ with an effective cell size of only 0.3 cm^3 .

Chapter 3

Cs-based magnetometer instrumentation

In this chapter, the details and characterization of a compact and sensitive cesium magnetometer are presented. This instrument was used for enhanced contrast magnetic resonance imaging studies. We also present another magnetometer, which was used for magnetic particle sensing. New features were added to the instrument, which caused an increase to the over-all sensitivity of the magnetometer.

3.1 Atomic magnetometer for magnetic resonance imaging

3.1.1 Laser

A diode laser (New Focus, model 7018) tuned to the D1 transition of Cs (894.95 nm) is used. There are two modes of operation for the diode laser: the constant current mode and the constant power mode. Constant-current mode results in narrower laser linewidth while constant-power mode results in the lower intensity fluctuations. We used the constant current mode for obtaining the absorption spectra of Cs, while we used the constant power mode for all the measurements.

The laser follows the Littman-Metcalf configuration. (Figure 3.1). The piezoelectric component precisely adjusts the angle of the mirror to adjust the wavelength of the laser beam. Frequency modulation is done by driving a piezoelectric transducer in the laser with a function generator (Stanford Research DS345).

3.1.2 Laser lock

Due to temperature, current and mechanical noises, the frequency of the beam from the laser tends to drift from the original set value. To avoid frequency drifts, we used a lock system called dichroic atomic vapor laser lock (DAVLL) [38].

A general scheme for the DAVLL is shown in Figure 3.2a. In this system, the beam is directed towards a Cs cell with larger size housed in a magnetic shield

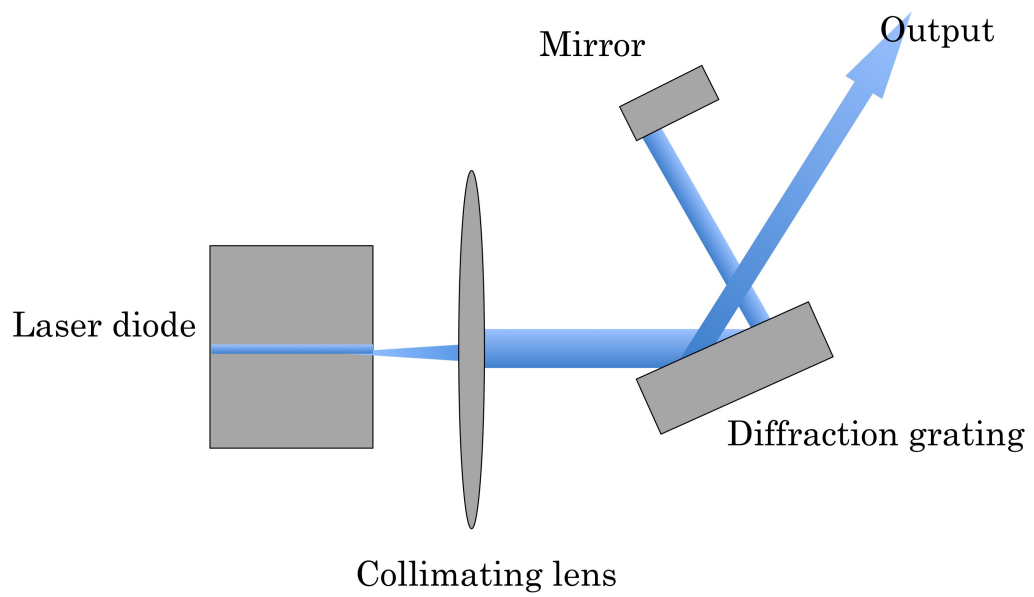


Figure 3.1: Littman-Metcalf configuration. A piezoelectric element controls the mirror next to the diffraction grating.

(Figure 3.2b.) containing a high-field magnet. As it interacts with the Cs atoms, the beam undergoes linear magneto-optical rotation. An elliptically-polarized beam is produced. Then, the beam passes through a quarter-wave plate and a polarization prism. The final beams are fed into two photodiodes, which voltage are amplified by a lock-in amplifier (Stanford Research SR530).

The characteristic DAVLL signal is shown in Figure 3.3. The quarter-wave plate is adjusted to change the phase of the beam so to maintain the zero-crossing point. The differential signal at this point is fed to the piezoelectric element of the laser, which maintains the frequency of the beam at the locking point [39].

3.1.3 Optical layout

Figure 3.4 shows a schematic of the optical layout. The laser beam first passes through a neutral density filter, then through a 5% beam sampler to be used by the entire optical system. After this, another 5% beam sampler is placed for power monitoring. This small portion of light is directed to a photodiode, which output is amplified and fed back to the laser for constant power operation. Another 5% beam sampler is placed for the laser lock system. Then, the rest of the beam passes through a 50 – 50 beam splitter to supply beams for each magnetometer.

In each magnetometer, the incoming beam from the beam splitter passes through a Glan polarizer to set the initial polarization of the beam(Figure 3.5). Then, it hits the mirror to direct the beam into the sensing region. The beam hits another mirror located at the back of the Cs cell holder and is reflected back to a Rochon

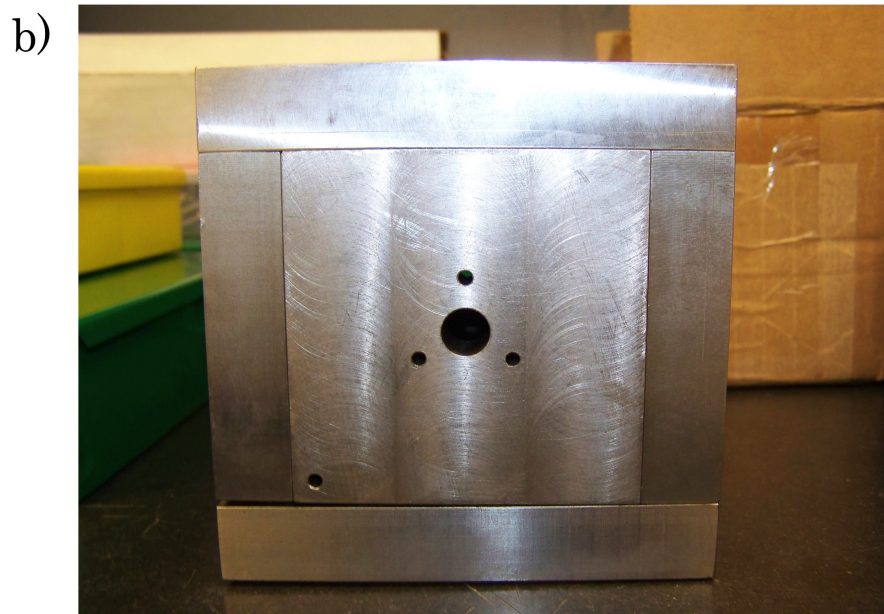
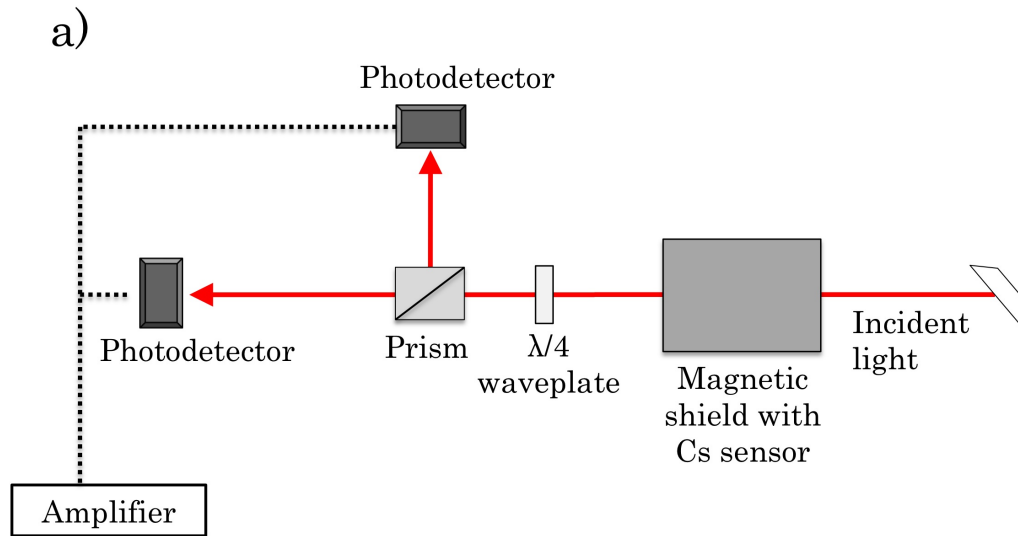


Figure 3.2: a. DAVLL system. A portion of the beam is directed to another Cs cell immersed in a stronger magnetic field. The deviation from the tuned frequency is recorded by an amplifier and sent to the laser head. b. Iron shield for the Cs sensor.

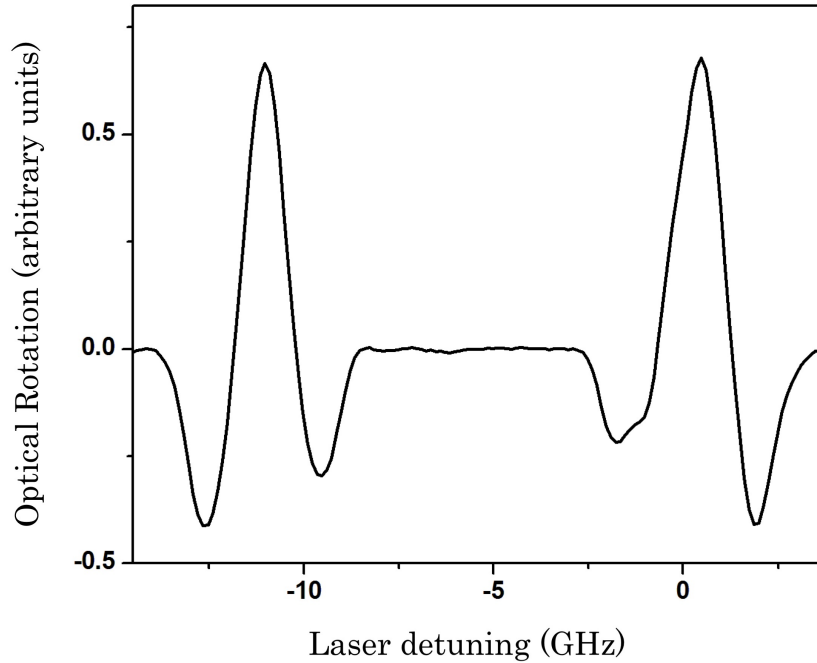


Figure 3.3: Magneto-optical rotation in DAVLL.

polarizer located 45° from the initial polarization prism. The refracted beams hit a photodiode. The output voltage is amplified and read by the lock-in amplifier.

The double-pass arrangement (Figure 3.6) increased the sensitivity of the instrument, since with this configuration, the cells can be located in an optimal position relative to each other and the heating requirement is reduced [40].

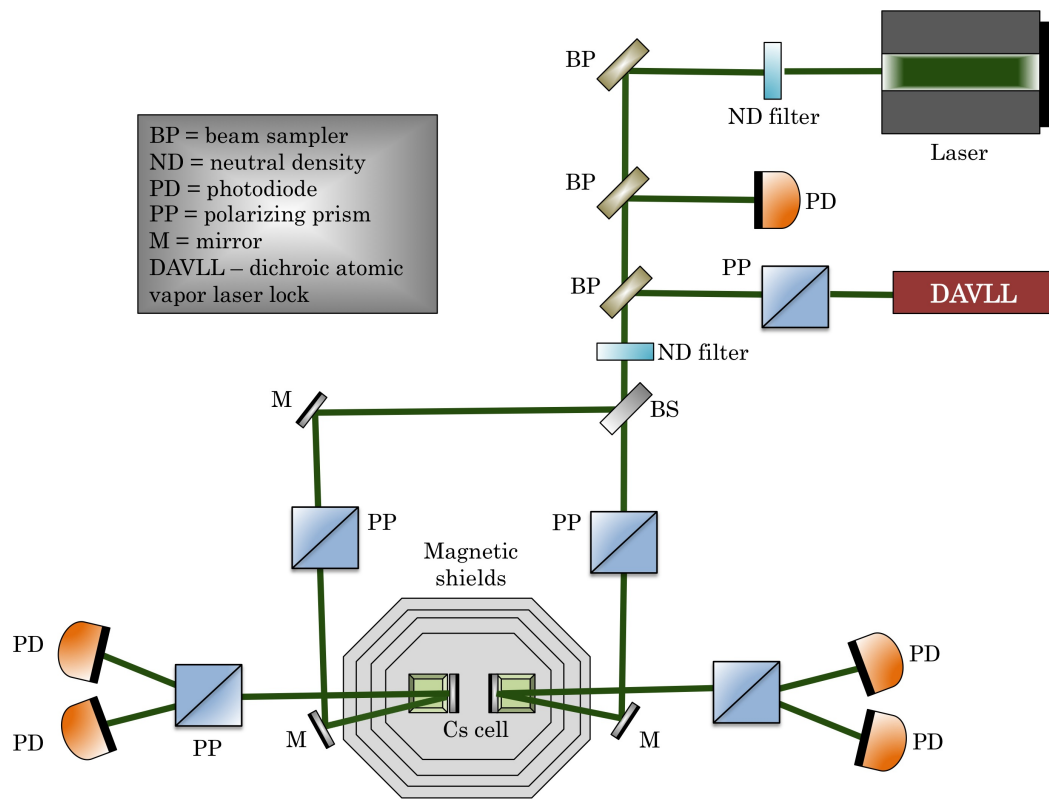


Figure 3.4: Optical layout for Cs magnetometer.

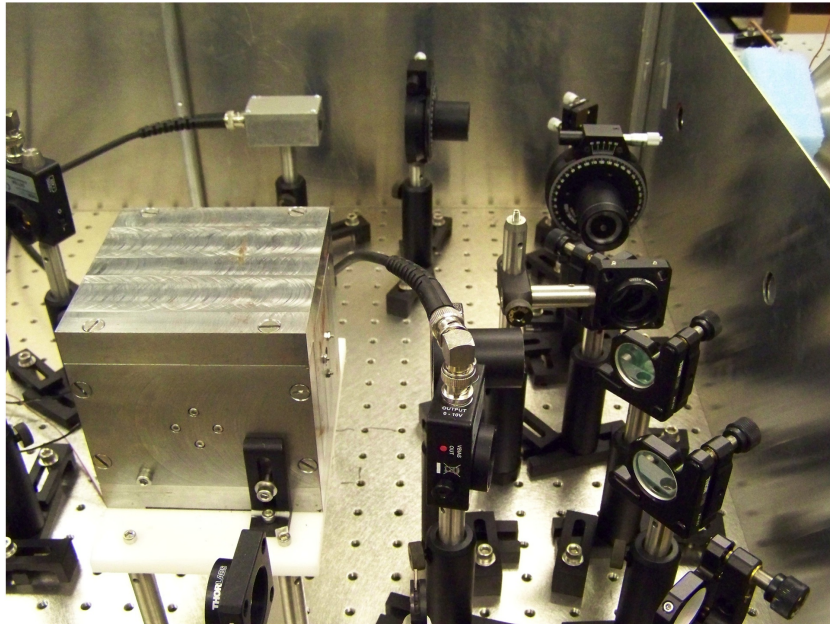


Figure 3.5: Optical elements for the Cs magnetometer.

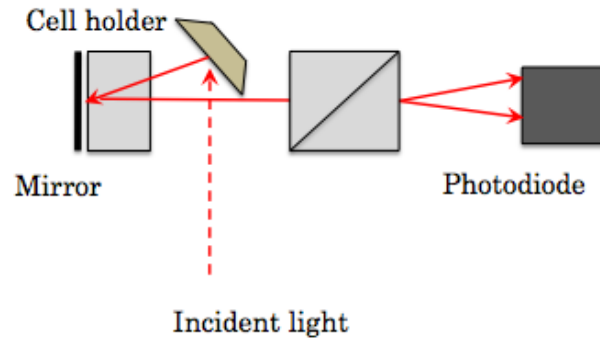


Figure 3.6: Double-pass arrangement of the beam provides optimum positioning of the cells and reduces heating requirement of the cell.

3.1.4 Magnetic shielding

The magnetic shield used in our set-up is shown in Figure 3.7a. The shield was made of high-permeability alloy. Mechanical stress and exposure to magnetic field are avoided to maintain the efficiency of the material. The over-all shape of each layer was a sphere to maximize the shielding factor. Each layer was held up with the next by a styrofoam, which also provided insulation in the set-up. The process of introducing the styrofoam to the shield is shown in Figure 3.7b. The radius of the four cylindrical ports was 11 cm. Magnetic caps were used as enclosures with two ports of the same radius as the ports in the cylindrical layers. The assembly was done for optical access, gradient coils, cell holding, sample inlet, a piercing solenoid and electrical connections. The volume of the shield was only 10% of the volume in [5] and is much smaller to the one used by Ledbetter et al [16].

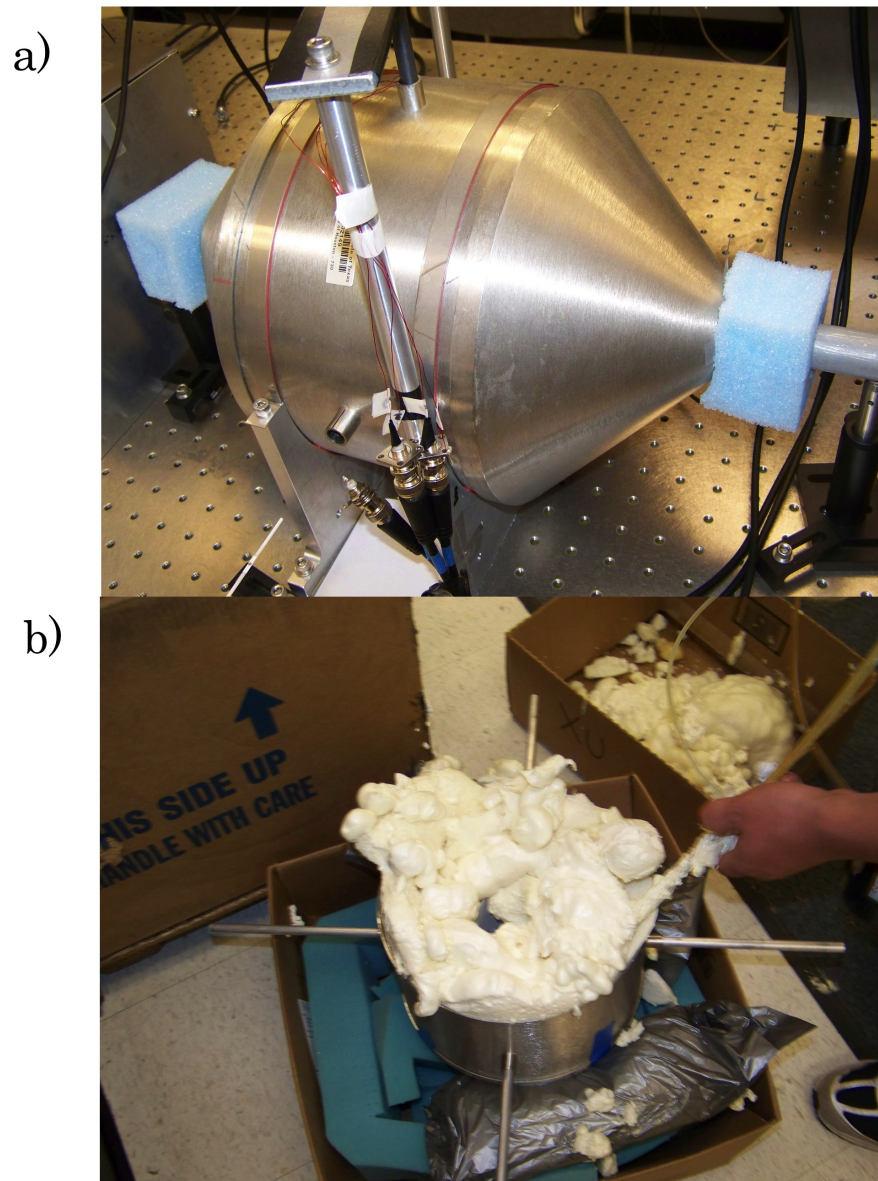


Figure 3.7: a. Magnetic shields. The ports are used for optical access, sample inlet, piercing solenoid and electrical connections. b. Styrofoam introduced in the shields to provide insulation.

3.1.5 Paraffin-coated Cs cells

Atomic magnetometers usually have the resonant medium (a vapor of alkali atoms) contained in glass cells. For our set-up, we use a $5 \times 5 \times 5$ mm³ cell that contains Cs atoms (Figure 3.8a). The inner walls of the cell is paraffin-coated so to minimize relaxation of ground-state polarization due to collisions with the wall. We do not use buffer gas, since we are avoiding higher temperature conditions and the paraffin coating melts at 60 °C.

The cell holder was designed in such a way that the two sensors are located at a minimum distance from each other. In the middle portion was a gap to give space for the sample holder (Figure 3.8b). The holder was made of Delrin material to prevent the introduction of extra magnetic field caused by metallic materials. Gold mirrors were glued on the back of the cell for beam reflection. Gold was chosen because of its high reflectivity. Plastic screws were present in order to adjust the angle of the mirror. The entire cell holder was held up by a plastic rod that goes through the upper part of the magnetic shield.

The density of atoms was increased by raising the operating temperature. Heat was supplied using a twisted Teflon-coated stainless steel wire wound around the outside part of the innermost layer of the magnetic shield. This heating method was found to be efficient and did not introduce extra noise at a significant level, since the configuration of the wire was canceled and shielded. A dc power supply was used to generate consistent heating.

The reduced cell size enhanced the filling factor, or the distance between the

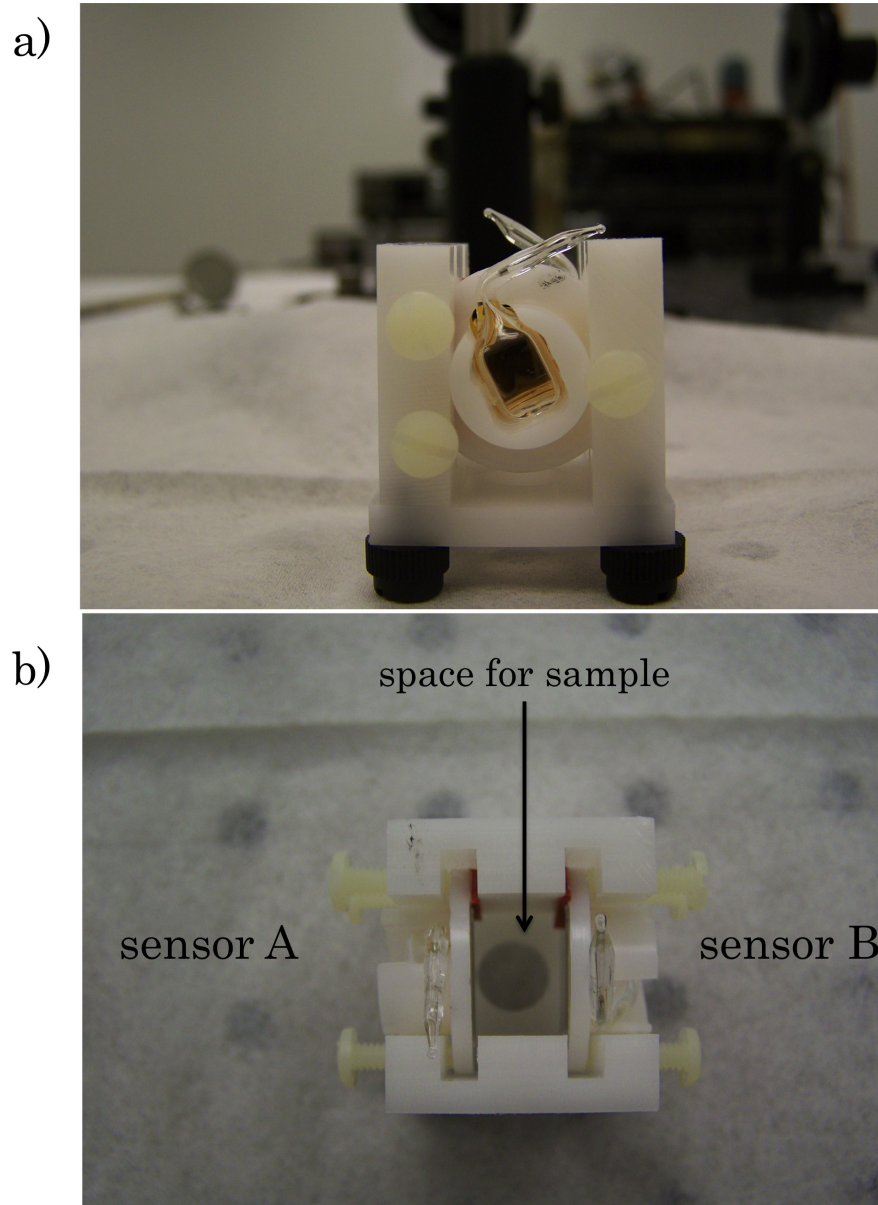


Figure 3.8: a. Cs sensor on the cell holder. b. Cell holder has a gap in the middle to provide space for the sample holder. Picture view is upside-down.

sensor and the sample of interest. The heating power needed for the containment of equal count was also reduced.

We chose cesium cells over other alkali atoms because of its distinctly resolved absorption bands, which reduced the possibility of laser frequency cross-over. Also, Cs-based magnetometers seemed to be the preferred type for common optical magnetometers due to its high accuracy and low heating demands.

3.1.6 Internal coils and the piercing solenoid

The internal coils were wound around a Teflon tube with an inner diameter size enough to accommodate the cell holder. The internal coils included a Maxwell coil, a Helmholtz coil, and gradient coils (Figure 3.9a and 3.9b). These coils were used to cancel the residual magnetic field and gradients and to provide a bias field. The bias field followed a Faraday geometry for optical rotation, in which it is directed along the center-to-center line of the cells, defined as the z axis. Since the sample magnetic field was much smaller than the bias field, the gradiometer was only sensitive to the magnetic field change along the z -axis. A dc source (Krohn-Hite, Model 523) supplied current to the z -gradient coil, which balanced the resonance frequencies of the magnetometers such that the difference between them was less than 0.5 Hz. The rest of the coils were driven by dry batteries.

The piercing solenoid was wound around a long, hollow aluminum tube. It was placed horizontally in the central portion of the magnetic shield (Figure 3.9c). This

provided the leading field, which directed the spins after the encoding region (discussed further in Chapter 4). The space inside limited the detection volume.

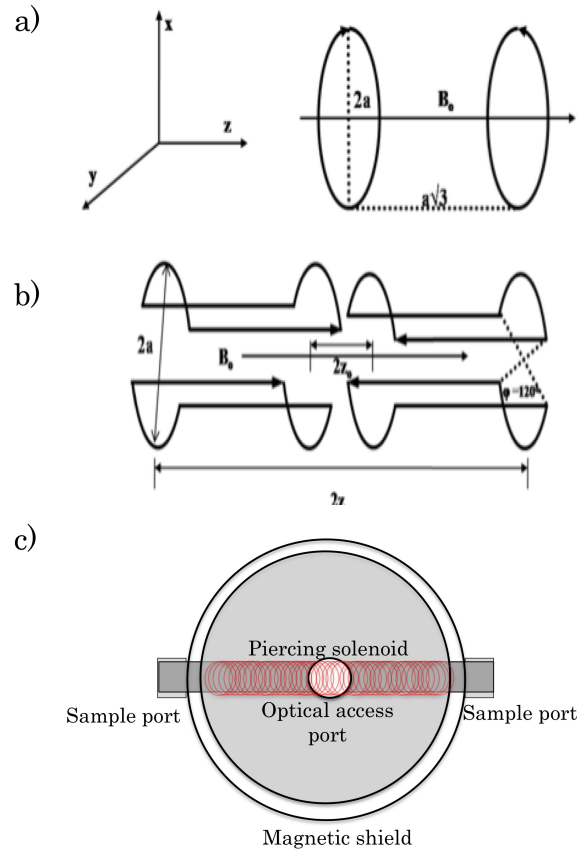


Figure 3.9: Internal coils comprise of a. Maxwell coil, b. Golay coil and; c) solenoid.

3.1.7 Polarimeter

The rotation angle was measured with a balanced polarimeter in which the fast axis of the detecting polarizing prism is at an angle of 45° to the initial polarizing prism (Figure 3.4). Denoting the photocurrents from the two photodiodes of the

polarimeter as I_1 and I_2 , the optical rotation angle ϕ , $\phi \lll 1$, would follow

$$\phi = \frac{I_1 - I_2}{2(I_1 + I_2)}. \quad (3.1)$$

3.1.8 Electronics and communications system

The over-all electronic connectivity is shown in Figure 3.10. Fast modulation of light is necessary to overcome low-frequency noise. In such case, lock-in detection is used. For NMOR with frequency-modulated light, detection of plane rotation must be synchronized. Therefore, a lock-in detector is an important element of the setup. We used SR830 lock-in amplifiers from Stanford Research. The differential current signals were measured with a time constant of 30 ms. In addition to detection of rotation, lock-in amplifiers were also used as voltage source for the piercing solenoid (lock-in amplifier II) and a dc source for the voltage scan needed to obtain the absorption spectra of Cs (lock-in amplifier I). Communication with TECMAG was also done via lock-in amplifier I.

A laser amplifier was used to detect a sample beam for power monitoring. A resistor load (Figure 3.11a) was needed to provide signal to the laser controller.

The function generator provided the modulation frequency to the laser controller. Another lock-in amplifier used for the DAVLL system gave the DC signal to lock the laser at a specific wavelength. Using an ac-dc mixer (Figure 3.11b), both information were fed into the laser controller. The function generator also communicated with both of the lock-in detectors to synchronize the detection of light.

A personal computer was used to store the in-phase and quadrature components

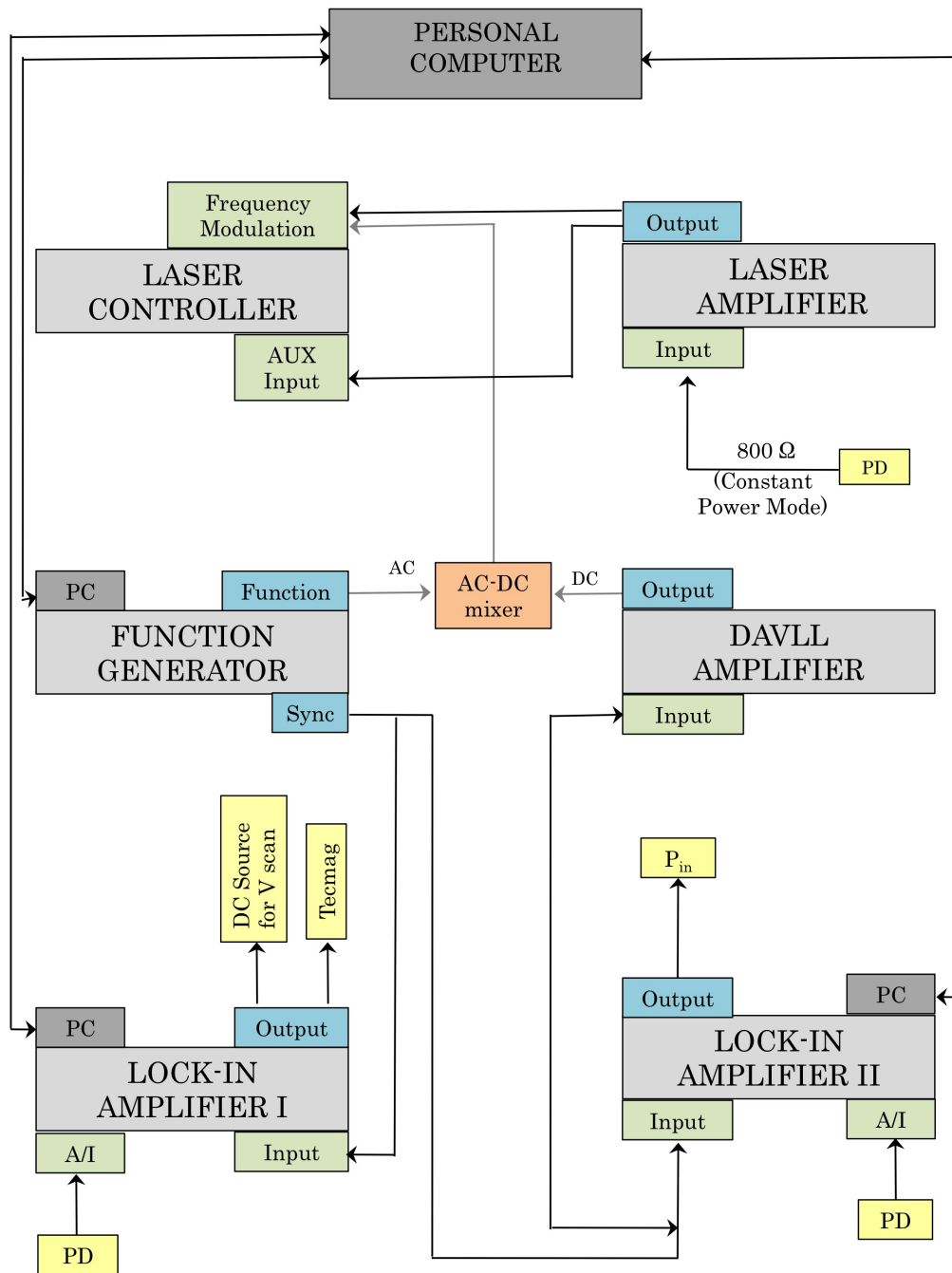


Figure 3.10: Electronics and communications system.

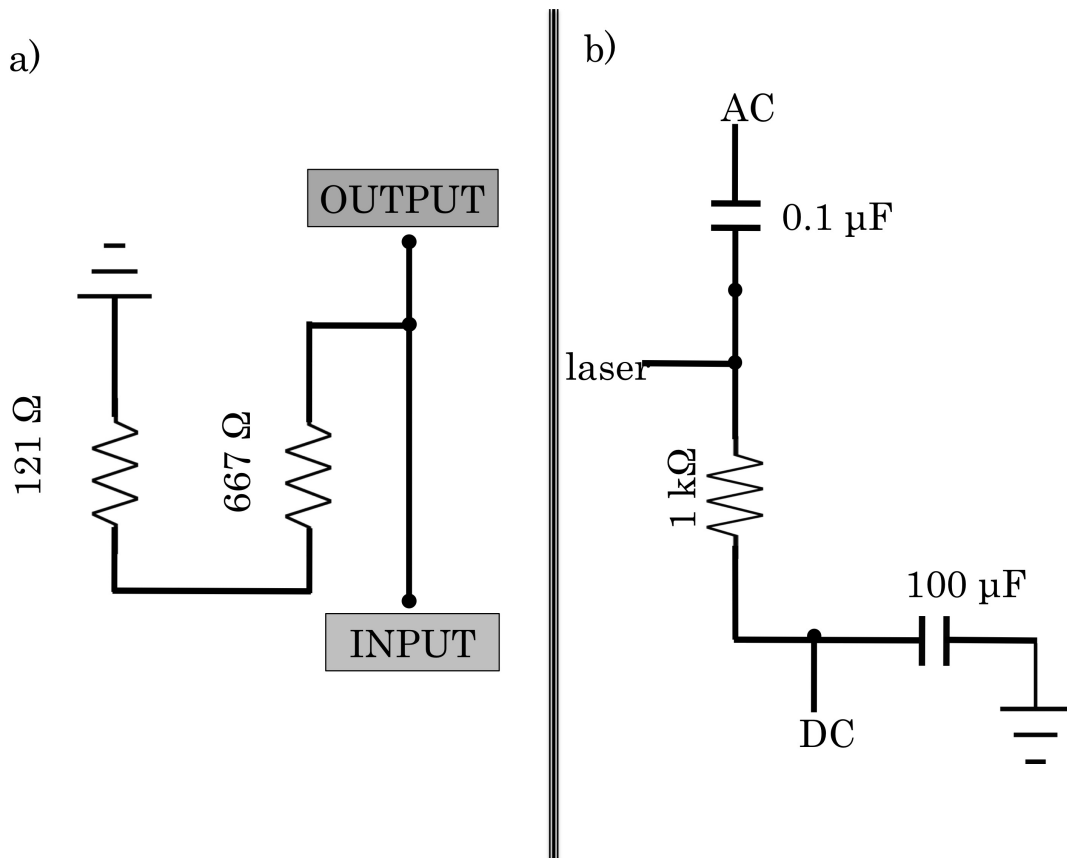


Figure 3.11: a. Circuit diagram for resistor load for power monitoring. b. Circuit diagram for ac-dc mixer.

of the NMOR signals as detected by the lock-in amplifiers, which were connected to the computer via a GPIB interface. Using a LABVIEW program (Figure 3.12), these signals could be visualized. The phases of both quadrature signals could be adjusted via the auto-phase button. The main goal was to set the phase of the in-phase signal to be less than 5° , while the out-phase was less than 180° . The oscillation amplitude

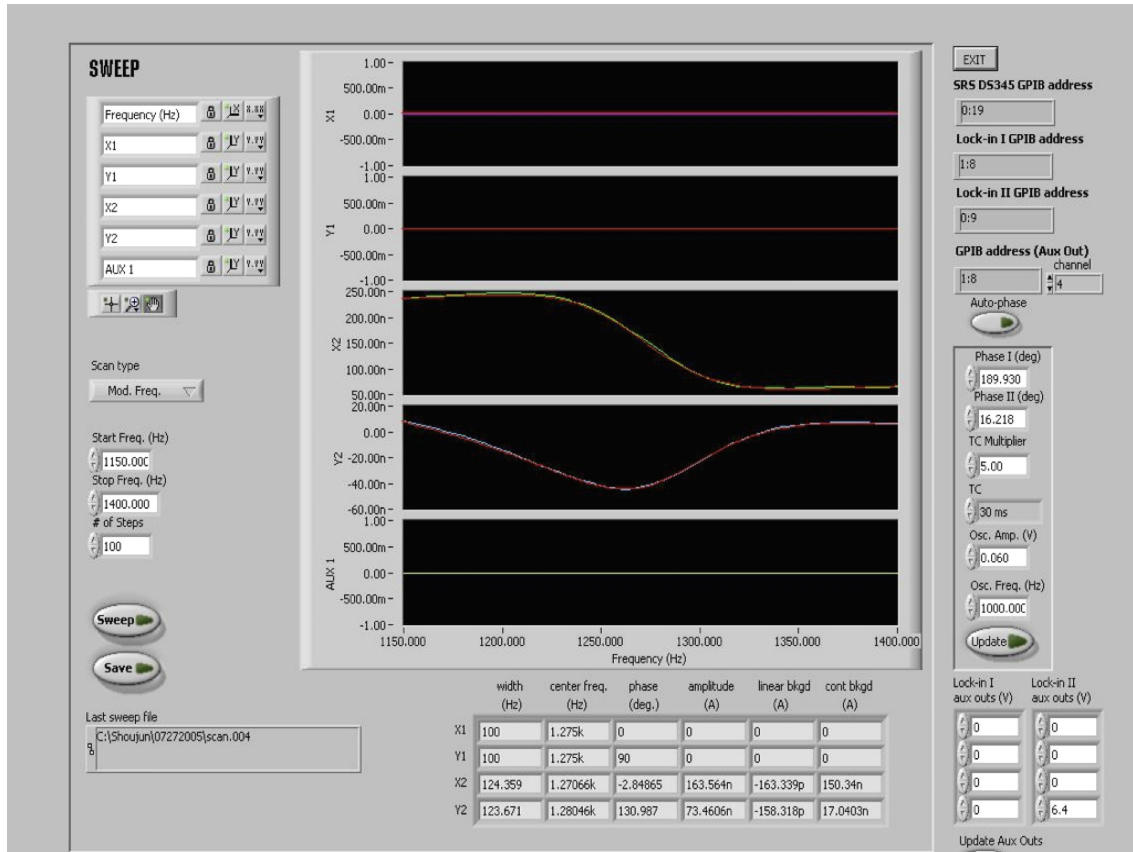


Figure 3.12: LABVIEW interface for GPIB communication and frequency modulation.

of the modulation frequency and the modulation frequency can also be set via the LABVIEW program.

To lock a resonance, the center frequency was determined in the quadrature

signal. This method was slow and required stabilization of the system each time the modulation frequency was changed. This can be overcome by a feedback algorithm that has proportional and integral parameters.

The deviations from resonance were proportional to the in-phase signal from one magnetometer. This signal was measured, inverted and fed back to the function generator and modifies the modulation frequency. The way the computer provided feedback is via an integral loop as given by the equation:

$$f = P\left(\varepsilon + I \int_{-t}^0 \varepsilon dt'\right) \quad (3.2)$$

where f is the feedback signal, ε is the error signal and P and I are the proportional and integral coefficients, respectively.

For calibration, we set P as 50% of the value of the oscillation threshold with a fixed integration range. The value of I was adjusted to optimize the response of the instrument to discrepancies from the square wave.

The magnetometer designated as the primary channel was, therefore, always on resonance. On the other hand, the in-phase signal from the other magnetometer was free of common-mode noise. This algorithm is especially advantageous since it is not sensitive to noise and it enables the user to alter parameters of the integral function.

3.1.9 Characterization of the instrument

In this section, we enumerate the characteristics of Cs magnetometer with our present configuration.

Absorption of Cs

The absorption profile of Cs from one of the sensors shown in Figure 3.13a corresponds to the hyperfine spectrum of the D1 transition of the alkali atom. We chose the D1 profile over D2 because the hyperfine transition strengths in D1 are much higher compared to those in D2 [41]. From experiments, we observed that for a particular voltage range, the one that was tuned to the highest voltage gives the most sensitive and stable signal. This voltage corresponded to the highest wavelength, which translated to the hyperfine transition with the lowest energy requirement (Figure 3.13b).

Quadrature signals

Another feature of our instrument was the resonance profile of Cs around the modulation frequency. We observed resonance when the modulation frequency was twice the Larmor frequency. A bias field was used to detect the resonances. The in-phase and out-phase quadrature signals are shown in Figure 3.14. The widths of these resonances (< 100 Hz) corresponded to twice the ground-state coherence relaxation rate.

Square – wave signal for calibration

To determine the sensitivity of the instrument and to calibrate the optical output from the lock-in amplifier, we used a 100 pT, 0.1 Hz magnetic field. The difference signal between the two sensors is plotted in Figure 3.15, with an integration time of 30 ms per data point.

Based on the noise level of 0.7 pT (peak to peak), we deduced the sensitivity of

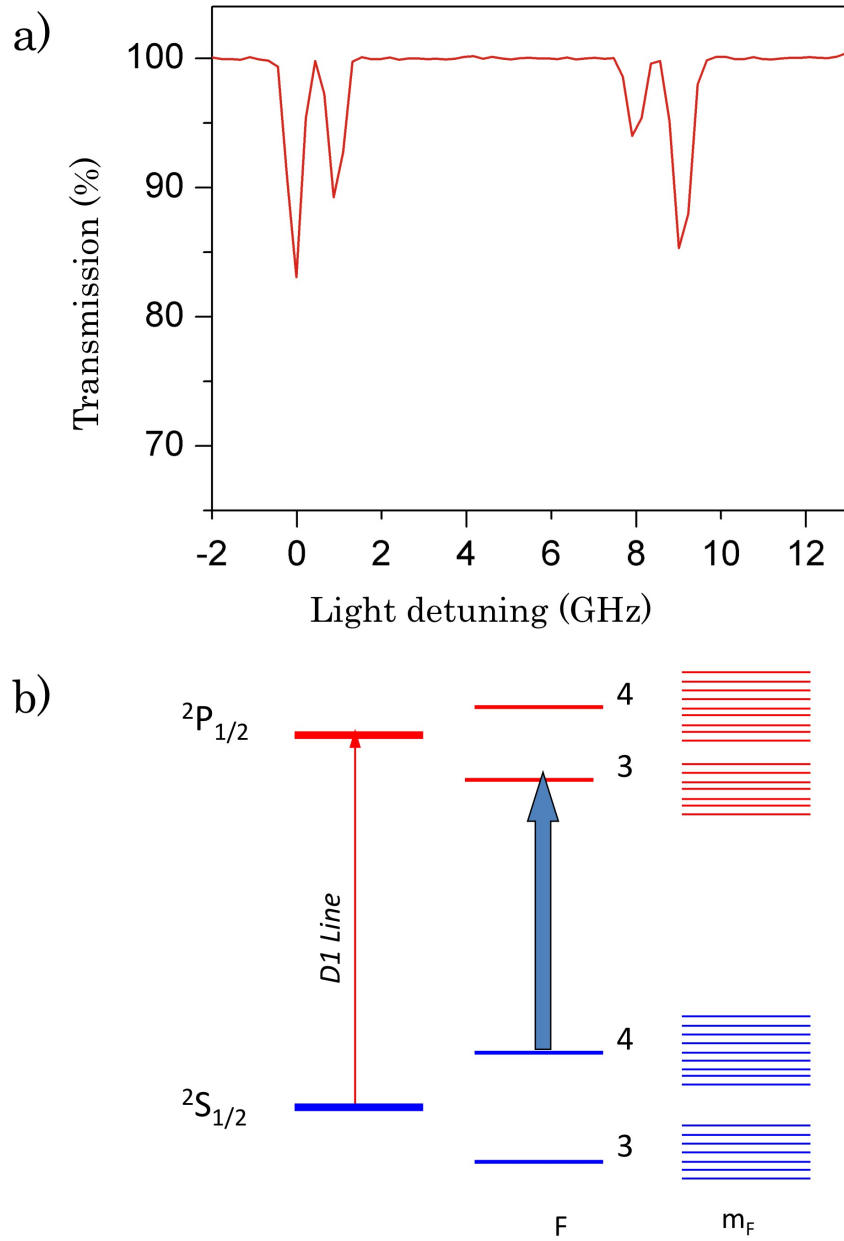


Figure 3.13: a. Absorption of Cs sensor of the D1 transition. b. Highest signal was found to be from the hyperfine transition $F = 4 \rightarrow F' = 3$.

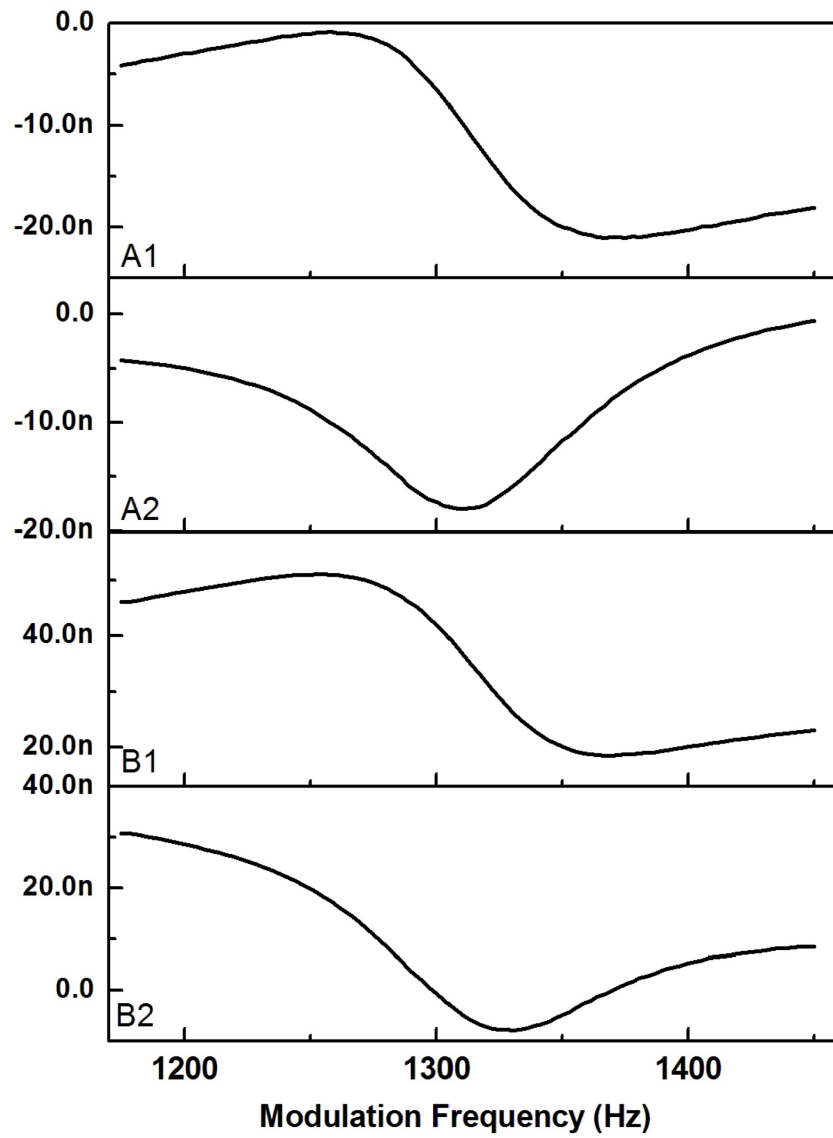


Figure 3.14: In-phase and out-phase resonance signals of Cs magnetometer

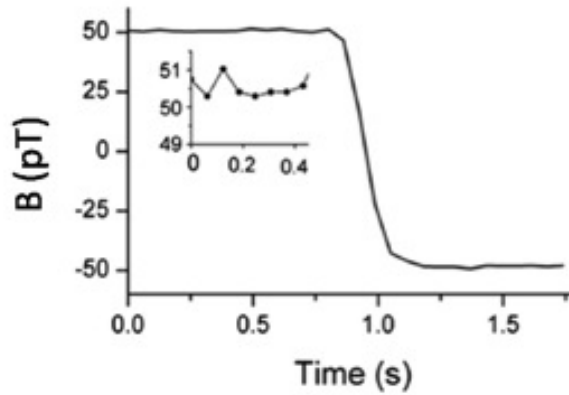


Figure 3.15: Signal for instrument calibration at 100 pT, 0.1 Hz magnetic field. The in-phase signals correspond to A1 and B1, while the out-phase signals correspond to A2 and B2.

the magnetometer to be $150 \text{ fT/Hz}^{1/2}$. Compared to the sensitivity of $80 \text{ fT/Hz}^{1/2}$ with 1-cm atomic sensors in the work of Xu and co-workers [40], the detection limit of the current apparatus was improved by more than four times because of the r^{-3} dependence of the magnetic field.

Calibration was done by simply comparing the ratios between the magnetic field and amplitude of the test signal versus the magnetic field and amplitude of the sample being measured.

Temperature optimization

The temperature dependence of sensitivity was investigated in the range of 34°C to 40°C . An identical optimization procedure was used for three different temperatures of 34°C , 37°C , and 40°C . The signal to-noise ratios (SNRs) for a fixed magnetic signal were plotted as a function of temperature in Figure 3.16.

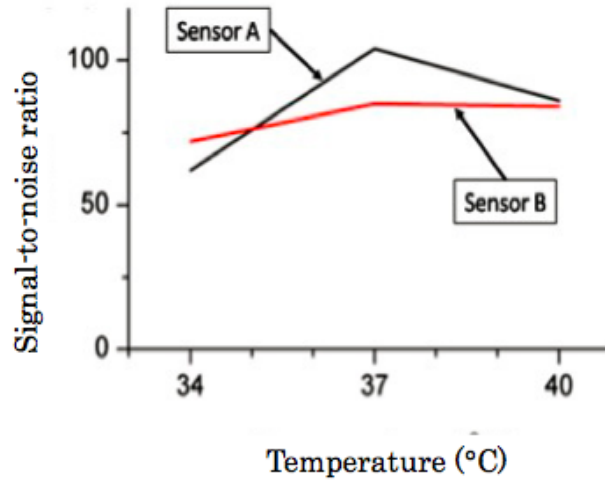


Figure 3.16: Temperature optimization. Highest sensitivity is achieved at 37 °C

Result showed that 37°C was the optimal operating temperature in the temperature range being tested. Interestingly, this temperature value was consistent with a model by Shah et al. [42]. The difference in the behavior of the sensors may be caused by cell-to-cell variations in the manufacturing process.

To reveal the stability of the instrument, we monitored a 100 pT signal in two modes: in one, the laser was stabilized by the DAVLL, and in the other, there was no stabilization. The results are shown in Figure 3.17. An arbitrary offset was implemented to the red trace in order to separate the two traces for comparison. No significant difference was observed in terms of baseline drift and SNR between the two modes, in the time frame of the test. This was different from similar high vacuum rubidium sensors, in which a DAVLL is required to obtain the desired sensitivity [5].

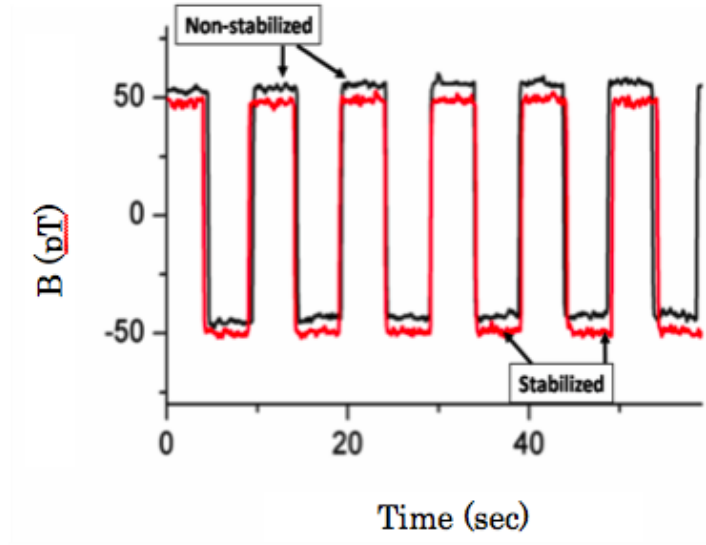


Figure 3.17: Comparison between stabilized and nonstabilized modes.

We speculate that the extraordinary stability of the current apparatus may be attributed to three factors. First, the absorption bands of cesium are distinctly resolved, which reduces the possibility of laser frequency cross over. Second, by operating at a lower temperature, the heating requirement is low, which reduces the associated noise. Third, it is possible that the cesium laser is more stable than the rubidium laser.

This optical magnetometer still has large room for improvement. For example, the atomic sensors are made by glass blowing. A drawback of sensors made in this fashion is the poor optical quality of the glass surface, which distorts and scatters the laser beam. We measured the power of the incident beams, which were 11.8 and 10.7 μW , respectively, and the power of the reflected beams, which were 3.2 and 3.3 μW , respectively, for the two sensors. The absorptions, however, were only

24% and 20%, respectively. This indicates that the signal amplitude is lowered by approximately a factor of 2. The imperfections of the sensors may be eliminated by using micromachining.

3.2 Atomic magnetometer for magnetic particle sensing

A Cs magnetometer with new features was built in order to make our set-up more applicable to our study of interest and to enhance the over-all sensitivity of the instrument. New features included new sets of magnetic shields, a plastic disc that served as a divider and the use of quadrant photodiode for signal reading.

3.2.1 Magnetic shields

The magnetometer consisted of three main components: 1 is a sample inlet system that uses an automated linear transducer to introduce samples at a constant speed, 2 is a magnetic shield that accommodates one or more atomic sensors for measuring the magnetic signal of the magnetic particles, and 3 is an aluminum enclosure that contains the optics and the laser to minimize the optical noise caused by stray light and other optical interferences (Figure 3.18a). The innermost caps of the new set of magnetic shields that we used are shown in Figure 3.18b. The caps on one side has rectangular ends. Unlike the previously built magnetometer, the sensor(s) can be arranged on one side, while the scanning of the sample can occur either through

the central port of the magnetic shields, or the other side of the magnetic caps. This configuration not only lessens noise due to air turbulence but also accommodates a more compact optical layout.

3.2.2 Divider

A key feature in this design is a dividing piece that separates the sample inlet channel, which is routed through two ports on the side of the magnetic shield, and the atomic sensor. The divider is made of a thin plastic and placed in the middle of the four-layer magnetic shield (Figure 3.19a). The divider prevents air circulation caused by the motion of the transducer and maintains the atomic sensors at a stable temperature. Therefore, it reduces the undesired optical rotation caused by air currents and avoids the atomic density fluctuation caused by the temperature instability that would occur otherwise.

3.2.3 Cs cell and internal coils

The atomic sensor used in this work is shown in Figure 3.19b. It is essentially a cubic-shaped glass compartment with a long tail. The cubic portion is 5 mm long on each side and coated with paraffin to elongate the coherence time of the polarized cesium atoms. The tail contains a drop of cesium and is connected to the cubic cell by a narrow channel such that cesium atoms continuously refill the cubic compartment.

Figure 3.20 shows the technical design for the coils. There are five different set of coils inside the shield: Helmholtz coil, Maxwell coil, Golay coil, and two saddle

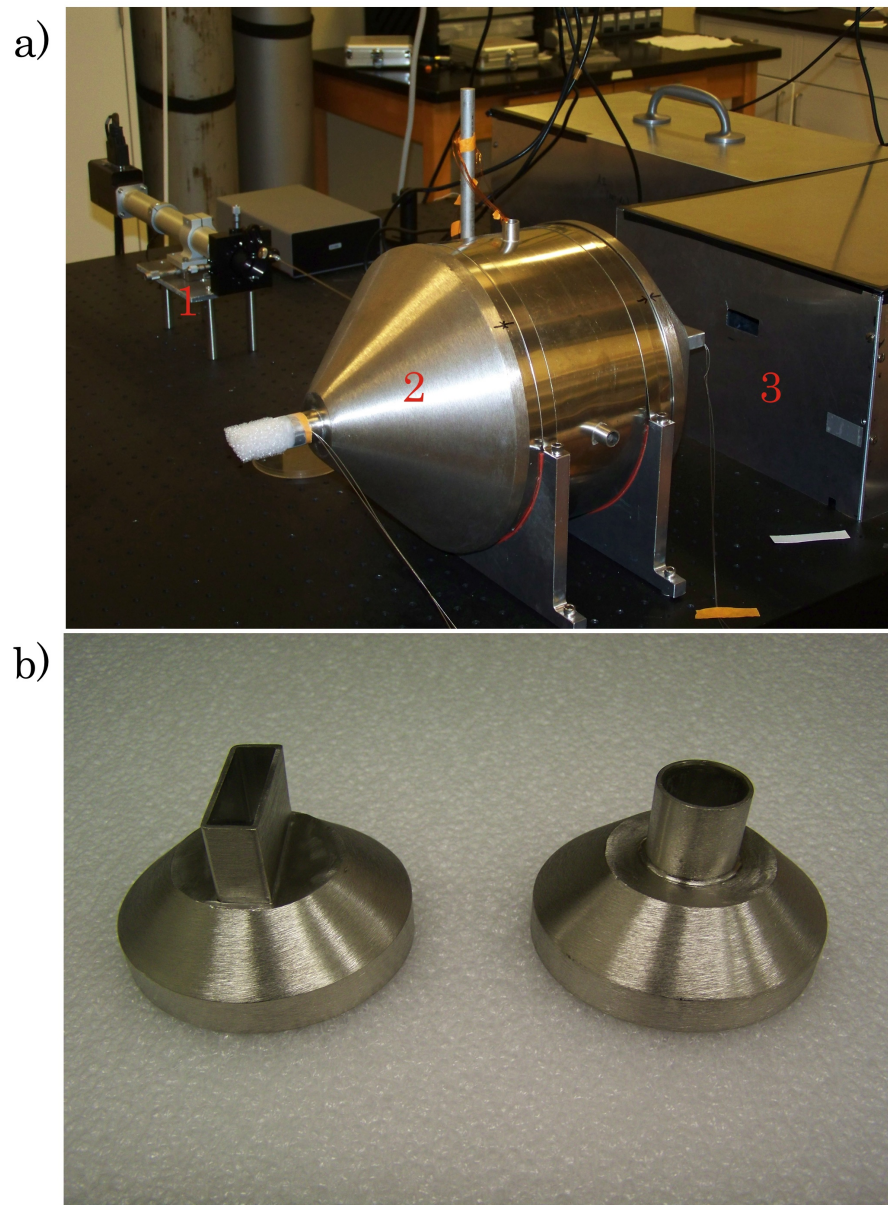


Figure 3.18: a. Three main components of Cs magnetometer: a sample inlet system, magnetic shields and optics enclosed by an aluminum enclosure. b. Internal magnetic caps with different port shapes.

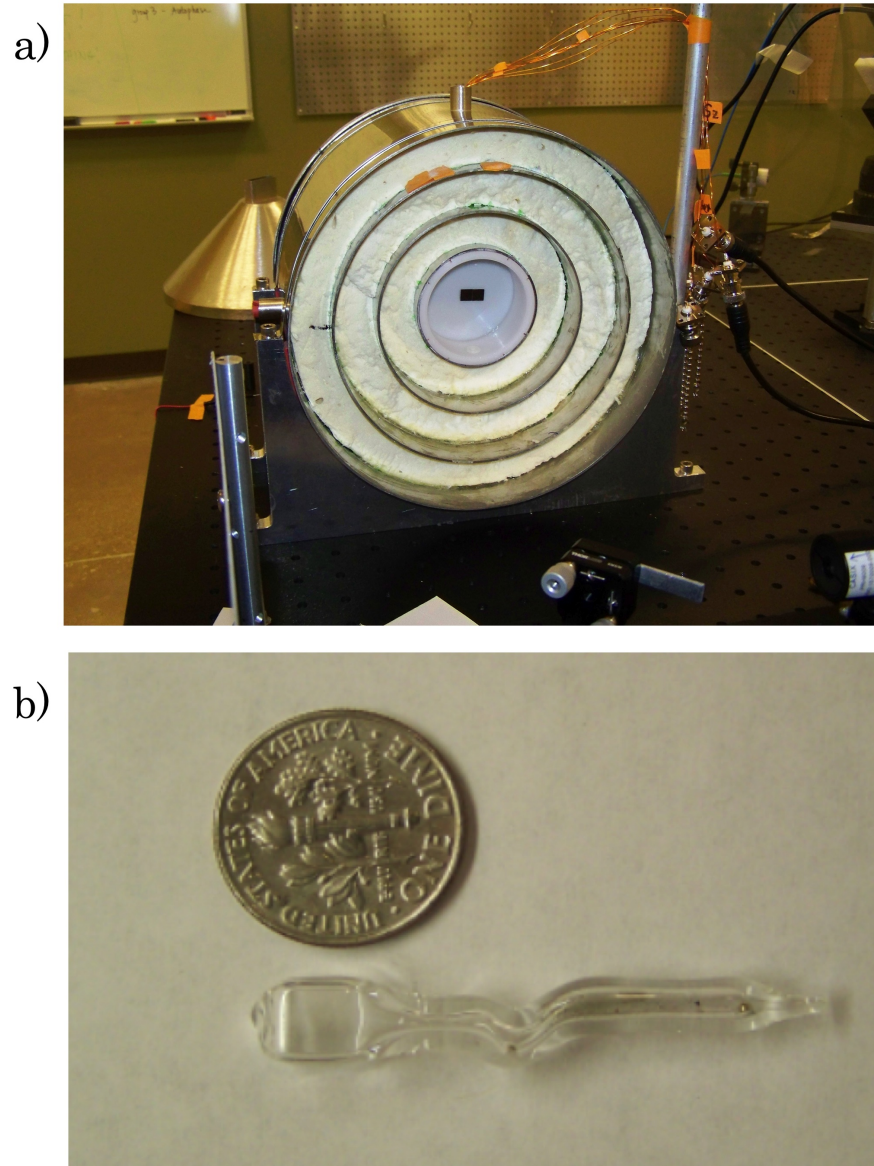


Figure 3.19: a. Cross-section view of the internal part of magnetic shield. A plastic divider separates two regions of the shield. b. Comparison between the Cs sensor and a dime.

coils. Gradient field is provided via the Maxwell coil. The Golay coil was placed inside the magnetic shield for field calibration. The rest of the coils are for noise cancellation. Current for the internal coils are provided via a box with 0.2 ppm/C

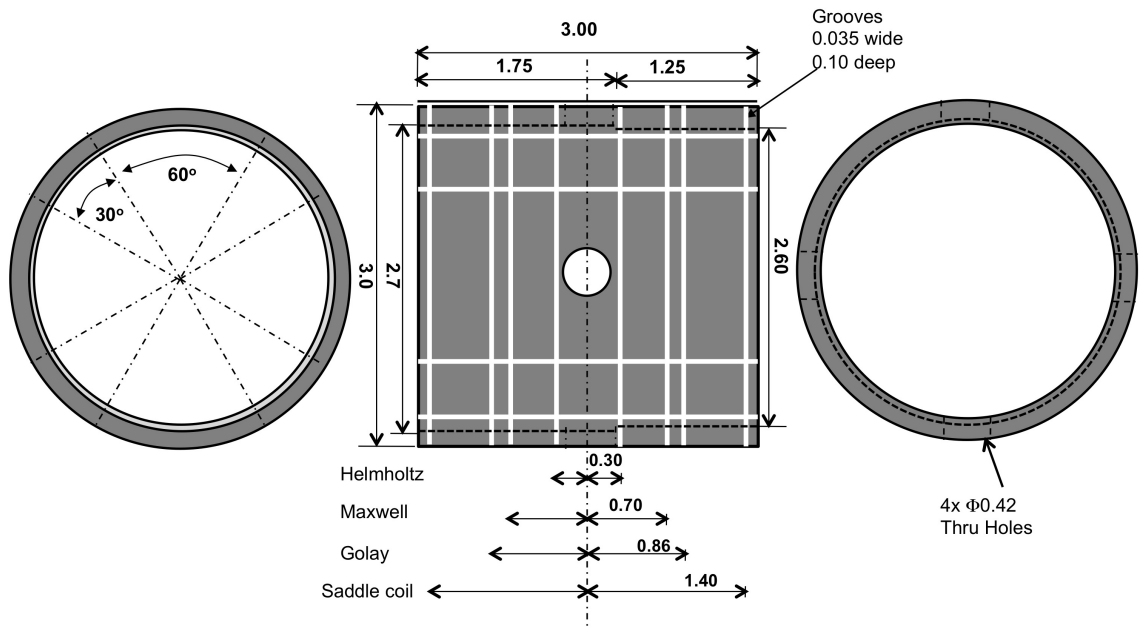


Figure 3.20: Technical design for coil holder located inside the shield.

resistors. Circuit diagram and a picture of the actual box is shown in Figure 3.21.

For the calibration, the sensitivity measurement was conducted in two steps. First, 0.5 V and -0.5 V were applied to the coil to observe the difference in the resonance frequency ω_m . Second, at a constant ω_m , ± 0.1 V was applied to the coil to obtain the signal-to-noise ratio and, subsequently, the sensitivity.

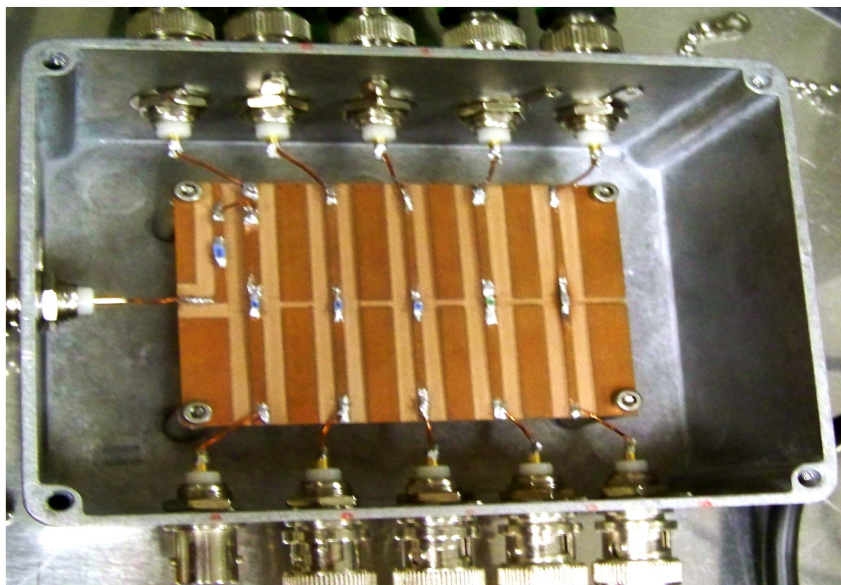
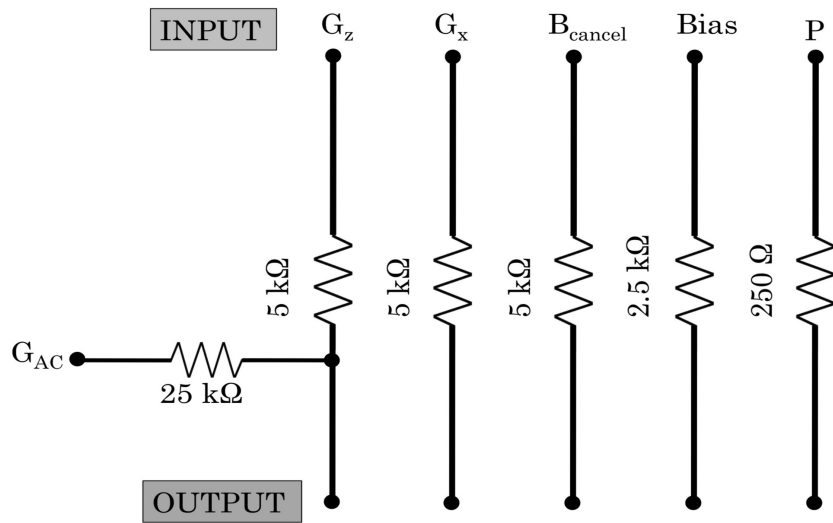


Figure 3.21: Resistor box for the internal coils.

3.2.4 Quadrant photodiode

In our new setup, we use a quadrant photodiode for detection. Quadrant photodiodes are position sensitive light detectors. They simply consist of four separate photodiodes, each quadrant shaped, which together make up a circle (see Figure 3.22). Like all photodiodes, they can be used in a photovoltaic or a photoconductive mode. The photovoltaic mode is widely used because though it has slower frequency response, it is still fast enough for many applications. This mode is also electronically simple and no dark current is present, which means less noise and better sensitivity to low light levels. The four photodiodes share a common cathode (which in photovoltaic mode is connected to ground) and have separate anodes.

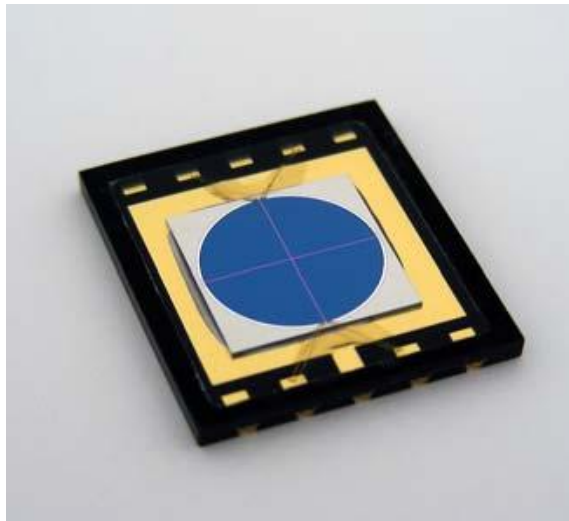


Figure 3.22: Quadrant photodiode for signal detection.

3.2.5 Characterization of the instrument

Sensitivity

The magneto-optical profiles are shown in Figure 3.23 for 0.5 V and -0.5 V, respectively. Fitting with dispersive Lorentz function gives resonance frequencies of 1242.77 and 1239.50 Hz. Therefore, 1 V corresponds to a magnetic field of 467 pT for the specific calibration coil used in this apparatus.

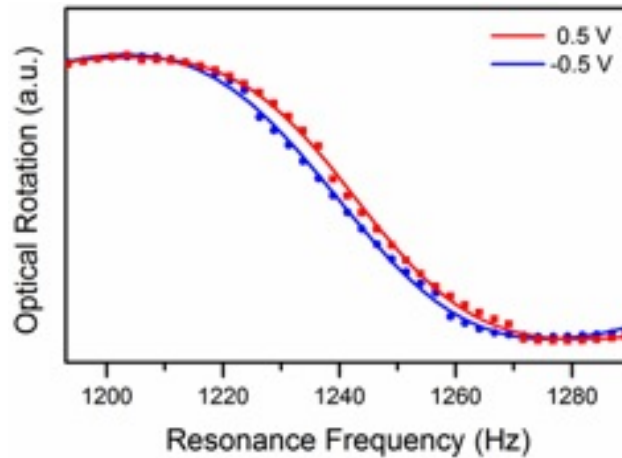


Figure 3.23: Magneto-optical resonances for calibrating magnetic fields.

Calibration

The magnetic fields produced by -0.1 V and 0.1 V were measured (Figure 3.24). The jump in the signal represented the change in voltage from -0.1 V to 0.1 V, which was 94 pT based on the calibration in Figure 3.25. The detection bandwidth is 50 Hz. From the signal-to-noise ratio of ~ 170 , we deduced the sensitivity to be ~ 80 fT/Hz^{1/2}. This is an improvement compared with the ~ 150 fT/Hz^{1/2} sensitivity of a previous atomic magnetometer using the same atomic sensor.

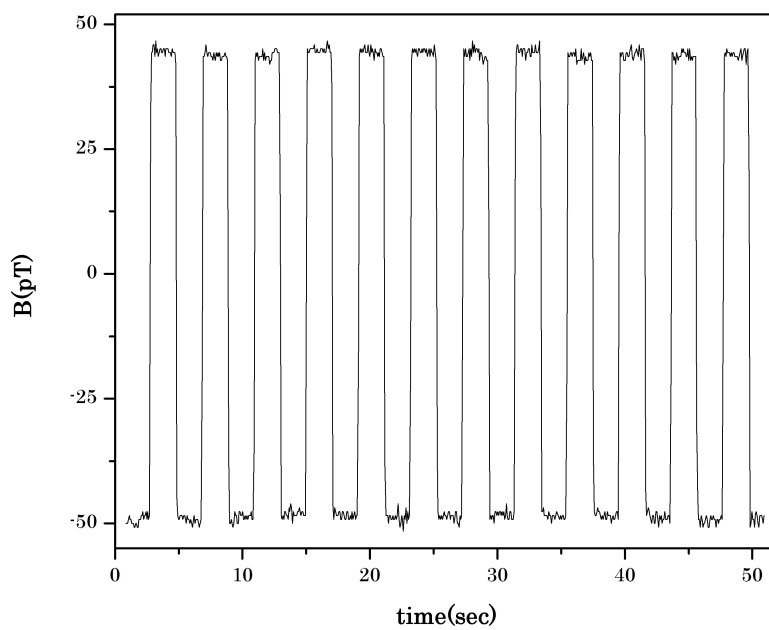


Figure 3.24: Square signal from -0.1 V to 0.1 V.

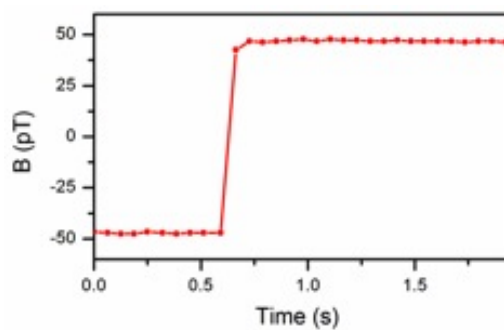


Figure 3.25: Square signal produced from test calibration.

The improvement in sensitivity is likely due to the implementation of the divider that increased thermal stability. Our previous study demonstrated that temperature played an important role in the sensitivity of atomic magnetometers [43]. Compared with the microfabricated atomic sensors that use rubidium atoms, our current apparatus has slightly worse sensitivity. For example, a recent report demonstrated a sensitivity of ~ 50 fT/Hz^{1/2} [44]. However, our apparatus uses Cs atoms in the sensor. One significant advantage is that the operating temperature is much lower, 35-37°C as opposed to 180°C, because cesium has the highest vapor pressure of all the alkali elements and our magnetometer is operated at low vapor pressure condition. The much lower operating temperature facilitates the application of atomic magnetometers to molecular and cellular imaging.

Chapter 4

Applications of atomic magnetometry in magnetic resonance imaging

In this chapter, we present the application of our compact Cs magnetometer in magnetic resonance imaging (MRI). This is especially important for enhanced contrast MRI, one of the most used techniques for diagnosing diseases. The first section in this chapter expresses the motivation of the study, as well as the comparison of existing nuclear magnetic resonance (NMR) techniques. This is followed by a discussion of detection schemes in atomic magnetometry for NMR/MRI, which includes the remote detection technique, the configuration we used for detecting the magnetic resonance signal of water. The third section presents some fundamental principles of contrast MRI. The fourth section shows the experimental results and analysis of

data obtained. The last section is the discussion of challenges of our current set-up and possible solutions.

4.1 Motivation of the study

Conventional MR detection techniques have been widely used in the medical field and fundamental sciences. Three major components of traditional MR devices are a superconducting magnet, cryogenics and a complex electronic system. Because of its bulky size and expensive cost, the applicability of this modality is limited. For example, the clinical MRI instrument cannot be used in remote areas and for imaging in the presence of metallic objects [45]. Alternatively, measurements can be done at the low-field regime, which will eliminate the need for a large magnet for detection. A low-field version of NMR/MRI will therefore make the system more portable, more accessible and more affordable.

One major challenge in developing low-field NMR and MRI is the establishment of a detection technique that has sufficient sensitivity for the intrinsically faint signals that occur after the elimination of the superconducting magnet and the cryogenics. The sensitivity of conventional inductive detection is proportional to the strength of the magnetic field. For this reason, high-field inductive coils, which usually have a small number of turns, are not preferable in the low field regime. It would therefore be beneficial to improve the existing techniques and, more importantly, to develop novel techniques for low-field NMR and MRI.

Several techniques have been developed, including a much improved version of

conventional inductive detection. Using a well-tuned coil containing thousands of turns, Appelt and co-workers [46] presented NMR spectra in the Earth's magnetic field ($\sim 50 \mu\text{T}$) with excellent spectral resolution. A linewidth of ~ 0.03 Hz was achieved in the proton spectrum of benzene. They were thus able to distinguish chemicals based on their characteristic J-couplings. (Note that chemical shift information is not resolvable in such a low field.) One drawback is that a rather large amount of sample, a volume of about a few milliliters, was needed to obtain the spectra. Stepišnik's group [47] and Callaghan's group [48] both demonstrated magnetic resonance images in the Earth's magnetic field using inductive detection, with spatial resolutions of 2.3 and 5.0 mm, respectively.

Alternative techniques have also been explored, including detection with superconducting quantum interference devices (SQUIDs) [49] as mentioned in Chapter 1. The SQUID magnetometer has been applied to diverse applications such as parallel MRI [50], T_1 MRI contrast [2], and magnetoencephalography [51]. When a SQUID is used for NMR/MRI detection, the magnetic flux is generated by the sample nuclear polarization. The high sensitivity of SQUID magnetometers, ~ 1 fT/Hz^{1/2} for SQUIDs operated at liquid helium temperature (4 K), is independent of the strength of magnetic field, making them well-suited for low-field NMR and MRI [52, 53]. However, they require cryogenics to maintain the detecting loop in the superconductive state. This makes SQUIDs inconvenient in certain conditions, such as applications in remote areas or places where cryogenics are not available.

A detection technique based on anisotropic magnetoresistive (AMR) sensors have

also been demonstrated for low-field NMR detection [54]. Compared to SQUID magnetometers, the AMR sensors that were employed possessed a much poorer sensitivity, on the order of $100 \text{ pT/Hz}^{1/2}$, at frequencies above 1 kHz. However, the fact that the sensors are entirely solid-state makes them exceptionally attractive for a miniaturized device. If cryogenic cooling is allowed, AMR sensors have achieved a sensitivity of $32 \text{ fT/Hz}^{1/2}$ [8].

Here, we present atomic magnetometry as another approach for low-field magnetic resonance detection. The magnetic field due to sample nuclear polarization is directly measured, with a theoretically projected sensitivity on the order of $0.01 \text{ fT/Hz}^{1/2}$ under optimal conditions [14]. In addition to direct measurement, cryogenics and a superconducting magnet are not necessary for an atomic magnetometer to operate. Therefore, with high sensitivity and portable features, the use of atomic magnetometer for low-field magnetic resonance detection can overcome the presently faced issues with conventional NMR and MRI methods.

For clinical MRI, the use of contrast agents is prevalent to obtain enhanced images. Gadolinium chelates are widely introduced to the patient's body. The efficiency of contrast agents is normally based on proton relaxivity, which is known to be dependent on the strength of external magnetic field. It has been found that at extremely low fields, the performance of contrast agents is significantly high, as seen from the nuclear magnetic resonance dispersion profiles in Figure 4.1 [55]. Thus, utilization of these contrast agents at low field will not only maximize the efficiency of these contrast agents, but will also make diagnosis safer, since at low field, the concentration requirement for the contrast agent may be substantially decreased,

which will decrease the risk of nephrogenic systemic fibrosis disease [56].

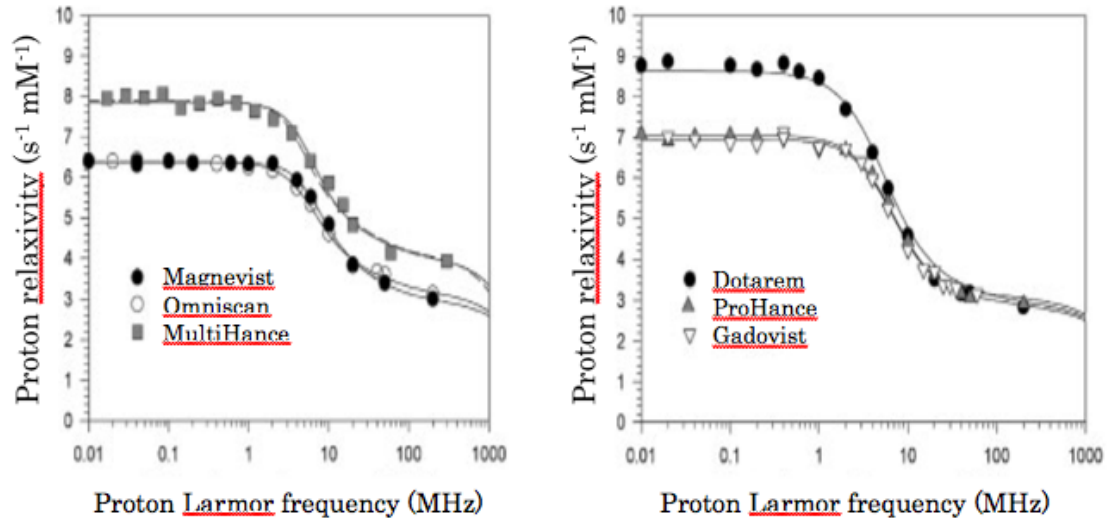


Figure 4.1: Nuclear magnetic resonance dispersion profiles of clinical contrast agents. Relaxivity is significantly high at lower magnetic fields.

A new group of contrast agents has been recently proposed. They are called smart contrast agents due to their specific response to certain changes in physical parameters such as pH, metal ion concentration, enzyme activity, temperature, and partial pressure of oxygen [57]. These parameters are important indicators of diseases such as tumor, neurodegenerative diseases, stroke, ischemic diseases, and others. With the use of these contrast agents, these parameters can be monitored noninvasively. In this study, we focus on the pH effects on the behavior of gadolinium-based contrast agents at low-field, which will be very beneficial to indicate the presence of tumor cells.

With the aforementioned advantages of low-field detection, atomic magnetometer

is therefore a promising MR detection technique. In the next section, the ways an atomic magnetometer detect magnetic resonance signal are discussed.

4.2 Detection schemes

Two primary schemes have been explored in detecting MR signal with an atomic magnetometer namely, the remote detection scheme and the radiofrequency detection scheme. Both schemes are applicable for low-field NMR and MRI. In remote detection, the fields are physically separated to allow independent optimization for each stage. When the sample is diluted in the encoding region, remote detection offers a better SNR because a much improved filling factor can be achieved in the detection stage. Furthermore, information regarding the flow behavior can be revealed via time-of-flight imaging [58]. In RF detection, a static sample can be studied, similar to conventional NMR. The nuclear resonance frequency is directly measured, which is more efficient than the point-by-point method in remote detection.

4.2.1 Remote detection scheme

Remote detection simply means that the signal detection region is spatially separated from others. The remote detection scheme was first developed by Pines and co-workers [59]. A schematic is shown in Figure 4.2. In this scheme, the sample flows through three stages namely, pre-polarization, encoding, and detection. In the pre-polarization stage, the nuclear spins are magnetized using a strong permanent

magnet, since a homogenous field is not necessary. The next stage is the encoding of nuclear spins, in which a low but homogeneous magnetic field is applied to record spectroscopic or spatial information. Encoding is done using appropriate pulse sequences (and weak gradient magnetic fields in the case of MRI). One convenient option is the use of the Earth's magnetic field as the encoding field, which is extremely homogeneous in the absence of local disturbances. After encoding, the precessing nuclear polarization, which now contains spectral or spatial information, experiences a $\pi/2$ pulse which tips it back as the longitudinal polarization. The magnitude of the longitudinal polarization is detected at the detection stage by an alkali sensor. For

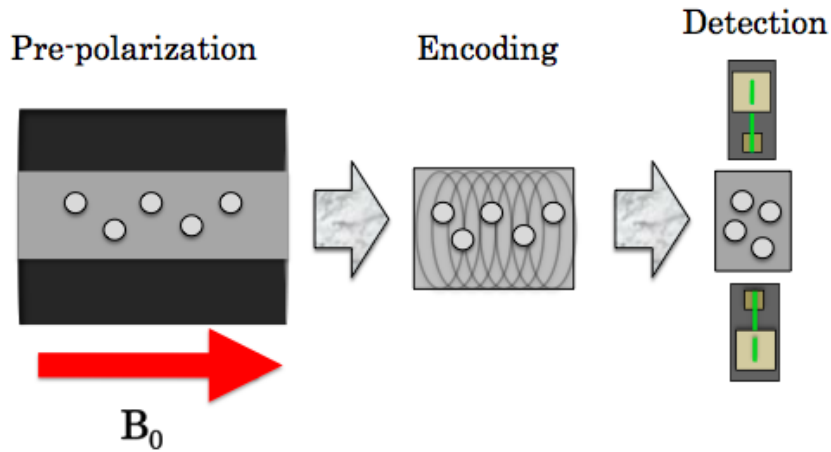


Figure 4.2: Remote detection scheme for nuclear magnetic resonance detection. Three regions are pre-polarization, encoding and detection.

remote detection of MRI, a pure phase encoding pulse sequence is most often used (Figure 4.3). In phase encoding, the nuclear spins are allowed to precess for a fixed amount of time in the presence of a gradient magnetic field. Therefore, the spatial information of the nuclear spins is encoded as different phases of precession that are

contained in the overall polarization. The overall polarization is directly measured by atomic magnetometers. No excitation pulses are needed at the detection stage for atomic magnetometers, because the magnetometer detects static magnetization instead of requiring an oscillating signal, unlike inductive coils. By measuring a set of overall polarizations as a function of systematically varied gradients, the spatial information is obtained by Fourier transformation of the polarizations.

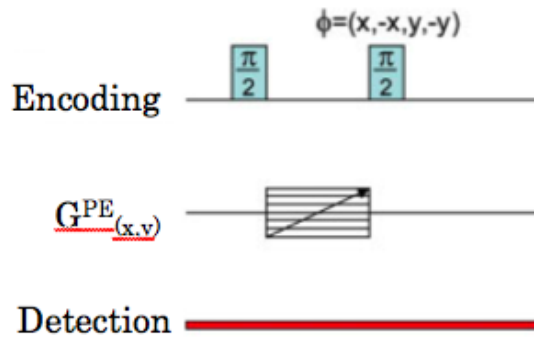


Figure 4.3: Pulse sequence of two-dimensional phase encoding. Four-step phase cycling is employed on the second $\pi/2$ pulse to overcome drifting noise.

4.2.2 Radiofrequency detection scheme

A different scheme for NMR, but not demonstrated for MRI yet, was presented by Savukov and co-workers [4]. This detection scheme is termed RF detection by the authors and is shown in Figure 4.4. In this scheme, the sample is static, similar to conventional NMR. A pulsed magnetic field is used for pre-polarization. (For fluidic sample, the sample may also be polarized by a permanent magnet outside the

magnetometer and flow into the detection region.) The nuclei are located inside a closely-wrapped long solenoid, so that this field is not experienced by the outside atomic magnetometer. By tuning the bias field B_a , the precession of the atoms matches the precession of the nuclei, allowing direct detection of the nuclear precession (free induction decay). An NMR spectrum has been exhibited with this technique. Twenty-eight milliliters of water pre-polarized by an electromagnet ($14 \mu\text{T}$) was encoded in a field of $\sim 1.5 \mu\text{T}$ at the same physical location. According to the sample volume and SNR of the spectrum (~ 10), the detection limit is $40 \mu\text{l}$ of water pre-polarized by a 1-T magnetic field. To date, MRI with atomic magnetometers

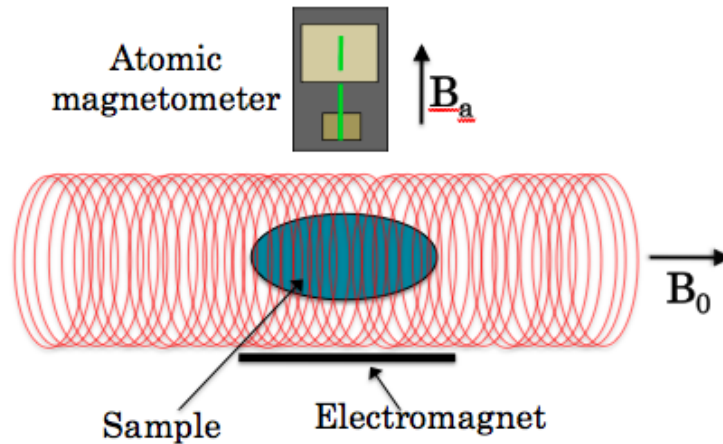


Figure 4.4: RF detection scheme with atomic magnetometer A long solenoid provides a leading field B_0 for the sample nuclei, whereas the alkali atoms do not experience this field. A tunable ac field B_a is applied to the atomic magnetometer so that the atomic precession matches the nuclear precession in order to observe resonance.

has only been reported using remote detection [5, 19, 60]. Some of the results are shown in Figure 4.5. Using the phase-encoding pulse sequence shown in Figure 4.3, and panel B shows the MR image of two tubes with water pre-polarized by a 0.3-T

permanent magnet. The tube diameter is 3 mm and the center-to-center distance is 5 mm. A detection volume of 5.6 μl can be estimated from the image SNR.

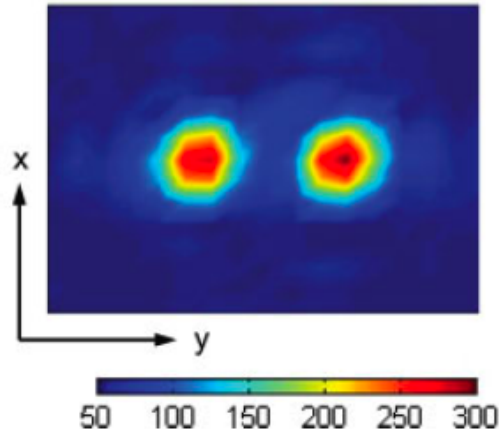


Figure 4.5: Cross-sectional magnetic resonance image of two water-filled channels.

4.3 Basic concepts in contrast MRI

4.3.1 Nuclear magnetic resonance phenomenon

Atoms with unpaired protons and/or neutrons exhibit a nuclear magnetic moment. These species, which are also called 'NMR active', respond to an external magnetic field accordingly. Just like how electrons couple with magnetic field, the energy levels undergo Zeeman splitting, which energy difference is given by the equation:

$$\Delta E_z = \mu_B B g m_j \quad (4.1)$$

where μ_B is the Bohr magneton, g is the Landé factor, m_j is the total angular quantum number, and B is the magnetic field applied. This means that at higher

external fields, the energy splitting is higher. There are two possible orientation of the spins: parallel and anti-parallel. The proportion of these spins is determined by Boltzmann distribution equation:

$$\frac{N^-}{N^+} = e^{-E/kT} \quad (4.2)$$

where N^+ is the population of parallel spins, N^- is the population of anti-parallel spins, E is the energy difference between the spin states and $k=1.3805E^{-23}$ J/K, and T is temperature in Kelvin. Figure 4.6 shows the relationship of the Zeeman split with the strength of magnetic field, as well as the occupancy of the spins.

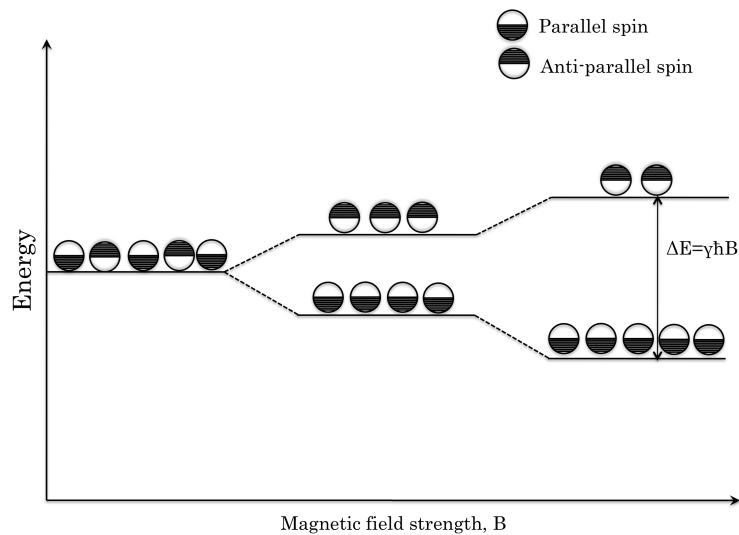


Figure 4.6: Zeeman splitting in nuclear spins. As magnetic field increases, the energy difference between sublevels increases and the number of parallel spins in the lower energy state also increases.

Some NMR active nuclei are ^1H , ^{31}P , and ^{23}Na . For imaging of the body, the detected nuclei is ^1H , since it is the most abundant NMR active species in the body [61].

The nuclear magnetic resonance phenomenon is initialized by exposing a sample

with NMR active species to a static magnetic field B_0 , which is normally applied along the z-axis. In NMR experiments, it is important that the number of parallel spins is greater than the anti-parallel at equilibrium. In addition to using high external magnetic field, low temperature is maintained to achieve this condition. Based on the Boltzmann equation, at room temperature, there is slightly more parallel spins (ground state) than anti-parallel spins (excited state). As temperature decreases, N^-/N^+ also decreases. At high temperatures, this ratio approaches 1. Therefore, to achieve a high net equilibrium magnetization in the ground state, a very low temperature must be maintained.

Magnetic resonance signal is obtained by exposing the polarized spins to an additional field source. After polarization, the nucleus is bombarded with a radiofrequency (rf) field B_1 orthogonal to B_0 . The field applied is $\sim 10^{-5} B_0$. This excites the polarized spins to a higher energy state or pictorially speaking, the spins undergoes precession (Figure 4.7). The spin transition depends on the value of the rf applied. The resonant frequency at which spin precession occurs is the Larmor frequency ω_0 :

$$\omega_0 = B_0 \times \gamma \quad (4.3)$$

where γ is the gyromagnetic ratio of the nucleus. For hydrogen, $\gamma/2\pi = 42.6 \times 10^6$ Hz/T.

When the rf field is turned off, the spins from the higher energy state relax back to their equilibrium state over a period of time. During the relaxation, it emits a resonance signal characterized by the longitudinal (spin-lattice) relaxation time T_1 (Figure 4.8a), given by the equation:

$$M_z(t) = M_0 e^{-t/T_1} \quad (4.4)$$

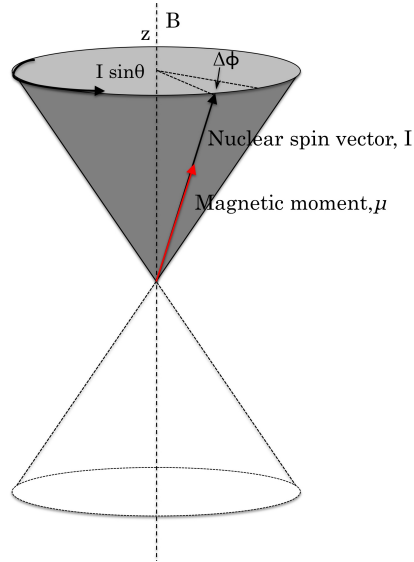


Figure 4.7: Larmor precession of nuclear spins. A radiofrequency field perpendicular to the magnetic field causes the nuclear spin moment to precess around the z-axis.

where M_z is the longitudinal magnetization, M_0 is the equilibrium magnetization, t is the acquisition time. This corresponds to the time when 63% of the spins return to their equilibrium state. After T_1 , the magnetization is fully recovered (Figure 4.8b). T_1 is the relaxation time characterizing the decay along the z-axis of magnetization. The relaxation along the xy plane can be characterized as well, using the transverse (spin-spin) relaxation time T_2 :

$$M_{xy}(t) = M_{xy}(0)e^{-t/T_2} \quad (4.5)$$

where M_{xy} is the transverse magnetization. When the rf field is turned off, the spins begin to dephase and therefore the signal decreases (Figure 4.9). T_2 is approximately ten times smaller than T_1 , since the applied rf pulses are always less than the main external field. The relaxation times, T_1 and T_2 are influenced by the interactions between the nuclei and their effective local magnetic environment in the sample.

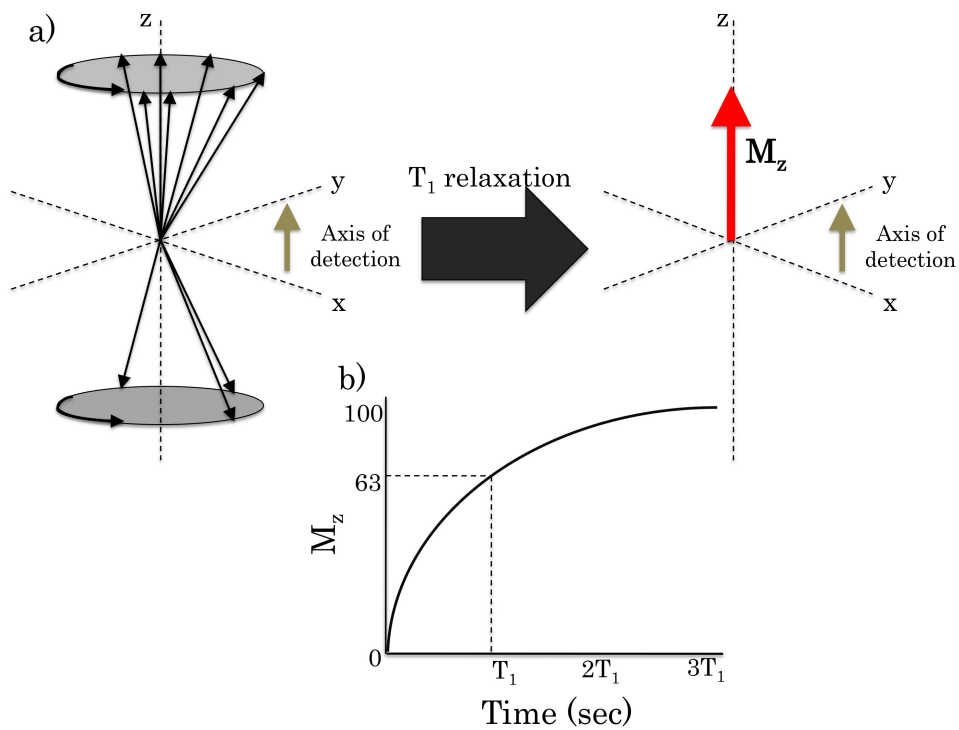


Figure 4.8: a. Spin-lattice (T_1) relaxation of nuclear spins. The recovery of magnetization along the z -axis is measured. b. After time T_1 , 63% of the magnetization returns to equilibrium. At $3T_1$, 100% of magnetization is recovered

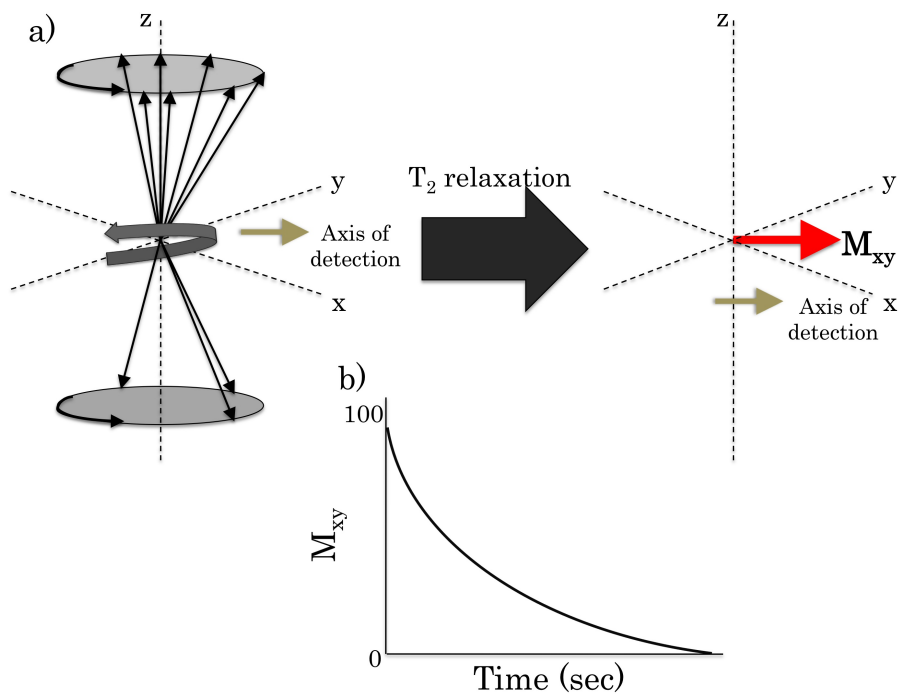


Figure 4.9: a. Spin-spin (T_2) relaxation of nuclear spins. The magnetization along the xy plane is measured. b. After time T_2 the signal along the xy plane decays due to the dephasing of spins.

Thus, factors such as the sample material, homogeneity, and temperature, affect the relaxation. This dependence can be used for the study of different media. Magnetic

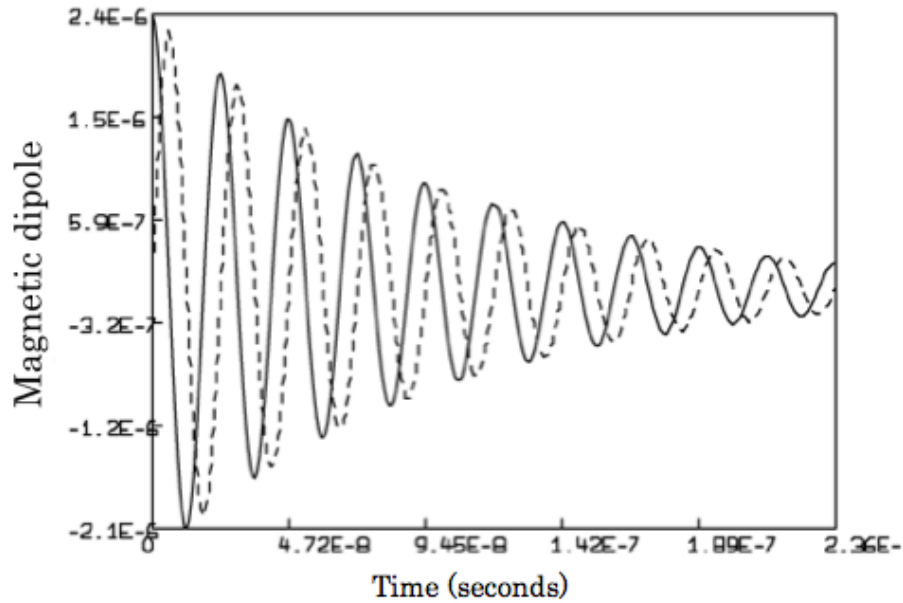


Figure 4.10: Free induction decay signal as detected by the radiofrequency coil. When the rf pulse is turned off, the signal along the transverse plane decreases.

resonance signal is detected by an rf receiver coil, which also produces the rf field for excitation. The rotating magnetization vectors produce an electromotive force on the coil. The signal decreases over time, and so is read by the rf receiver as a free induction decay (FID) signal (Figure 4.10).

For MRI, gradient fields and imaging sequences are used to obtain the magnetic resonance signals at different points. An example of the process is shown in Figure 4.11, Sample A, B and C have high, medium and low magnetic resonance signal, respectively. Since they are along the same x-position, they have the same frequency

of precession. Their y-positions are encoded by applying phase gradients repetitively. When the phase gradient is zero, all the signals are in phase. With a positive phase gradient (applied on A), A has a phase lead while C has a phase lag with respect to B. The opposite happens for a negative phase gradient. All of these raw signals are recovered and analyzed by Fourier transforming the K-space.

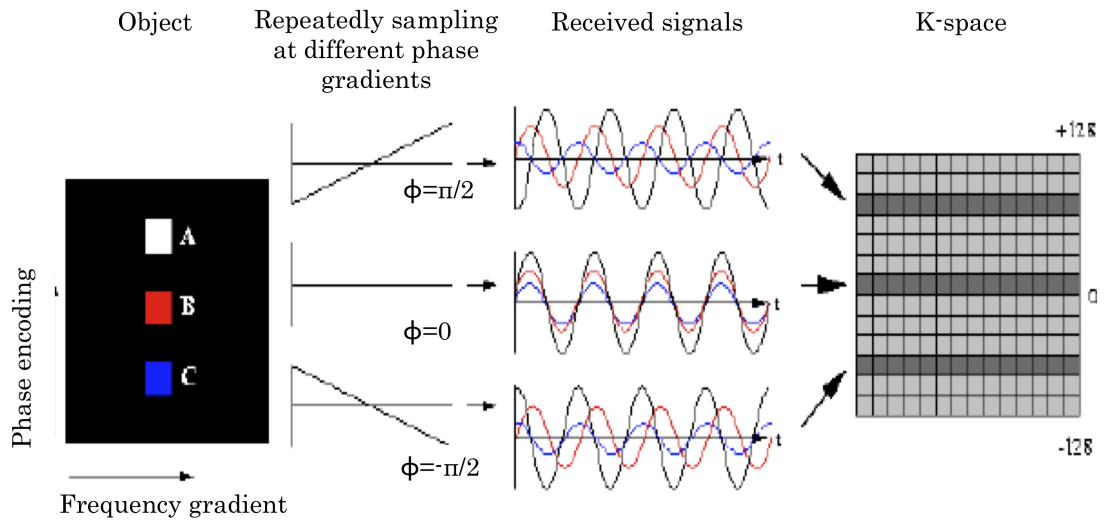


Figure 4.11: Signal encoding using phase-encoding gradients. Signals along the y-positions are encoded by repeated scanning with different phase gradients. K-space records the signal in the presence of gradients.

Each row of the space is assembled together and is collectively converted into an image via Fourier transform (Figure 4.12).

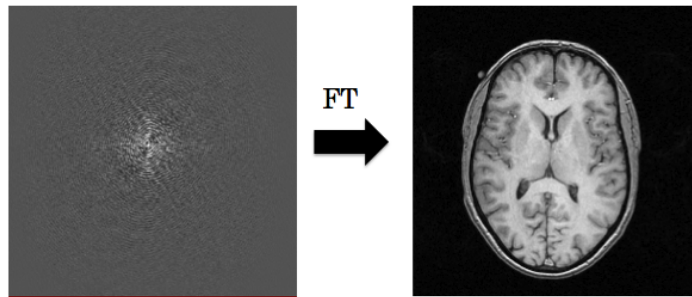


Figure 4.12: Fourier transform of K-space results in a magnetic resonance image.

4.3.2 Contrast magnetic resonance imaging

Imaging with specific contrast is a primary advantage of MRI [62]. In contrast MRI, gadolinium-based contrast agents are commonly used to distinguish different tissues or local environment. They are also called T_1 contrast agents since they enhance T_1 measurements to a greater extent than T_2 agents. Gadolinium is chosen over other paramagnetic ions because of its seven unpaired electrons that make its paramagnetic effect more effective for relaxation. Also, among other lanthanides, its electronic relaxation time (2×10^{-10}) is the longest [63], which means that its electron magnetic moment vector stays along the equilibrium position long enough to be felt by the excited protons surrounding it, resulting in faster nuclear relaxation.

The paramagnetic effect is first experienced by the water molecule directly coordinated to the gadolinium ion (inner-sphere). The effect is transmitted to the water molecules that hydrate the chelate (second-sphere) and to the bulk water (outer-sphere) via dipole-dipole interaction (Figure 4.13). Thus, for a contrast agent to be effective for high-field MRI, it must have at least one water molecule that is directly coordinated to the gadolinium ion, since the inner-sphere water molecule relaxes the

most. However, increasing the number of inner-sphere water molecules may affect the stability of the chelate, which is very important to consider since free gadolinium ions are toxic at physiological conditions. Hence, in designing gadolinium-based contrast agents, both the efficiency and the stability of the chelate are important factors to consider. The efficiency of contrast agents (i.e. relaxivity) does not only depend

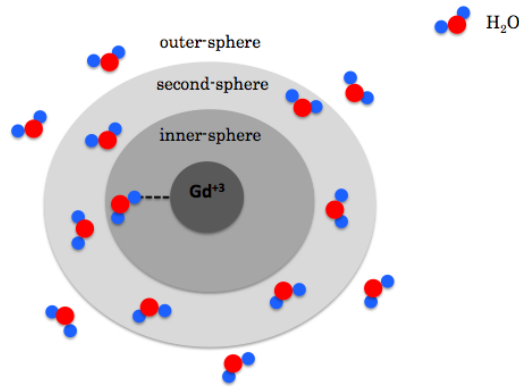


Figure 4.13: Paramagnetic effect of gadolinium ion on water molecules. The inner-sphere experiences a net dipole from the paramagnetic gadolinium ion. This effect is transferred to the outer-sphere molecules.

on the number of inner-sphere water molecules but also on other factors such as the rate of exchange of water molecules, the tumbling rate of the chelate (correlation time), temperature and the applied external field. The relationship between the magnetic field and the T_1 relaxation rate is shown by the Solomon-Boembergen-Morgan equation:

$$\frac{1}{T_{1m}} = \frac{2}{15} \frac{\gamma_H g_e}{m \mu_B} r_{GdH}^6 S(S+1) \left(\frac{7\tau_{c2}}{1 + \omega_s^2 \tau_{c2}^2} + \frac{3\tau_{c1}}{1 + \omega_H^2 \tau_{c1}^2} \right) \quad (4.6)$$

where γ is the nuclear gyromagnetic ratio, g is the electronic factor, μ_B is Bohr magneton, S is the total spin quantum number, ω_s is the electron Larmor precession,

ω_H is the nuclear Larmor precession, τ_{c_1} is the longitudinal correlation time, τ_{c_2} is the transverse correlation time, and r is the electron spin – solvent nuclear spin distance [64]. Based on this equation, the relaxation rate is higher at lower field, since relaxation time increases with the Larmor frequency of protons.

4.4 pH contrast in MRI

An important goal in contrast MRI is to develop contrast agents to highlight specific biochemical environments, e.g., areas with particular ions and pH, as these parameters often serve as indicators for their corresponding diseases. [65, 66, 67]. In particular, a wide range of molecular probes based on paramagnetic ion chelates have been developed for a pH-specific response [68, 69, 70] However, they often exhibit a non-monotonic response in the biologically significant pH range of 6 to 8.5. Another limiting factor is the need of a high concentration of the agents, usually in the range of mM, due to low relaxivity. High concentrations of gadolinium may lead to undesired side effects in biomedical diagnostics [1].

From the NMRD profiles shown in Figure 4.1, it can be seen that the relaxivity for spin-lattice relaxation time (T_1) is much higher in low magnetic fields ($< 1 \mu\text{T}$) than in high fields ($> 0.5 \text{ T}$). This cannot be realized using conventional techniques. Therefore, an alternative detection technique for MRI must be implemented [2]. Furthermore, it remains unclear whether the specific contrast, pH response in this case, is enhanced in low fields compared to high fields.

Here we show that gadolinium triethylenetriamine hexaacetic acid [$\text{Gd}(\text{TTHA})^{3-}$]

exhibits a significant pH response in an ambient magnetic field of $40 \mu\text{T}$, even at concentrations as low as $50 \mu\text{M}$. Although the relaxivity of this chelate has been measured at pH 5 and 9 in $\sim 0.5 \text{ T}$, no study has been carried out in the range of 6 to 8.5 [71]. The exceptionally low relaxivity in such a high field has prohibited its application in pH contrast imaging. We show that the pH response is monotonic in this pH range in ambient magnetic field of $40 \mu\text{T}$. The relaxivity was slightly greater compared to results in a high field. By directly measuring the proton magnetization with an atomic magnetometer [43], the pH of an unknown solution was revealed by this molecular probe. Multiple channels can be monitored simultaneously by measuring magnetization at a single location, with the aid of a gradient magnetic field.

4.4.1 Experimental section

We used the remote detection technique to detect the magnetization of our sample. This allows us to obtain optimum parameters for each region without affecting the other. There are three regions in a remote detection configuration namely, pre-polarization, encoding and detection.

In the pre-polarization region, water molecules are magnetized through flowing through a compact 2T-permanent magnet enclosed in an aluminum magnetic shield. A sample holder is situated in the bore of the magnet. The sample holder is made of brass rod and contains a $5 \mu\text{m}$ porous material to enable the liquid sample to remain in the magnetizing region while keeping the same flow rate. Water then flows through

the encoding region. In the encoding region, rf pulses are sent to excite the nuclear

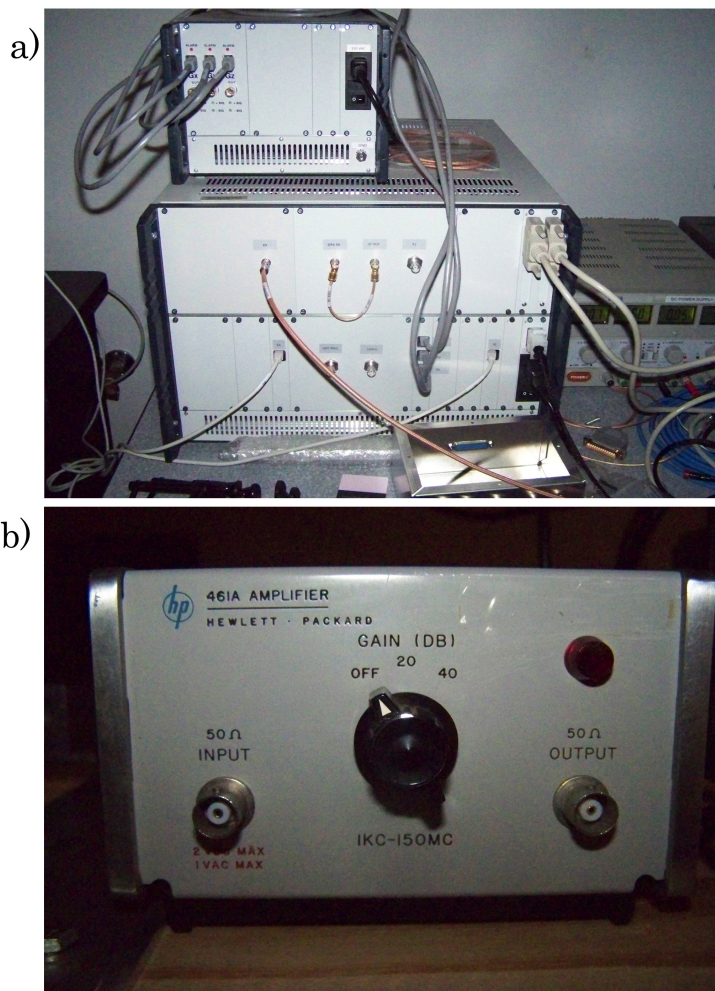


Figure 4.14: a. Tecmag LF1 Apollo unit for sending rf pulses. b. Rf amplifier.

spins of the sample. The rf pulse is generated and sent by Tecmag LF1 Apollo (Figure 4.14a), which is amplified using the HP 461A amplifier (Figure 4.14b). A saddle coil wound around a teflon tube drives the rf signal. The saddle coil is compact, easily constructed and can generate a uniform magnetic field perpendicular to the axis of

cylinder. The configuration produces a magnetic field in the x-axis (Figure 4.15). We used the optimum configuration of the saddle coil, which has the optimum angle at 60° and the ratio length/diameter=1.41 for best rf field homogeneity [72]. The saddle coil used in our experiment has length=2.0 in and diameter=1.42 in.

To obtain images, we used gradient coils with a similar pulse sequence used by Xu and co-workers [5]. The strength of the magnetic field was varied in a controlled manner to provide spatial information about the MR images. The gradient coils vary the magnetic field and are powered by a gradient amplifier. These coils vary the magnetic fields in the three spatial orientations x, y and z across the imaging volume where G_x and G_y are known as transverse gradients and G_z is called a longitudinal gradient. This makes it possible to determine a map of spin density in the sample region.

Our gradient coil design consists of a Maxwell pair where the current flows in opposing directions in the two coils, and produces a magnetic field gradient that varies linearly with the z axis. With a distance between the loops chosen to be $a\sqrt{3}$, a simple calculation shows that this gradient is uniform up to 5% within a sphere of radius $0.5a$ and, at the center, the gradient efficiency is $\eta = 8.058 \times 10^{-7} a^2 T m^{-1} A^{-1}$.

The x and y gradient coil design consists of Golay or double-saddle arrangement, which consists of four saddles on the surface of the encoding region(Figure 4.16). This configuration produces a linear variation in the magnetic field along the x and y axis and a linear field at the central plane, and the wires parallel to the z-axis do not produce a z-component of magnetic field, which does not affect the gradient field. The gradient is uniform to 5% within a sphere of radius $0.4a$. The efficiency is

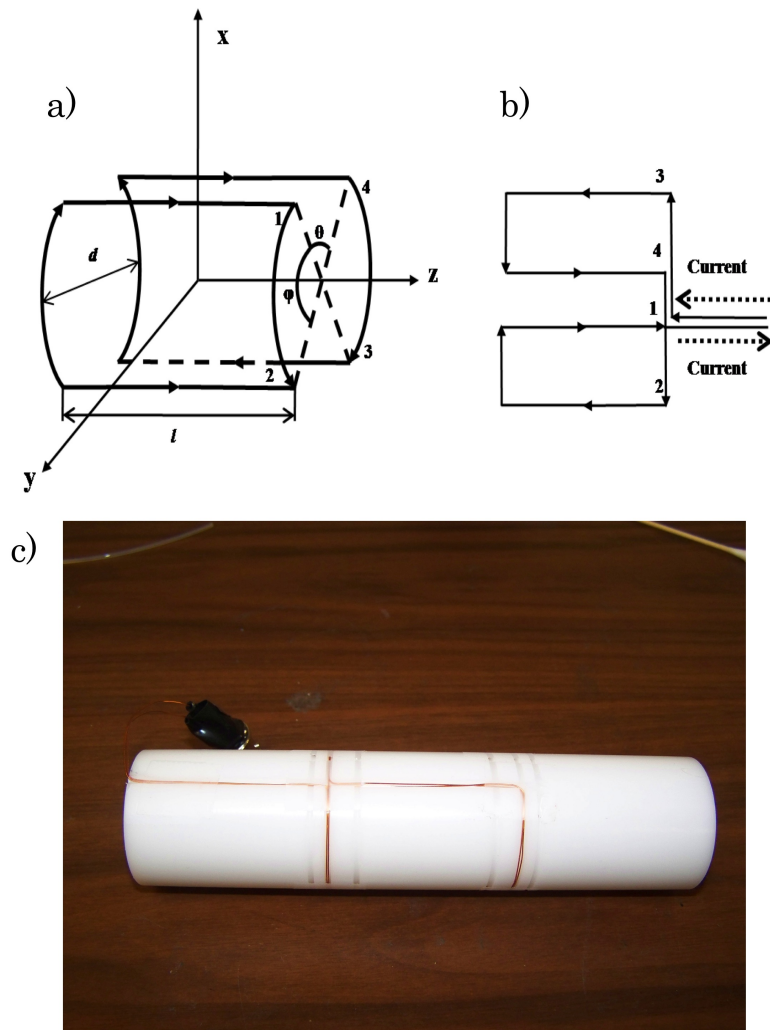


Figure 4.15: a. Saddle coil configuration. Optimum angle was $\theta = 60^\circ$; length/diameter = 1.41 b. Direction of current flow. c. Saddle coil on a Teflon tube.

given $\eta = 9.18 \times 10^{-7} \text{a}^2 \text{Tm}^{-1} \text{A}^{-1}$.

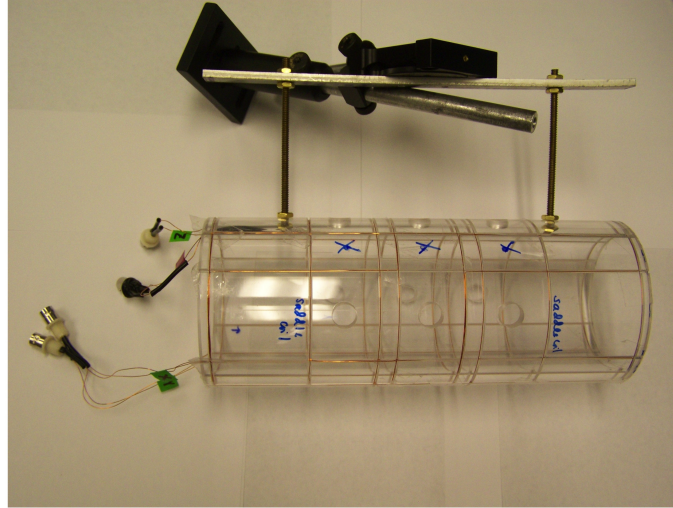


Figure 4.16: Gradient coils wound around a plastic tube. Length and dimensions are measured based on the efficiency parameters.

The sample flows through the encoding region to the detection region via a copper tube with a cap that can hold $140 \mu\text{L}$ of sample. The magnetization of spin is directed into the region via a leading field of 0.5 G produced by the piercing solenoid. The direction of detection was set by applying a bias field (Figure 4.17). This enables both of the sensors to detect the magnetization of the flowing sample.

Based on equation 3.1, it can be noted that the magnetic field strength exerted by the sample, B_s , on the detectors is inversely proportional to the distance r^3 . Therefore the sample holder is placed in an optimal position to detect high magnetization signal. With the orientation of the sensors, the magnetization signal from both sensors can be added and the common mode noise can be cancelled [1]. Unlike traditional nuclear

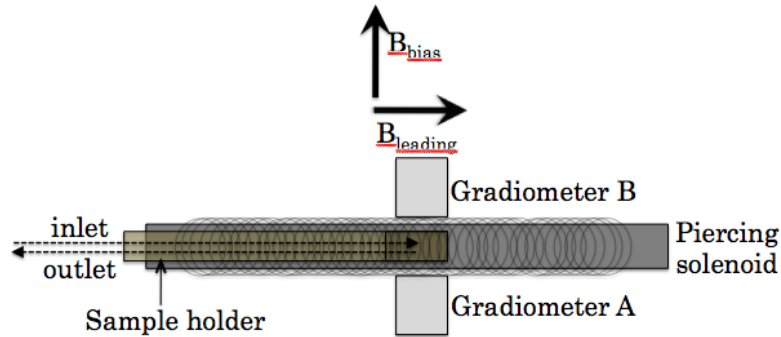


Figure 4.17: Detection region of the remote detection scheme. A copper tube holds the sample to be measured. Detection axis is define by a bias field.

magnetic resonance devices, a pick-up coil is not needed. The sensors can directly measure the magnetization of the sample

A microannular gear pump is used to drive the water flow. We use a beaker as a reservoir of the sample, both before the pump and after the detection region. With this set-up, a minimum amount of sample can be used and recycled. Figure 4.18 shows the over-all picture of the set-up. A 3-way pulsed valve was implemented to perform the stopped-flow measurements to obtain relaxation times(Figure 4.19). The valve allowed the direct measurement of the T_1 relaxation time of water. TECMAG directs the timing of the stopping and the flowing of the sample via the valves using the pulse sequence in Figure 4.20. The resonance frequency is 1.73 kHz. The duration for the $\pi/2$ pulses is 4.5 ms. The duration for the gradient is 5 ms. We only obtained 1-D images of samples. The imaging phantom is composed of two parallel channels inside a plastic cylinder. Each channel is cylindrical with 3.2 mm diameter and 15 mm length. The center-to-center spacing between the two channels is 8.3 mm. One channel is filled with a volume reducer to show a difference from the other channel.

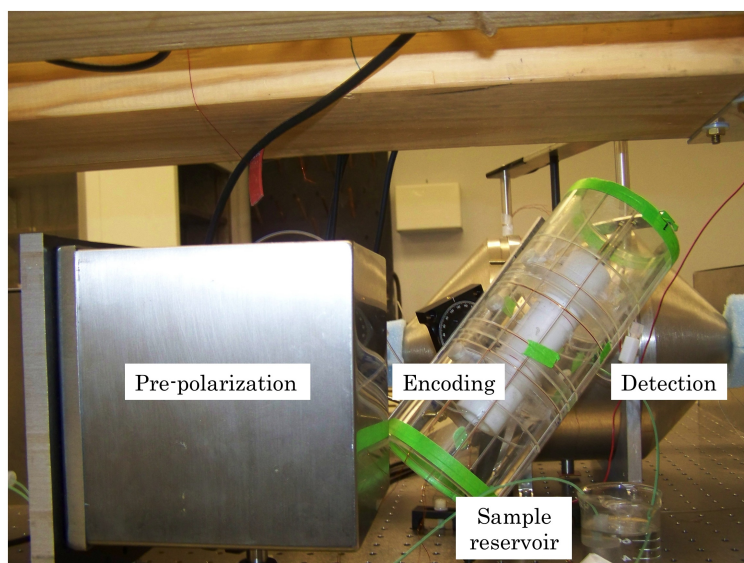


Figure 4.18: Remote detection setup. Sample is driven by a micropump (not shown) and is recycled back to the reservoir.

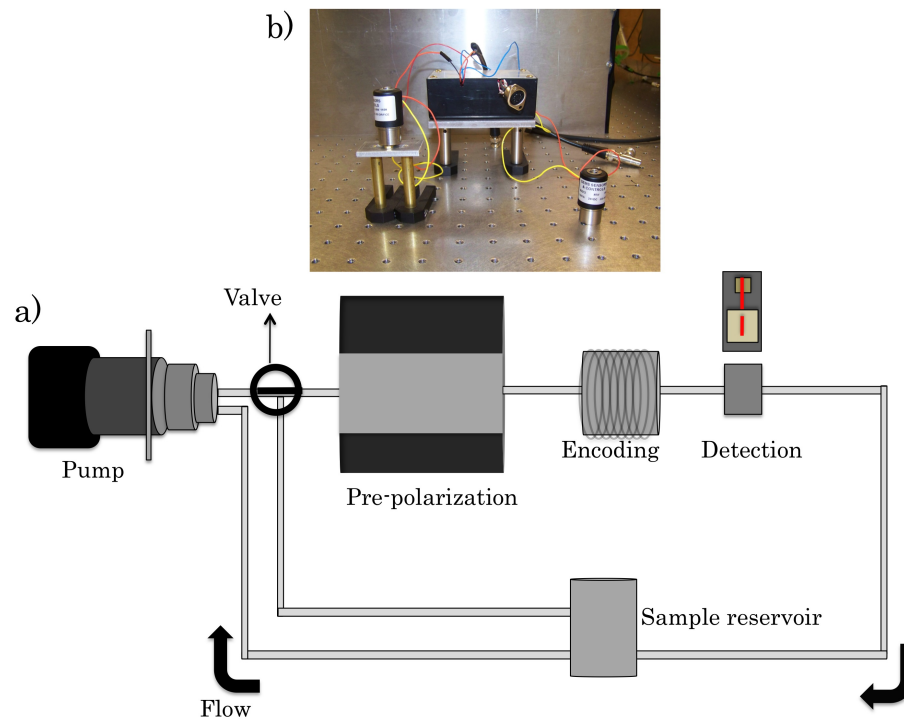


Figure 4.19: a. Stopped-flow scheme. b. Valve stops the flow in a systematic manner.

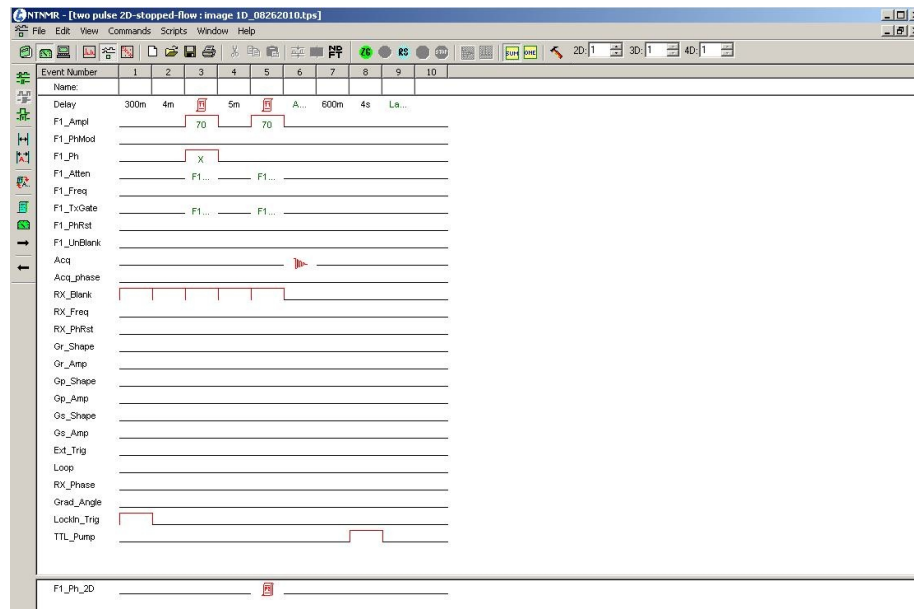


Figure 4.20: Pulse sequence for the stopped-flow experiment.

4.4.2 Matlab scripts

Using the MATLAB script below, the average water signal was obtained.

```
clearall;  
[FileName, PathName] = uigetfile('*.',' Selectthedatafile');  
pathfile = [PathName, FileName];  
lock = importdata(pathfile);  
prompt = ('Enter number of deleting sections :');  
dlg_title = ' Input';  
num_lines = 1;  
def = '0';  
answer = inputdlg(prompt, dlg_title, num_lines, def);  
if str2num(answer1) == 0  
else  
for k = 1 : str2num(answer1)  
prompt = 'Enter Begin Position :',' Enter End Position :';  
dlg_title = ' Input positions of unuseful data';  
num_lines = 1;  
def = '20',' 50';  
answer = inputdlg(prompt, dlg_title, num_lines, def);  
lock(str2num(answer1) : str2num(answer2), :) = [];  
end  
end  
prompt = 'Enter peak difference :';
```

```

dlg_title = ' Input';
num_lines = 1;
def = '3.500e - 03';
answer2 = inputdlg(prompt, dlg_title, num_lines, def);
diff = str2num(answer2);
M = [ ];
index = 0;
k = 0;
size = 50;
X = zeros(5, 1);
G = zeros(size, 2);
M(:, 1) = lock(:, 1);
M(:, 2) = lock(:, 4);
M(:, 3) = lock(:, 5);
for n = 2 : length(M);
if (M(n, 3) < 3)&(M(n - 1, 3) > 3);
index = index + 1;
k = 1;
end;
if (index > 0)&(k <= size);
if n > 4
for m = 1 : 5
X(m) = M(n + m - 5, 2);

```

```

end
if M(n,2) > mean(X) + 3 * std(X)
M(n,2) = mean(X);
else if M(n,2) < mean(X) - 3 * std(X)
M(n,2) = mean(X);
else M(n,2) = M(n,2);
end
end
end
if index == 1;
G(k,1) = M(n,1);
end;
G(k,2) = G(k,2) + M(n,2);
k = k + 1;
end;
end;
t0 = G(1,1);
b0 = G(1,2)/index * 100/diff;
for m = 1 : length(G);
G(m,1) = G(m,1) - t0;
G(m,2) = G(m,2)/index * 100/diff - b0;
end;
for m2 = 1 : 10

```

```

Y(m2) = G(size + m2 - 10, 2);
end
form = 1 : length(G);
G(m, 2) = G(m, 2) - mean(Y)/G(size - 5, 1) * G(m, 1);
end;
figure; plot(G(:, 1), G(:, 2))
minposition = find(G(:, 2) == min(G(:, 2)));
avgsig = mean(G(minposition - 5 : minposition + 5, 2))

```

On the other hand, one-dimensional images were obtained using the following MATLAB script:

```

clearall;
step = 11;
rawdata = importdata(pathfile);
M(:, 1) = rawdata(:, 1);
M(:, 2) = rawdata(:, 4);
M(:, 3) = rawdata(:, 5);
hu = [ ];
index = 0;
for n = 2 : length(M);
if M(n, 3) < &&M(n - 1, 3) > 3;
if index == 0
start = n;
end

```

```

index = index + 1;
hu(1, index) = n;
end
end

data1 = [ ];
data2 = data1;
data3 = data1;
data4 = data1;
tri_back = 15;
for i = 1 : 1 : index/step/4
dlength = length(M(hu(1 + (i - 1) * 4 * step) - tri_back + 1 : hu(1 + (i - 1) * 4 *
step + step) - tri_back, :));
data1(1 + (i - 1) * dlength : i * dlength, :) = M(hu(1 + (i - 1) * 4 * step) - tri_back + 1 :
hu(1 + (i - 1) * 4 * step + step) - tri_back, :);
dlength = length(M(hu(1 + (i - 1) * 4 * step + step) - tri_back + 1 : hu(1 + (i - 1) *
4 * step + 2 * step) - tri_back, :));
data2(1 + (i - 1) * dlength : i * dlength, :) = M(hu(1 + (i - 1) * 4 * step + step) -
tri_back + 1 : hu(1 + (i - 1) * 4 * step + 2 * step) - tri_back, :);
dlength = length(M(hu(1 + (i - 1) * 4 * step + 2 * step) - tri_back + 1 : hu(1 + (i -
1) * 4 * step + 3 * step) - tri_back, :));
data3(1 + (i - 1) * dlength : i * dlength, :) = M(hu(1 + (i - 1) * 4 * step + 2 * step) -
tri_back + 1 : hu(1 + (i - 1) * 4 * step + 3 * step) - tri_back, :);
if i == index/step/4

```

```

dlength = length(M(hu(1 + (i - 1) * 4 * step + 3 * step) - tri_back + 1 : end, :));
data4(1 + (i - 1) * dlength : i * dlength, :) = M(hu(1 + (i - 1) * 4 * step + 3 * step) -
tri_back + 1 : end, :);
else
dlength = length(M(hu(1 + (i - 1) * 4 * step + 3 * step) - tri_back + 1 : hu(1 + (i -
1) * 4 * step + 4 * step) - tri_back, :));
data4(1 + (i - 1) * dlength : i * dlength, :) = M(hu(1 + (i - 1) * 4 * step + 3 * step) -
tri_back + 1 : hu(1 + (i - 1) * 4 * step + 4 * step) - tri_back, :);
end
end
peakadd = zeros(step, 4);
for r = 1 : 4;
if r == 1
lock = data1;
else if r == 2
lock = data2;
else if r == 3
lock = data3;
else
lock = data4;
end
end
end

```

```

M = [];
index = 0;
index2 = 0;
k = 1;
d = 0;
t_travel = 0.97;
s = 20;
X = zeros(5, 1);
G = zeros(s, 2, step);
peak = zeros(step, 2);
M(:, 1) = lock(:, 1);
M(:, 2) = lock(:, 2);
M(:, 3) = lock(:, 3);
for n = 2 : length(M);
if M(n, 3) < 3 && M(n - 1, 3) > 3;
index = index + 1;
k = 1;
if mod(index - 1, step) == 0
index2 = index2 + 1; r;
end
d = mod(index - 1, step) + 1;
end
if index2 > 0 && k <= s

```

```

if n > 4
for m = 1 : 5
X(m) = M(n + m - 5, 2);
end
if M(n, 2) > mean(X) + 3 * std(X)
M(n, 2) = mean(X);
else if M(n, 2) < mean(X) - 3 * std(X)
M(n, 2) = mean(X);
else M(n, 2) = M(n, 2);
end
end
end
if index2 == 1
G(k, 1, d) = M(n, 1);
end
G(k, 2, d) = G(k, 2, d) + M(n, 2);
k = k + 1;
end;
end;
if index2 > 0
for n = 1 : step
t0 = G(1, 1, n);
peak(n, 1) = n;

```

```

b01 = (G(1, 2, n) + G(2, 2, n) + G(3, 2, n) + G(4, 2, n) + G(5, 2, n))/5 * 2e12;
b02 = (G(s-1, 2, n)+G(s-2, 2, n)+G(s-3, 2, n)+G(s-4, 2, n)+G(s, 2, n))/5*2e12;
for m = 1 : s
G(m, 1, n) = G(m, 1, n) - t0;
G(m, 2, n) = (G(m, 2, n) * 2e12 - b01 - G(m, 1, n) * (b02 - b01)/G(s, 1, n))/index2;
if m > 5&&G(m, 1, n) >= t_travel&&G(m - 1, 1, n) < t_ravel
peak(n, 2) = G(m, 2, n)+(G(m, 2, n)-G(m-1, 2, n))*(t_travel-G(m, 1, n))/(G(m, 1, n)-
G(m - 1, 1, n));
peak_position = m;
end;
end;
end;
end;
end;
peakadd(:, r) = peak(:, 2);
end;
a1 = peakadd(:, 1); a2 = peakadd(:, 2); a3 = peakadd(:, 3); a4 = peakadd(:, 4);
real = (a1 - a2)/2; imag = (a3 - a4)/2;
total = real + sqrt(-1) * imag;
b = fftshift(fft(total, 2 * step, 1), 1);
figure; plot(abs(b));
aaa = abs(b);
save file.txtaaa - ASCII

```

4.4.3 Results and discussion

A typical flow profile is shown in Figure 4.21, in which the time of detection in seconds is plotted against the magnetic field detected from the sample. The dispersion curve is obtained by averaging 100 measurements after applying a single π pulse. The static magnetization is obtained from the peak of the dispersion curve, where the signal detected is at its maximum. For pure water, we obtained a signal of 28.5 pT, which is six times better than previous report [5].

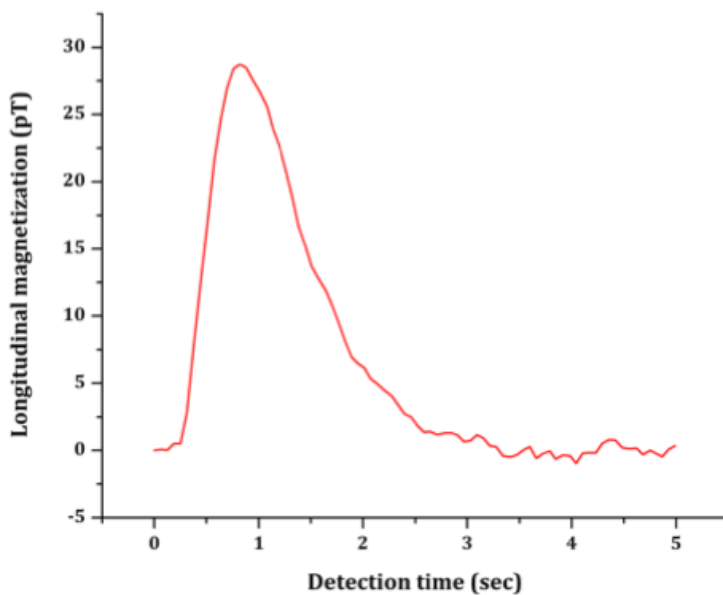


Figure 4.21: Flow profile of water in remote detection scheme. The magnetization is recorded from the maximum signal detected in the curve.

We measured the magnetization of 100 μM $\text{Gd}(\text{TTHA})^{3-}$ at several pH using $\text{NaH}_2\text{PO}_4/\text{Na}_2\text{HPO}_4$ buffer (Figure 4.22, blue). For comparison, the magnetization of 100 μM gadolinium diethylenetriamine pentaacetic acid [$\text{Gd}(\text{DTPA})^{2-}$] was also

measured within the same pH range (Figure 4.22, red). The detection volume was 140 μl . These measurements showed that while $\text{Gd}(\text{DTPA})^{2-}$ had no response to pH, the magnetizations for $\text{Gd}(\text{TTHA})^{3-}$ increased monotonically as pH increased. Thus, the relaxivity of $\text{Gd}(\text{TTHA})^{3-}$ decreased when pH increased, while that of $\text{Gd}(\text{DTPA})^{2-}$ remained constant. This observation was consistent with the high-field results [71].

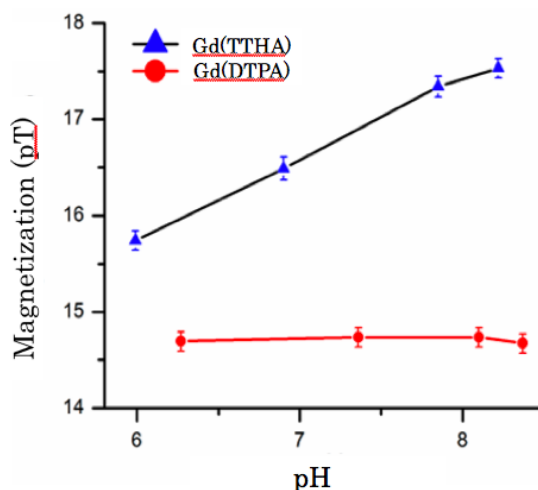


Figure 4.22: pH responses of $\text{Gd}(\text{TTHA})^{3-}$ and $\text{Gd}(\text{DTPA})^{2-}$. $\text{Gd}(\text{TTHA})^{3-}$ showed a non-monotonic response, a characteristic property for tumor sensing.

To quantify the relaxivity of $\text{Gd}(\text{TTHA})^{3-}$ as a function of pH, we used a stopped-flow scheme to directly measure T_1 of the sample solutions: after pre-polarization, the sample was held in the detection region by switching the three-way valve to the bypass path. Because the valve had a response time of 20 ms, this method was more accurate for measuring T_1 compared to stopping the pump which had a response time of $\sim 2\text{s}$. In addition, the three-way valve maintained constant flow rate for the pump to reduce mechanical noise in contrast to a two-way valve.

Because the relaxivity of $\text{Gd}(\text{DTPA})^{2-}$ did not change with pH, we measured its relaxivity at pH=7.5 and used this value to calibrate the relaxivity of $\text{Gd}(\text{TTHA})^{3-}$ at different pH values. Figure 4.23 shows the two relaxation traces of pure water (black) and 100 μM $\text{Gd}(\text{DTPA})^{2-}$ (red). Fitting the data with an exponential decay produced T_1 3.00 \pm 0.17 s for pure water and 1.03 \pm 0.08 s for 100 μM $\text{Gd}(\text{DTPA})^{2-}$. Therefore, the relaxivity for $\text{Gd}(\text{DTPA})^{2-}$ was determined to be 6.4 \pm 0.9 $\text{s}^{-1}\text{mM}^{-1}$. This value agreed well with literature [57].

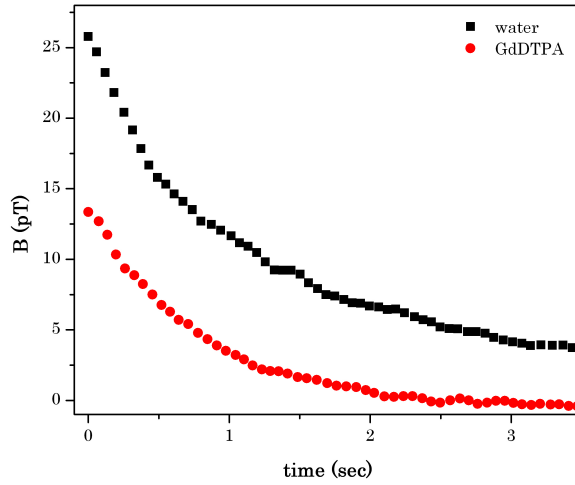


Figure 4.23: T_1 relaxation profiles of pure water and 100 μM $\text{Gd}(\text{DTPA})^{2-}$

The relaxivity, α , is defined as

$$\frac{1}{T_1} = \frac{1}{T_{1,0}} + \alpha C \quad (4.7)$$

where T_1 is the relaxation time with the contrast agent, $T_{1,0}$ is the relaxation time of pure water, C is the concentration of the contrast agent. Therefore, relaxivity can

be calculated as

$$\alpha = \frac{1}{C}(1/T_1 - 1/T_{1,0}). \quad (4.8)$$

Given $C = 100 \text{ M}$, $T_1 = 1.03 \pm 0.08 \text{ s}$, $T_{1,0} = 3.00 \pm 0.17 \text{ s}$, we obtain $\alpha = 6.4 \pm 0.9 \text{ s}^{-1} \text{mM}^{-1}$.

The relaxivity of $\text{Gd}(\text{TTHA})^{3-}$ at different pH is calibrated using the above value. The relaxation of the three samples, pure water, $\text{Gd}(\text{DTPA})^{2-}$ solution, and $\text{Gd}(\text{TTHA})^{3-}$ solution, follow

$$M(\text{water}) = M_0 e^{-t/T_{1,0}} \quad (4.9)$$

$$M(\text{Gd}(\text{DTPA})^{2-}) = M_0 e^{-t1/T_{1,0} + \alpha_1 C} \quad (4.10)$$

$$M(\text{Gd}(\text{TTHA})^{3-}) = M_0 e^{-t1/T_{1,0} + \alpha_2 C}. \quad (4.11)$$

The three solutions have the same M_0 because of the same sample volume. They also have the same relaxation time t because of the same flow rates. α_1 and α_2 are relaxivities for $\text{Gd}(\text{DTPA})^{2-}$ and $\text{Gd}(\text{TTHA})^{3-}$, respectively. Combining equations 4.9 and 4.10 gives

$$\alpha_2 = \frac{\ln(M_2/M)}{\ln(M_1/M)} \alpha_1. \quad (4.12)$$

This method eliminates the influence on relaxivity by the flow time and the sample volume, which would otherwise impose a significant uncertainty to the relaxivity

value. The results are plotted in Figure 4.24. From the relaxivity change, we deduced the pH-sensitivity of $\text{Gd}(\text{TTHA})^{3-}$ as $0.6 \text{ s}^{-1}\text{mM}^{-1}$ per pH unit in $40 \mu\text{T}$, which was slightly higher than 0.4 in high fields [71]

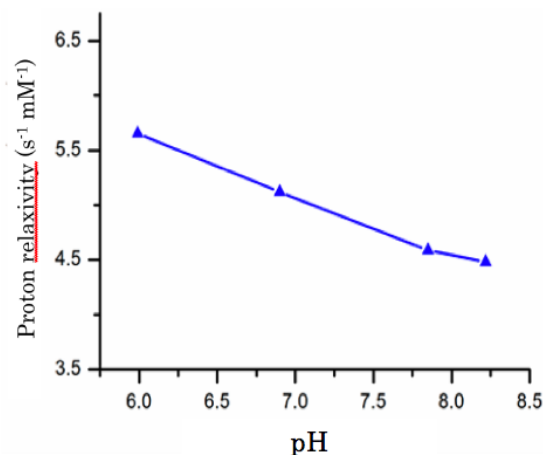


Figure 4.24: Relaxivity of $\text{Gd}(\text{TTHA})^{2-}$ vs pH

To illustrate the high pH-sensitivity, we measured the magnetization of $50 \mu\text{M}$ $\text{Gd}(\text{TTHA})^{3-}$ solution at several known pH values controlled by buffer and one unknown pH (Figure 4.25). The point in magenta is the solution with an unknown pH value. From the calibration curve, a pH of 7.7 was obtained for the unknown solution, which was in excellent agreement with 7.61 obtained by a glass pH meter. The concentration of $50 \mu\text{M}$ was at least one order of magnitude lower than clinically used concentrations. In addition, $\text{Gd}(\text{TTHA})^{3-}$ had excellent safety profile because the toxic gadolinium ion is fully coordinated. These two factors made $\text{Gd}(\text{TTHA})^{3-}$ a well-suited pH probe.

To demonstrate the applications of this pH probe in MRI, we made a two-channel phantom with different volumes and used remote detection for imaging [5]. Using

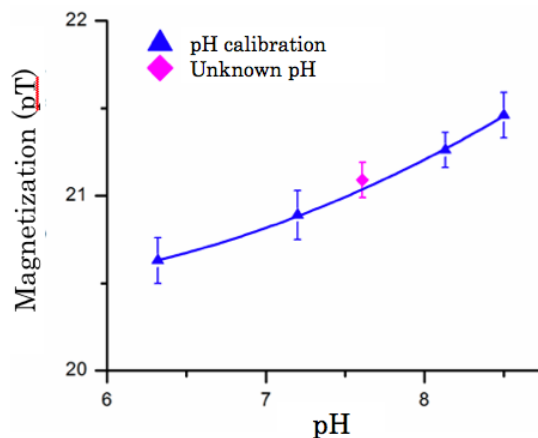


Figure 4.25: pH response of $\text{Gd}(\text{TTHA})^{3-}$ at $50 \mu\text{M}$

a gradient of $0.33 \mu\text{T}/\text{m}$, one-dimensional images were obtained with water and $150 \mu\text{M}$ $\text{Gd}(\text{TTHA})^{3-}$ (Figure 4.26). Because the two channels had the same pH, the same degree of signal change was expected for the channels switching from water to $\text{Gd}(\text{TTHA})^{3-}$.

From the areas of the profiles for each channel using water then $\text{Gd}(\text{TTHA})^{3-}$, we deduced a signal decrease of 55% for the left channel and 54% for the right channel. This indicated that the relaxivities of $\text{Gd}(\text{TTHA})^{3-}$ were identical in the two channels, consistent with the same pH values. Therefore, $\text{Gd}(\text{TTHA})^{3-}$ may serve as a robust pH probe in MRI.

The above example also shows that MRI with a molecular probe is capable of mapping pH with a single detector. This is more desirable than implementing multiple detectors at each location, because some locations may not be physically reachable to the detector. Using a molecular probe is minimally invasive and causes little disturbance to the system under study, especially at a low concentration of $50 \mu\text{M}$.

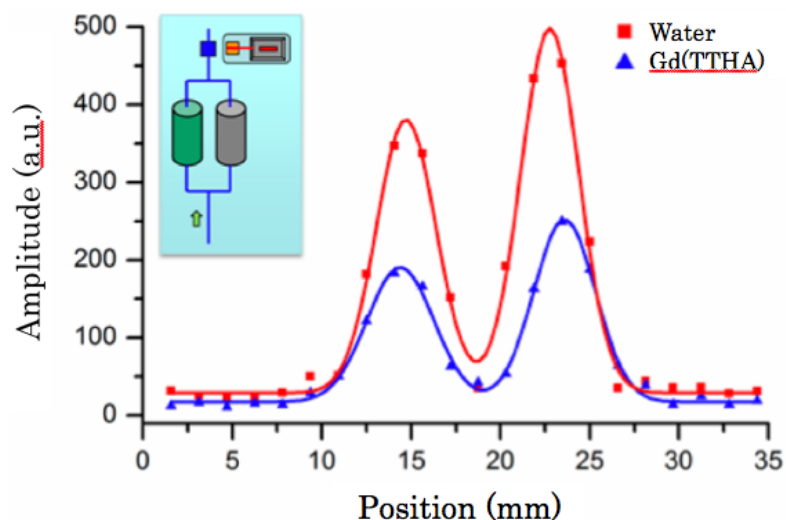


Figure 4.26: One-dimensional MR images of a two-channel phantom (inset) with pure water and $150 \mu\text{M}$ $\text{Gd}(\text{TTHA})^{3-}$.

In addition, MRI in ambient magnetic field removes the constraints on the size and magnetic homogeneity requirement for the samples in high-field MRI.

The sensitivity of the atomic magnetometer can be improved, which will lead to a lower concentration of $\text{Gd}(\text{TTHA})^{3-}$ needed for measuring pH or a smaller detection volume. A sensitivity of $0.5 \text{ fT}/\text{Hz}^{1/2}$ has been reported, [14] corresponding to 1.5 nl pre-polarized water at 1 T at 1 cm from the magnetometer [11]. This may theoretically reduce the required concentration of $\text{Gd}(\text{TTHA})^{3-}$ needed by two orders of magnitude.

Based on the results, we reveal $\text{Gd}(\text{TTHA})^{3-}$ as viable to be a molecular probe for pH detection in an ambient magnetic field. With a sensitive atomic magnetometer for detection, pH discrimination is achieved with a low concentration of $50 \mu\text{M}$. One-dimensional MRI showed that the spatially resolved pH measurement could be

obtained using a single detector.

4.5 Challenges and possible solutions

Researches have proven that atomic magnetometers can offer the highest sensitivity in detecting magnetic fields and are suitable for NMR detection and contrast MRI. However, there are still challenges that need to be addressed to further its application to magnetic resonance. The three major issues are the size of the magnetic shield, maintaining the cell temperature, and increasing the spin time coherence of the atomic cell.

1. Magnetic shield elimination

The multiple-layer magnetic shield used by most atomic magnetometers is to ensure a relatively noise-free and field-free environment. While it has been effective in eliminating noise and unnecessary field, its size is an issue if we want to improve the accessibility of the instrument. The shield makes atomic magnetometers much larger than the atomic cells. Although progress in miniature magnetic shields has been reported [73], it would be ideal if no magnetic shields were used at all.

Several approaches have been undertaken to pursue a shield-free magnetometer. One method uses a set of balancing coils with feedback control to cancel out the magnetic field of the laboratory. With this technique, a sensitivity of $1 \text{ pT}/\text{Hz}^{1/2}$ has been achieved [74]. The authors predicted that the sensitivity could be substantially improved by reducing high-frequency magnetic noise and magnetic field gradients

across the cell.

Another method involves directly operating an atomic magnetometer in the Earth's magnetic field. Acosta and co-workers studied a magnetometer that operated at a field of $\sim 40 \mu\text{T}$, which is provided by a set of coils enclosed in magnetic shields [75]. They achieved an estimated sensitivity of $60 \text{ fT}/\text{Hz}^{1/2}$. The degraded sensitivity is attributed to the nonlinear Zeeman splitting of the atomic levels. In a magnetic field of $\sim 10 \mu\text{T}$ or higher, the nonlinear term in the Zeeman effect is no longer negligible, which removes the degeneracy of transitions with the same Δm_F . Therefore, the magneto-optical resonance becomes more complicated and less outstanding for each transition. The overall broadened feature results in a lower sensitivity.

The nonlinear Zeeman effect can be minimized using various methods. Seltzer and co-workers showed that by using a second modulation, the sensitivity loss due to nonlinear Zeeman splitting could be largely recovered [76]. For a potassium magnetometer, they showed that the sensitivity improved by a factor of four. Recently, Jensen and co-workers reported an approach that utilized light shift to overcome the nonlinear Zeeman effect [77]. In this method, an additional laser beam with the appropriate frequency, polarization, and power was introduced to the atomic cell. The multiple magnetic resonances due to the nonlinear Zeeman effect became a single resonance feature in the presence of a magnetic field of 0.397 G . The sensitivity was thus improved, although it was still significantly lower than that of the shielded magnetometers that operate in a near-zero magnetic field.

2. Heating method

As we can see from Equation 4.1, a sufficient number of gaseous atoms is required to achieve a desirable sensitivity. Therefore, most atomic magnetometers operate at an elevated temperature, especially when the atomic cell is rather small. Thus far, two heating methods have been employed: electro-resistive heating and hot air blowing. In the first option, heaters are placed close to the detectors for optimal heating efficiency. However, the magnetic field generated by the electric current in the heaters overwhelms the signal from the sample. Thus the heating current must be turned off while measurements are taken. This causes sensitivity degradation due to temperature fluctuation. The measurement duty cycle is also poor because measurements cannot be performed when the heaters are on. Several approaches have been demonstrated to reduce noise associated with heating. For low-frequency magnetometer, Xu et al., [40] placed the heating wires outside of the inner most layer of the magnetic shields. For RF magnetometers, an ac current with a frequency outside the magnetometers bandwidth can be used [78].

The second option, heating via blowing hot air, introduces air turbulence along the optical path of the magnetometer and consequently causes undesired polarization changes to the laser beam. By using vacuum tubes for the optical path, such turbulence is largely avoided.

3. Increasing spin coherence time for a small cell

From Equation 4.3, we see that a smaller magnetometer will have a higher SNR for NMR applications. However, compared to larger cells, the more frequent collisions between polarized atoms and the wall in smaller cells result in a loss of coherence and, hence, a decreased coherence time τ . Based on the discussion above, there are

two ways to decrease the collisions between the atoms and the wall. One method is the application of a cell coating, and the other is the introduction of a buffer gas. Despite significant progress, additional study is necessary in order to further increase the coherence time of the polarized atoms. For instance, a coating that has a higher melting point and weaker interactions with the atoms is worthy of exploration [41].

In addition to the above-mentioned issues, there are some other critical parameters to be explored. One example is the recovery time of the atomic polarization after the excitation pulse. Romalis group [4, 79] showed that with a countering field counter to the excitation field, the recovery time of atomic magnetometers can be shortened to less than 1 ms. Another example is the development of low-cost lasers to replace stabilized lasers, thus facilitating multiplexing of atomic magnetometers. Vertical cavity surface emitting lasers (VCSELs) have been used for this purpose [80]. The results at this time are still not as impressive as those obtained with a stabilized laser, most likely because the VCSELs were not frequency-stabilized. Further research is thus needed to overcome these limitations.

Chapter 5

Applications of atomic magnetometry in magnetic molecular sensing

This chapter presents the application of atomic magnetometry in detecting magnetically labeled cells. The motivation of the study, fundamental background theories and the experimental results and analysis are discussed. Lastly, challenges and possible strategies to improve the technique are presented.

5.1 Motivation of the study

Identification of the nature of a diseased condition requires high sensitivity and reliability. This controls the spread of the disease [81, 82], which enables timely treatment that will significantly improve survival rates. For example, the 5-year survival rate for early-stage, localized breast cancer reaches nearly 100%, whereas that at the metastatic stage is only 26% [83]. In the case of contagious diseases, including acquired immune deficiency syndrome (AIDS), an early diagnosis also effectively prevents the spread of the disease [84].

A variety of technologies have been developed in order to provide early diagnosis with accuracy and molecular specificity. Currently, a molecule-specific cellular diagnosis is usually accomplished via optical labeling [85, 86, 87, 88] and magnetic labeling [89, 90, 91, 92]. Optical technique is very well developed because of its high sensitivity, but it requires a transparent environment. Compared with optical labeling, magnetic labeling has better biocompatibility and less toxicity, and it can be applied in opaque conditions, including in vivo settings.

For magnetic-based techniques to compete with optical-based techniques, three important factors must be considered namely, sensitivity, spatial resolution, and molecular specificity.

As mentioned in the previous chapter, there are three main types of magnetic devices that impart ultrahigh sensitivity: superconducting quantum interference devices (SQUIDs) [93, 94, 95], giant magneto-resistive (GMR) sensors [8, 96], and atomic magnetometers [14, 32, 42]. Other devices with lower sensitivity have also

been used [97, 98, 99]. Because of technological advances, atomic magnetometers have been able to reach high sensitivity that is comparable to that of SQUID devices; both magnetometers can reach the low $\text{fT}/\text{Hz}^{1/2}$ range for ac magnetic fields and tens of $\text{fT}/\text{Hz}^{1/2}$ for dc magnetic fields. One major advantage of atomic magnetometers over SQUID devices and GMR sensors is its operation without the need for a bulky and expensive cryogenic system. GMR sensors at room temperature are significantly less sensitive than cryogen-cooled ones. Using atomic magnetometers, the detection of a single cobalt particle at a detection distance of ~ 2.5 mm was recently achieved [44]. However, the lower limit of detection of magnetically labeled molecules has generally been limited to 10^4 to 10^5 molecules [100].

To image magnetic particles with high spatial resolution, various methods have been demonstrated. A tomographic image has been obtained using the nonlinear response of magnetic particles by Gleich and co-workers [101]. Recently, Goodwill and Conolly [102] demonstrated a novel approach of multidimensional x-space imaging that achieved sub-millimeter spatial resolution. We reported a scanning magnetic imaging scheme using an atomic magnetometer [9]. In this scheme, scanning the sample across the magnetometer produced a magnetic-field profile. The quantity of the magnetic particles and the spatial information were obtained by fitting the magnetic-field profile according to dipolar magnetic field distribution. For well-separated samples, the spatial resolution reached $20 \mu\text{m}$ at a detection distance of approximately 8 mm [43]. A longer detection distance will be desired for in vivo diagnostics in the near future and will hopefully be combined with better sensitivity.

The third parameter to be considered is molecular specificity, which is the resolving of magnetic signals from different molecules. Optical techniques can distinguish molecular entities based on the wavelength of light. Compared to optical detection, magnetic-based methods do not have a similar parameter to distinguish molecular entities. As a consequence, magnetic-based techniques cannot provide quantitative description of the target biomarkers unless excessive sample separation is employed. The separation and purification process is labor-intensive, expensive, and sometimes infeasible. Another challenge is the presence of multiple biomarkers associated with a single disease, which requires a simultaneous quantitative detection of multiple biomarkers for diagnosis [103]. This requirement is a challenge for the current magnetic-based techniques. Recently, we reported a force-induced remnant magnetization spectroscopy (FIRMS) technique that used a shaking force to distinguish the physisorbed receptor molecules from those bound via a specific interaction [10]. This technique is based on the dissociation of magnetically labeled molecules; these dissociated molecules undergo Brownian motion and consequently have no measurable magnetic signal. Therefore, the measured magnetization represents only the quantity of the bound molecules. We have performed a proof-of-principle study in which magnetic particles specifically bound to human CD3⁺ T cells were detected and resolved from a background of physisorbed magnetic particles. No quantitative correlation between the quantity of cells and the number of specifically bound magnetic particles were discussed, and this feature is required for the techniques use in diagnostics.

It is for these reasons that this study was conducted. Improvements on sensitivity, a high spatial resolution at a longer detection range, and quantitative cell specificity were made. Human CD4⁺ T cells are measured by labeling them with CD4 antibody-conjugated magnetic particles. The count of this cell type in blood serves as an indicator for HIV infection. A well-established criterion for HIV infection is a blood count of this cell type below 200 cells/ μ L [104]. We show that the number of specifically bound magnetic particles matches the number of cells.

5.2 Magnetic properties of nanoparticles

In magnetic particle sensing, we can consider the magnetization of a sphere.

$$B(m, r) = \frac{\mu_0}{4\pi r^3} (3\hat{r}(m \cdot \hat{r}) - m). \quad (5.1)$$

It is well-known that a uniformly magnetized sphere is described as a dipole at the center of the sphere. Because of the r^{-3} dependence of the magnetic field, it is important that the instrument to be used has enough sensitivity at a given distance to detect the magnetization.

The core of magnetic nanoparticles is iron oxide. The iron atom has a strong magnetic moment because of its four unpaired electrons in the 3d orbital. When crystal is formed from iron cations, different states can occur. A paramagnetic state is obtained when each magnetic moment is randomly aligned to each other, resulting in a zero net magnetic moment. Upon application of external magnetic field, some spins will align with it and a small net magnetic moment is obtained. For ferromagnetic

crystal, all the magnetic moments are parallel to each other even without external field. In the following subsections, paramagnetism and ferromagnetism are discussed in more detail.

5.2.1 Paramagnetism

Paramagnetic systems contain atomic or molecular orbitals with exactly one electron in them. According to Pauli's principle, spin magnetic moments need to be pointing in opposite directions in order to cancel out magnetic fields. However, an unpaired electron is free to align its magnetic moment in any direction. Therefore, the spins in a paramagnetic system do not tend to interact with one another. These non-interacting spins obey the ideal Curie law:

$$M = \chi \mathbf{H} = \frac{C}{T} \mathbf{H} \quad (5.2)$$

where M is the resulting magnetization, χ is the magnetic susceptibility, H is the auxiliary magnetic field, measured in amperes/meter, T is absolute temperature, measured in Kelvins, and C is a material-specific Curie constant.

Curie's law is only valid at low magnetization levels, since at high-field/low-temperature regime, magnetization is saturated and all the magnetic dipoles are aligned with the external field. No further alignment occurs at much higher external field, therefore the total magnetization will not increase.

Quantum mechanically, paramagnetism can be explained by considering a signal

magnetic moment \mathbf{m} given as:

$$\mathbf{m} = g\mu_B \frac{\mathbf{J}}{\hbar} \quad (5.3)$$

where g is the Landé factor, μ_B is Bohr's magneton, \hbar is the reduced Planck's constant, and \mathbf{J} is the total quantum mechanical angular momentum. When an external magnetic field is applied along the z-axis, the magnetic moment z-component becomes quantized:

$$m_z(j_z) = g\mu_B \frac{J_z}{\hbar} = g\mu_B j_z \quad (5.4)$$

where j_z is the total angular momentum quantum number, which distinguishes the discrete states $2J + 1$. The absolute potential energy of magnetic moment is

$$E = m_z(j_z)\dot{B} \quad (5.5)$$

where B is external field. Therefore, energy splitting occurs when $B \neq 0$. The energy levels are occupied according to Boltzmann statistics:

$$\langle m_z \rangle = g\mu_B \langle j_z \rangle = \frac{g\mu_B}{Z} \sum_{j_z=-J}^{j_z=+J} j_z e^{-\frac{m_z(j_z)B}{kT}} \quad (5.6)$$

where Z is the partition function

$$Z = \sum_{j_z=-J}^{j_z=+J} e^{-\frac{m_z(j_z)B}{kT}} \quad (5.7)$$

and k is the Boltzmann constant. Manipulation of Equation 5.5 leads to the quantum mechanical Brillouin function $\mathbf{B}_J(B, T)$:

$$\langle m_z \rangle = g\mu_B J \mathbf{B}_J(B, T). \quad (5.8)$$

5.2.2 Superparamagnetism

When single magnetic moments can be considered as classic magnetic dipoles based on the Curie limit of paramagnetism, the system is commonly called superparamagnetic. To fully define superparamagnetism, two mechanisms namely Néel and Brown relaxation, need to be distinguished.

In Néel's relaxation theory, a mechanically fixed single-domain (region in the crystal with uniform magnetization, (Figure 5.1) is considered to have angular momentums coupled to each other. This results in a *giant* magnetic moment that is rigidly bound by one or more of the possible anisotropies within the material the particle is made of. For big particles, this anisotropy has very high energy compared to magnetic or thermal energies. However, the anisotropical energy changes rapidly with the volume of the particle. When the volume is decreased, a critical barrier is overcome; the thermal energy kT is high enough to flip the magnetic moment. The Néel relaxation time $\tau_N(E_{AI}/kT)$ ($\simeq 10^{-9}s$) is a measure of the random flipping of the giant magnetic moment within a mechanically fixed particle. When the particles' diameter is below 3 to 50 nm, magnetization can randomly flip direction under the influence of temperature. In the absence of external magnetic field, when the time used to measure the magnetization of the nanoparticles is much longer than the Néel relaxation time, their magnetization appears to be in average zero. In this state, an external magnetic field is able to magnetize the nanoparticles, similarly to a paramagnet. However, their magnetic susceptibility is much larger than the one of paramagnets.

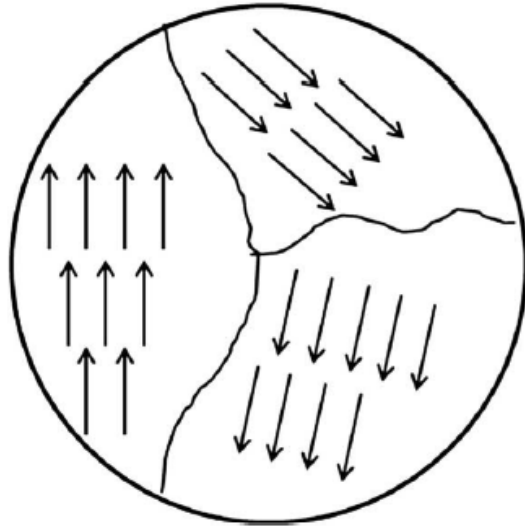


Figure 5.1: Magnetic domains in a bulk material.

Magnetic nanoparticles are typically suspended in a liquid for most applications. In these cases, superparamagnetism is rotated mechanically via the Brownian movement. Since the force counter to Brownian rotation is hydrodynamic, Brownian relaxation time depends on thermal energy, particle volume and the liquid carrier's viscosity. For water or kerosene as solvent, τ_B is on the order of 10^7 s .

5.2.3 Ferromagnetism

Ferromagnetic materials have a net magnetic moment in the absence of external magnetic field. All magnetic ions must contribute positively to the net magnetization for a material to be considered as ferromagnetic. This is to distinguish them from ferrimagnetic and antiferromagnetic materials. If some of the magnetic ions subtract from the net magnetization (if they are partially anti-aligned), then the material is ferrimagnetic. If the ions anti-align completely so as to have zero net magnetization,

despite the magnetic ordering, then it is an antiferromagnet. All of these alignment effects only occur at temperatures below the Curie temperature (for ferromagnets and ferrimagnets) or the Néel temperature (for antiferromagnets). The dependence

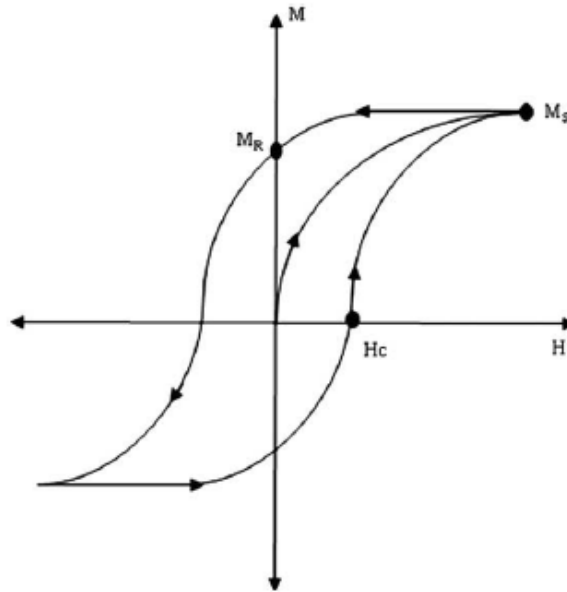


Figure 5.2: Magnetization as a function of applied magnetic field on a ferromagnetic system.

of magnetization of a ferromagnet to an external magnetic field of strength H is shown in Figure 5.2. From the figure, it can be seen that the increase is nonlinear until a saturation value M_s is reached. When H is decreased after the saturation point, the domains do not return to their original orientations. This creates a hysteresis loop in the magnetization curve. When the H turns zero, the system cannot be fully demagnetized unless a field H_c with an opposite direction to the initially introduced field is applied. For materials with single domain, hysteresis loop is not observed and the system is referred to as superparamagnetic. At room temperature, iron oxide

nanoparticles smaller than about 20 nm are classified as superparamagnets.

5.3 Specific biomedical applications of magnetic nanoparticles

Iron oxide in the form of Fe_3O_4 has been widely used in biomedical applications because of their biocompatibility and low toxicity in the human body [105, 106, 107, 108]. Functionalized particles have been associated with drug delivery to a desired target for medication [109, 110]. This requires a minimum dosage, which reduces any adverse effect of the drugs [110]. For drug delivery, nanoparticles are functionalized with drugs, proteins, and genetic materials and serve as therapeutic agents [109, 111].

In-vitro bio-assays have been the major area of application where nanoparticles have been explored [105, 112]. Wang and co-workers [113] used ferromagnetic sensors to detect binding of target DNA and proteins, resulting in an extremely sensitive magnetic microarrays.

Superparamagnetic iron oxide (SPION) has been used in vivo as MRI contrast agents for molecular and cellular imaging. [105, 106, 114]. The surface of SPION particles generally have a polysaccharide layer for colloidal stability [115]. These functionalized particles have been in used in a whole variety of application such as cell separation, protein purification, environment and food analyses, organic and biochemical syntheses, industrial water treatment, and biosciences [116]. The organic polymers basically enhance the stability, dispersability, and functionality of magnetic

nanoparticles [108].

Another application of iron oxide particles is hyperthermia in cancer therapy. Using SPION in a magnetic field, tumor cells can be heated to 41 to 45 °C, in which cancerous tissues are irreversibly damaged while causing a reversible damage to normal tissues [109].

5.4 Cell-binding interactions

For the cell-binding study, we specifically used human CD4 T-cells and streptavidin-coated magnetic particles which were both obtained commercially. In this section, we discuss the interactions present in the system.

CD4 or cluster of differentiation 4 is a glycoprotein that is a member of the immunoglobulin superfamily. Normally, about 65% of T cells in the blood are CD4+ (have CD4 protein attached on their membrane). The extracellular segment has four "domains", which are the bulk of the protein. Together, these make up the first 371 amino acids in the protein. The portion that is on the transmembrane section is amino acids 372 through 395, and the cytoplasmic section (the bit that lies on the inside of the cell) is amino acids 396-433 (Figure 5.3). The CD4 protein has two different regions namely, variable immunoglobulin (IgV) and constant immunoglobulin(IgC), which identifications are based on the variability in the amino acid sequences. D₁ and D₂ resemble IgV, while D₃ and D₄ resemble IgC [117].

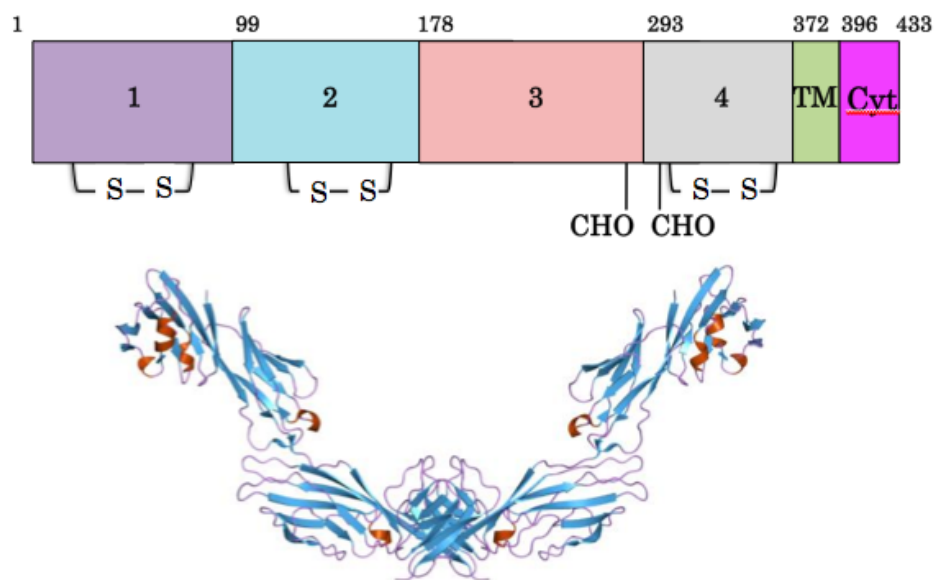


Figure 5.3: Structure of CD4. The four domains are numbered. CHO are glycosylation sites. TM is transmembrane segment; Cyt is the cytoplasmic portion.

In our particular study, T-cells are first combined with the antibody, which contains a DSB-X conjugated monoclonal mouse anti-human CD4. DSB-X biotin is a derivative of desthiobiotin, a stable biotin precursor (Figure 5.4) that has the ability to bind biotin-binding proteins, such as streptavidin and avidin. The magnetic particles used are coated with modified streptavidin. The binding between streptavidin and biotin has a dissociation constant (K_d) on the order of $\simeq 10^{14}$ mol/L and is one of the strongest non-covalent interactions known in nature. The streptavidin-biotin complex has high affinity because of the presence of high shape complementarity between the binding pocket and biotin. There also exists an extensive network of hydrogen bonds formed to biotin when in the binding site. This is called the first shell. The second shell of hydrogen bonding involves residues that interact with the

first shell protein residues. There are also hydrophobic pockets, where a lot of van der Waals and hydrophobic interactions are present. Lastly, biotin binding stabilizes strands, which closes over the bound biotin.

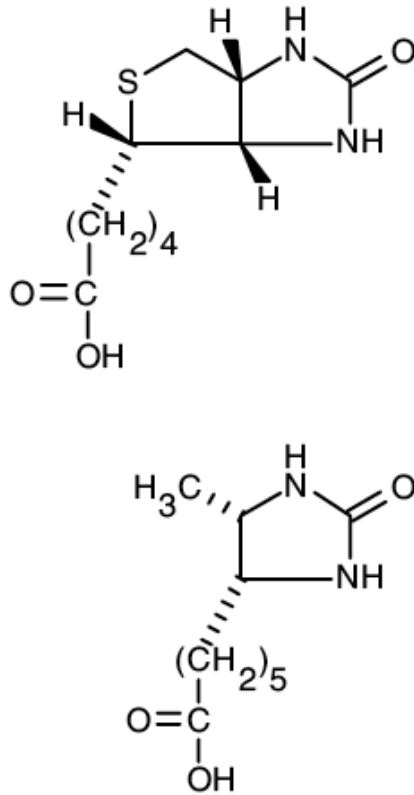


Figure 5.4: Comparison between D-biotin (top) and D-desthiobiotin(bottom).

5.5 Experimental section

5.5.1 Scanning magnetic imaging

Streptavidin-coated ferromagnetic particles (Spherotech, 4-5 μm overall diameter) were used. A piece of capillary tubing containing 50 nL of the sample was glued to a glass slide. From the particle density of $\sim 1.4 \times 10^8$ particles/mL, we calculated the number of particles in this sample to be 7.0×10^3 .

The sample was scanned across by the atomic sensor using a linear transducer (Ultra Motion) with a scanning speed of 1 mm/s. The magnetic fields as a function of the scanning dimension were obtained by the atomic sensor (Trial 1). Next, the sample and the transducer were moved 0.500 mm away from the sensor by a translation stage (Thorlabs) so that the distance between the sample and the sensor became 0.500 mm longer. The magnetic-field profile was measured when the sample was scanned again (Trial 2).

5.5.2 Cell binding

A vial of human CD4+ T cells (20 mL, ca. 6.46×10^7 cells, Innovative Research) was washed with 2 mL isolation buffer (0.1% BSA, 2 mM EDTA in phosphate buffered saline at pH 7.4) and then centrifuged at $350 \times g$ for 8 min. The cells were re-suspended in 3 mL isolation buffer. From the new suspension, 500 μL was incubated with 25 μL antibody at 2-8 $^\circ$ for 10 min. The mixture was washed with isolation buffer, centrifuged, and re-suspended in 50 μL isolation buffer. Streptavidin-coated

magnetic particles (Invitrogen, Dynabeads, 2.8 μm) were introduced to the T cells. To a $4 \times 2 \times 1 \text{ mm}^3$ (L \times W \times H) sample well with glass sides and a polycarbonate bottom, 4 μL of the antibody-cell suspension was added. The cells effectively adhered to the polycarbonate surface. An equal volume of magnetic particle solution was added. The original concentration was 15 mg/mL, corresponding to 10^9 particles per mL. The sample well was covered with a glass cover slip and was incubated in a wet chamber at room temperature for 8 hours. A vortex mixer (VWR, 945303) was used to apply mechanical force onto the system. The force was controlled by adjusting the shaking speed. The sample was shaken for 5 minutes before each measurement. As a comparison, a blank experiment was performed in which no cells but only magnetic particles were present in the sample well.

5.6 Results and discussion

5.6.1 Spatial resolution

The scanning configuration is illustrated in Figure 5.5a, in which the d-axis is the detection axis of the magnetometer, determined by the direction of B_0 , and the x-axis is the scanning axis. The magnetic field profiles of the sample are shown in Figure 5.5b for the two trials with the difference in d of 0.500 mm. The profiles are well described by Yao and Xu [100]:

$$B = \frac{\mu_0 M}{4\pi((x - x_i)^2 + d^2)^{3/2}} \left(\frac{3ad^2}{(x - x_i)^2 + d^2} + 3\sqrt{1 - a^2} \frac{(x - x_i)d}{(x - x_i)^2 + d^2} - a \right) \quad (5.9)$$

Here, B is the measured magnetic field, M is the sample magnetization, d is

the distance along the detection axis, the detection axis is perpendicular to the x-axis, a is equal to $\cos\theta$, where θ is the angle between the magnetic orientation of the corresponding sample and the d-axis. By fitting the profile, we obtain both the magnetization and thus, the quantity of the magnetic particles, and the spatial information. Using Equation 5.9, we obtained the magnetization values and the dimensions of the d- and x-axes, which are listed in Table 5.1. The reduced amplitude in Trial 2 (red trace) was caused by the larger distance between the sample and the sensor. Because the two scans were performed for the same sample, the magnetization (M) values should be the same. As shown in Table 5.2, the difference between the two M values is well within the experimental error. The difference in d values is 0.508 mm, which is consistent with the 0.500 mm movement measured by a translation stage. These results show that the distance information and the quantity of the magnetic particles can be determined with the detection distance extended to more than 1 cm, which is a much longer distance than that in our previous work. The two x values are also consistent with each other [100].

Parameter	Trial 1	Trial 2	Difference
$M(10^{-9}Am^2)$	3.92 ± 0.02	3.93 ± 0.02	0.01
$d(mm)$	10.167 ± 0.016	10.675 ± 0.015	0.508
$x(mm)$	162.22 ± 0.02	162.32 ± 0.02	0.10

Table 5.1: The results of fitted parameters in scanning magnetic imaging

From the signal amplitude, we can estimate the detection limit of this type of magnetic particle. The magnetic signal of 650 pT, the peak value of the profile of Trial 1, corresponds to $\sim 7 \times 10^3$ particles. Therefore, a single particle will produce a field of 93 fT at a distance of 1 cm, which is higher than the 80 fT/Hz^{1/2} sensitivity

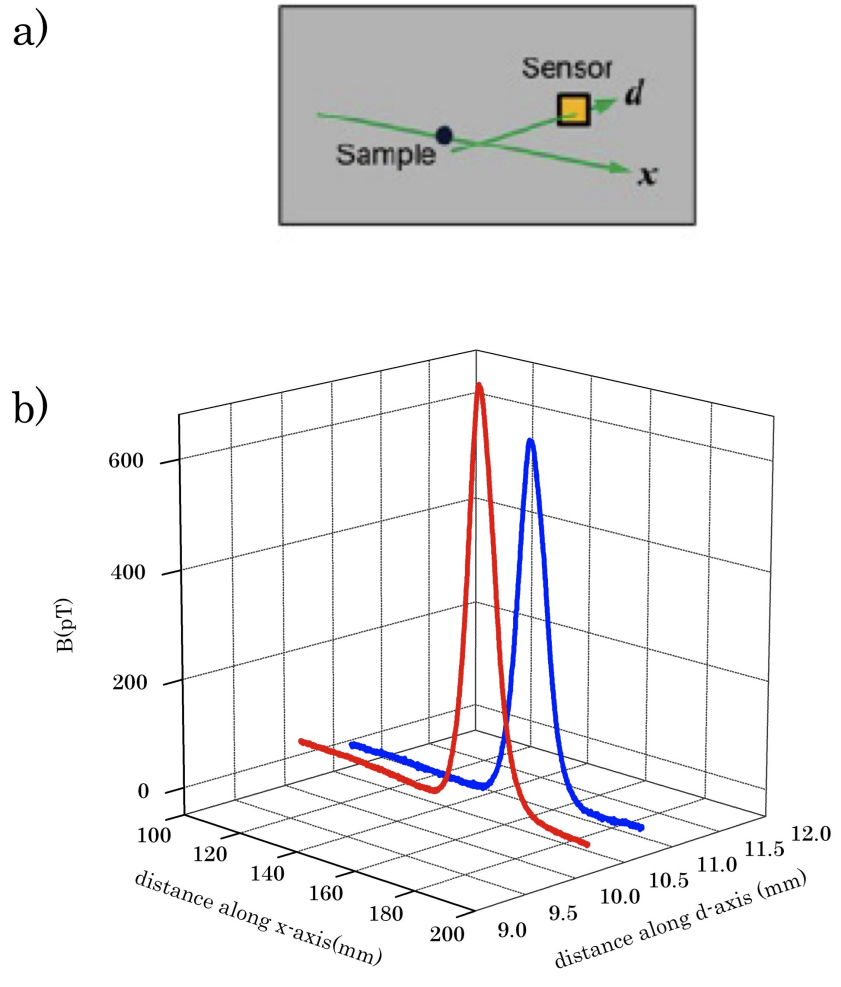


Figure 5.5: a. Scanning configuration for magnetic particle detection. b. Magnetic field profiles for two trials at different d values.

determined. This means that the detection limit of a single such particle can be achieved using 1 s measuring time. The substantial improvement in the detection limit compared with the previous limit of magnetic particle detection is attributable to two factors: one is the improved sensitivity and the other is the stronger magnetization of the magnetic particles used in this work. The excellent detection limit at a long detection distance is a major advantage for magnetic sensing over optical methods.

5.6.2 Specificity

The results for detecting magnetically labeled human CD4⁺ T cells are shown in Figure 5.6. When there is no external force, the initial magnetization values are the same for both the cell-binding experiment (red trace) and the blank (blue trace) at $1.61 \times 10^{-9} \text{ Am}^2$ because the amounts of magnetic particles are identical in both experiments. Upon the application of an external force by shaking at 1500 rpm, the magnetization was reduced to zero in the blank experiment. This reduction is interpreted as the dissociation of the physisorbed magnetic particles; the Brownian motion of the dissociated particles randomized their magnetic orientation and thus resulted in a zero overall magnetic field. In the cell-binding experiment, the magnetization also initially decreased at 1500 rpm, but stabilized at $1.01 \times 10^{-9} \text{ Am}^2$ once 2000 rpm had been reached. This value corresponds to the magnetization of magnetic particles that were specifically bound to cells via the CD4 antibody. We can calculate the number of specifically bound magnetic particles and compare it with the number of cells. The total number of magnetic particles is 1.7×10^6 , which

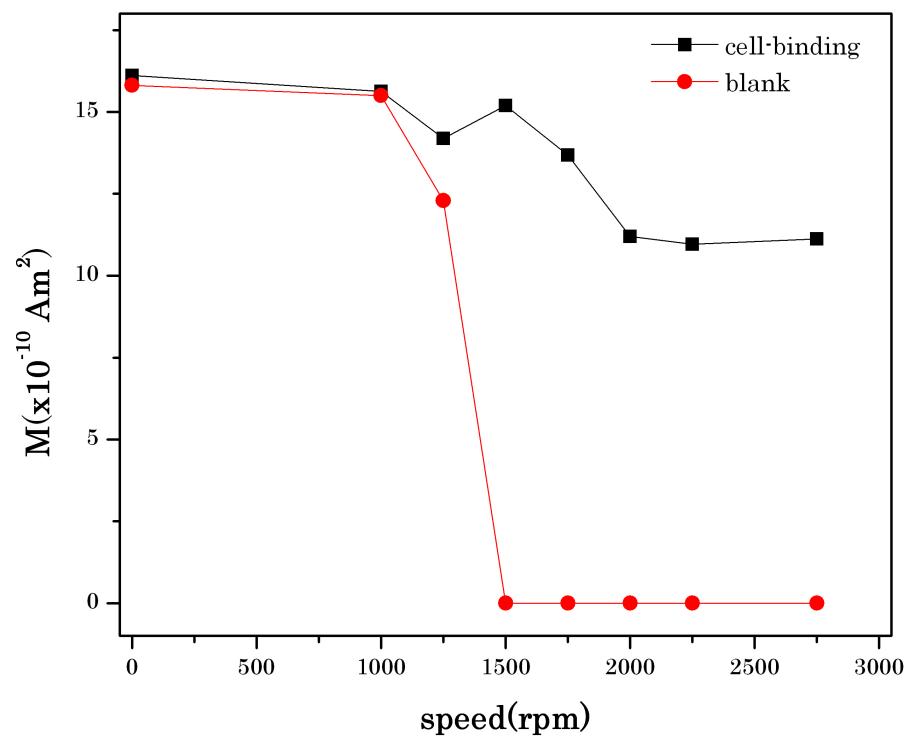


Figure 5.6: FIRMS profile for magnetically labeled CD4 cells.

corresponds to the initial magnetization value of $1.61 \times 10^{-9} \text{ Am}^2$. Therefore, the quantity of bound particles should be

$$1.7 \times 10^6 \times \frac{1.01 \times 10^{-9}}{1.61 \times 10^{-9}} = 1.1 \times 10^6. \quad (5.10)$$

From the experimental parameters, we can estimate the number of cells in the sample well to be 9×10^5 . Given an estimated uncertainty of 10% during both the loading of the cells and the magnetic particles into wells, the number of specifically bound magnetic particles agrees well with the number of cells. This agreement indicates that, on average, one magnetic particle binds to one cell. This result gives a reliable correlation for identifying the quantity of cells, an unknown in diagnostic applications, from the number of specifically bound magnetic particles.

To diagnose HIV with the current apparatus, stronger magnetic particles conjugated with CD4 antibody are required. For example, particles similar to the ones used in the scanning magnetic imaging may be functionalized for diagnostic purposes. By doing so, we achieved a signal-to-noise ratio of 120 with a 50 Hz detection bandwidth, taking into account all the noise associated with sample handling. This result suggests that we can measure 600 particles at a fairly fast detection rate without any modification of the present setup. Considering that the current criterion for HIV infection of a CD4⁺ T cell blood count is below 200 cells/ μL and our sample well holds 4 μL blood, it is clear that the current apparatus will be sufficient for this purpose.

We can compare our approach with other techniques. Flow cytometry, which efficiently counts individual cells, is generally considered the golden standard for

cellular analysis [118]. The advantages of our approach are reflected in two aspects. First, for in vitro analysis, we do not require a large fluid volume, which could be expensive, hazardous, and difficult to obtain. Thus, our approach includes easier sample handling and is cheaper. Second, magnetic sensing can potentially be applied to in vivo analysis, while flow cytometry is strictly an in vitro method.

Another technique with a long detection range and excellent spatial resolution is magnetic resonance imaging (MRI) [89]. It relies on the difference in the nuclear magnetic relaxation induced by the magnetic nanoparticles, which leads to its poor sensitivity. Furthermore, the quantification is complicated by the pulse sequences, and MRI is expensive. One advantage of MRI, however, is that it can be coupled with magnetic resonance spectroscopy to reveal specific molecules that are not labeled. Compared to MRI, our approach provides sensitive magnetic detection by directly sensing the signal from the magnetic nanoparticles. We use pulse sequences that are rather simpler, which allows quantitative analysis to be done with ease. And as mentioned in the previous chapters, atomic magnetometer is relatively cheaper than conventional MRI since it does not require a superconducting magnet and a cryogenic system for operation.

Lastly, optically based, label-free techniques, such as stimulated Raman scattering [119] and microfluidic-based optical microscopy [120], are highly sensitive and specific, but may be limited by the penetration depth of the light source into the opaque samples. Our approach overcomes this limitation since magnetic fields can penetrate through opaque systems.

Chapter 6

Conclusions

In this work, applications of atomic magnetometry in magnetic resonance imaging (MRI) and magnetic molecular sensing were demonstrated. Detection of magnetic field was based on nonlinear magneto-optical rotation, in which a linearly polarized, frequency-modulated light was used for pumping and probing. Cesium was chosen as the alkali sensor because of its sensitivity even at lower temperature conditions. The sensitivity achieved was $150 \text{ fT/Hz}^{1/2}$. The optimum temperature was found to be 37°C , which is highly suitable for biomedical applications. Magnetic resonance studies were carried out using the remote detection scheme, while magnetic particle sensing was done with a scanning technique and force-induced remnant magnetization spectroscopy (FIRMS).

For MRI studies, the magnetization signal from water both in pure and paramagnetic conditions were measured. Using a 180° pulse at $\simeq 1.75 \text{ kHz}$, the highest magnetization signal from pure water was found to be 28.5 pT , which is better

than previous work [5] by a factor of 6. To demonstrate the application of atomic magnetometry in pH contrast, the pH response of gadolinium triethylenetriamine hexaacetic acid $\text{Gd}(\text{TTHA})^{2-}$ from pH 6 to 8.5 was examined. Results showed a pH response of 0.6 s⁻¹ mM⁻¹ per pH unit at ambient magnetic field, which was slightly higher than the value in high magnetic fields. As a comparison, the commonly used gadolinium diethylenetriamine pentaacetic acid $\text{Gd}(\text{DTPA})^{2-}$ was also examined and found to have a non-monotonic response in this pH range. By directly measuring the relaxation of longitudinal magnetization using a stopped-flow scheme, the relaxation times and hence the relaxivity were obtained. Based on the results, $\text{Gd}(\text{TTHA})^{2-}$ could serve as a pH probe at concentrations as low as 50 μM , which is more than one order of magnitude lower than the concentrations used in present magnetic resonance imaging. Using remote detection of MRI in ambient magnetic field, we demonstrated that spatially resolved pH could be achieved.

For magnetic particle detection, factors such as sensitivity, spatial resolution and molecular specificity were put into consideration. For enhanced sensitivity, a different configuration of the magnetometer was designed and built. A divider was used to separate the sample region from the detection region. This arrangement increased the sensitivity by a factor of two (80 fT/Hz^{1/2}), which was attributed to a decrease in noise caused by air flow, more compact optical layout and increased filling factor. Using 7000 streptavidin-coated magnetic particles, a magnetization of 650 pT was obtained, predicting the applicability of atomic magnetometry in single particle detection. Results also showed the capability of the instrument in obtaining spatial information even at long detection range. With a detection distance of more than 1

cm, the spatial resolution was found to be $20 \mu\text{m}$. Coupled with force-induced remnant magnetization spectroscopy, the magnetometer also demonstrated its capability in providing molecular specificity. By measuring the magnetization that is due to the specific binding of conjugated magnetic particles to human CD4 cells, quantitative correlation between the amount of magnetic particles and the number of cells on the surface was achieved.

One of our major goals is to make the whole device more portable and more accessible. Therefore, miniaturization of the magnetometer is an important consideration for future work. One way to carry out this task is to miniaturize or eliminate the magnetic shield completely, since its size is much bigger than the sensors. Although methods have already been reported [74, 75], the sensitivity still needs to be improved by a significant factor. One way to improve the sensitivity of the instrument is by setting up a multiple-pass arrangement of the beam. This will allow the beam to interact with Cs atoms longer and therefore result in a higher optical-rotation at low field. This technique will require a system of mirrors intricately put together to align the beam efficiently.

To expand the application of atomic magnetometry in magnetic resonance imaging, pH studies can be extended to two-dimensional imaging of phantom and biological systems. The effect of ions and other parameters such as temperature, enzymatic activity and partial pressure of oxygen on the relaxation effect of other gadolinium chelates can also be studied.

For magnetic molecular sensing, an ultimate goal is to perform measurements on human subjects in vivo. This means the detection distance must be approximately

10 cm, which is a factor of 10 greater than our current value. This requires that sensitivity be improved by 1000-fold because of the d^{-3} dependence of the magnetic signal. To fulfill this condition, a larger atomic sensor would be helpful because the limit on the sensor dimension is also increased. For example, a recent report demonstrated a sensitivity of $0.16 \text{ fT}/\text{Hz}^{1/2}$ using a spin-exchange relaxation-free (SERF) technique [121]. Although such sensitivity has not been achieved for the dc magnetic signal, this result shows the potential to further improve the sensitivity and thus reduce the detection limit of magnetically labeled cells.

Bibliography

- [1] P. H. Kuo, E. Kanal, A. K. Abu-Alfa, Cowper, and S. E. Gadolinium-based MR contrast agents and nephrogenic systemic fibrosis1. *Radiology*, 242(3):647–649, March 2007.
- [2] S. K. Lee, M. Mößle, W. Myers, N. Kelso, A. H. Trabesinger, A. Pines, and J. Clarke. SQUID-detected MRI at 132 microT with T1-weighted contrast established at 10 microT-300 mT. *Magnetic Resonance in Medicine*, 53(1):9–14, 2005.
- [3] I.M. Savukov and M.V. Romalis. NMR detection with an atomic magnetometer. *Physical Review Letters*, 94(12):123001–1–123001–4, 2005.
- [4] I.M. Savukov, S.J. Seltzer, and M.V. Romalis. Detection of NMR signals with a radio-frequency atomic magnetometer. *Journal of Magnetic Resonance*, 185(2):214 – 220, 2007.
- [5] S. Xu, V. V. Yashchuk, M. H. Donaldson, S. M. Rochester, D. Budker, and A. Pines. Magnetic resonance imaging with an optical atomic magnetometer. *Proceedings of the National Academy of Sciences USA*, 103(34):12668–12671, 2006.
- [6] D. Rugar, R. Budakian, H. J. Mamin, and B.W. Chui. Single spin detection by magnetic resonance force microscopy. *Nature*, 430:329–332, 2004.
- [7] U. Kaiser, A. Schwarz, and R. Wiesendanger. Magnetic exchange force microscopy with atomic resolution. *Nature*, 445:522–525, 2007.
- [8] M. Pannetier, C. Fermon, G. Le Goff, J. Simola, and E. Kerr. FemtoTesla magnetic field measurement with magnetoresistive sensors. *Science*, 304(5677):1648–1650, 2004.
- [9] L. Yao and S. Xu. Long-range, high-resolution magnetic imaging of nanoparticles. *Angewandte Chemie International Edition*, 48(31):5679–5682, 2009.

- [10] L. Yao and S. Xu. Force-induced remnant magnetization spectroscopy for specific magnetic imaging of molecules. *Angewandte Chemie International Edition*, 50(19):4407–4409, 2011.
- [11] D. Yu, N. Garcia, and S. Xu. Toward portable nuclear magnetic resonance devices using atomic magnetometers. *Concepts in Magnetic Resonance Part A*, 34A(2):124–132, 2009.
- [12] M. P. Ledbetter, I. M. Savukov, V. M. Acosta, D. Budker, and M. V. Romalis. Spin-exchange-relaxation-free magnetometry with Cs vapor. *Physical Review A*, 77(3):033408–1–033408–7, March 2008.
- [13] J. C. Allred, R. N. Lyman, T. W. Kornack, and M. V. Romalis. High-sensitivity atomic magnetometer unaffected by spin-exchange relaxation. *Physical Review Letters*, 89:130801, September 2002.
- [14] I. K. Kominis, T. W. Kornack, J. C. Allred, and M. V. Romalis. A subfemtotesla multichannel atomic magnetometer. *Nature*, 422(6932):596–599, 2003.
- [15] I. M. Savukov, S. J. Seltzer, M. V. Romalis, and K. L. Sauer. Tunable atomic magnetometer for detection of radio-frequency magnetic fields. *Physical Review Letters*, 95(6):063004–1–063004–4, 2005.
- [16] M.P. Ledbetter, C.W. Crawford, A. Pines, D.E. Wemmer, S. Knappe, J. Kitching, and D. Budker. Optical detection of NMR J-spectra at zero magnetic field. *Journal of Magnetic Resonance*, 199(1):25 – 29, 2009.
- [17] H. Xia, A. Ben-Amar Baranga, D. Hoffman, and M. V. Romalis. Magnetoencephalography with an atomic magnetometer. *Applied Physics Letters*, 89(21):211104–1–211104–3, 2006.
- [18] M. P. Ledbetter, V. M. Acosta, S. M. Rochester, D. Budker, S. Pustelny, and V. V. Yashchuk. Detection of radio-frequency magnetic fields using nonlinear magneto-optical rotation. *Physical Review A*, 75(2):023405–1–023405–6, February 2007.
- [19] S. Xu, E. Harel, D. J. Michalak, C. W. Crawford, D. Budker, and A. Pines. Flow in porous metallic materials: a magnetic resonance imaging study. *Journal of Magnetic Resonance Imaging*, 28(5):1299–1302, 2008.
- [20] S. Xu, M. H. Donaldson, A. Pines, S. M. Rochester, D. Budker, and V. V. Yashchuk. Application of atomic magnetometry in magnetic particle detection. *Applied Physics Letters*, 89(22):224105, 2006.

- [21] M. Faraday. *Experimental Research*, volume 3. London, 1855.
- [22] D. Macaluso and O. M. Corbino. Sur une nouvelle action subie par la lumière traversant certaines vapeurs métalliques dans une champ magnétique. *Comptes Rendus Hebdomadaires des Séances de l'Académie des Sciences*, 127(548), 1898.
- [23] W. Voigt. *Nachrichten von der Gesellschaft Wissensch zu Gttingen Math-phys. Klasse*, 329, 1898.
- [24] D. Budker, W. Gawlik, D. F. Kimball, S. M. Rochester, V. V. Yashchuk, and A. Weis. Resonant nonlinear magneto-optical effects in atoms. *Review of Modern Physics*, 74(4):51, 2002.
- [25] N. Papageorgiou, A. Weis, V. A. Sautenkov, D. Bloch, and M. Ducloy. High-resolution selective reflection spectroscopy in intermediate magnetic fields. *Applied Physics B: Lasers and Optics*, 59:123–126, 1994.
- [26] W. Gawlik, J. Kowalski, R. Neumann, and F. Träger. Strong narrowing of the na forward scattering signals due to the interaction with an intense dye laser field. *Physics Letters A*, 48(4):283 – 284, 1974.
- [27] L. Allen and J.H. Eberly. *Optical resonance and two-level atoms*. Dover, New York, 1987.
- [28] R. W. Schmieder, A. Lurio, W. Happer, and A. Khadjavi. Level-crossing measurement of lifetime and hfs constants of the $^2P_{3/2}$ states of the stable alkali atoms. *Physical Review A*, 2:1216–1228, October 1970.
- [29] L. M. Barkov, D. A. Melik-Pashayev, and M. S. Zolotorev. Nonlinear faraday rotation in Samarium vapor. *Optics Communications*, 70(6):283 – 284, 1989.
- [30] W. Happer. Optical pumping. *Review of Modern Physics*, 44(2):169 – 250, April 1972.
- [31] Z. Wu, T. G. Walker, and W. Happer. Spin-rotation interaction of noble-gas alkali-metal atom pairs. *Physical Review Letters*, 54:1921–1924, April 1985.
- [32] D. Budker, D. F. Kimball, S. M. Rochester, V. V. Yashchuk, and M. Zolotorev. Sensitive magnetometry based on nonlinear magneto-optical rotation. *Physical Review A*, 62(4):1–7, 2000.
- [33] D. Budker, D. F. Kimball, V. V. Yashchuk, and M. Zolotorev. Nonlinear magneto-optical rotation with frequency-modulated light. *Physical Review A*, 65(5):5, 2002.

- [34] W. Gawlik, L. Krzemien, S. Pustelny, D. Sangla, J. Zachorowski, M. Graf, A. O. Sushkov, and D. Budker. Nonlinear magneto-optical rotation with amplitude modulated light. *Applied Physics Letters*, 88(13):131108–1–131108–3, 2006.
- [35] M. V. Balabas, D. Budker, J. Kitching, P. D. D. Schwindt, and J. E. Stalnaker. Magnetometry with millimeter-scale antirelaxation-coated alkali-metal vapor cells. *Journal of the Optical Society of America B*, 23(6):1001–1006, June 2006.
- [36] D. Budker. Atomic physics: A new spin on magnetometry. *Nature News and Views*, 422(6932):574–575, 2003.
- [37] M. V. Balabas, T. Karaulanov, M. P. Ledbetter, and D. Budker. Polarized alkali-metal vapor with minute-long transverse spin-relaxation time. *Physical Review Letters*, 105(7):070801–1–070801–4, Aug 2010.
- [38] K. L. Corwin, Z. T. Lu, C. F. Hand, R. J. Epstein, and C. E. Wieman. Frequency-stabilized diode laser with the zeeman shift in an atomic vapor. *Applied Optics*, 37(15):3295–3298, 1998.
- [39] V.Y. Yashchuk, D. Budker, and J. R. Davis. Laser frequency stabilization using linear magneto-optics. *Review of Scientific Instruments*, 71(2):341–346, 2000.
- [40] S. Xu, S. M. Rochester, V. V. Yashchuk, M. H. Donaldson, and D. Budker. Construction and applications of an atomic magnetic gradiometer based on nonlinear magneto-optical rotation. *Review of Scientific Instruments*, 77(8):083106–1–083106–8, 2006.
- [41] S.J. Seltzer. *Developments in Alkali-Metal Atomic Magnetometry*. Phd Dissertation, Princeton University, November 2008.
- [42] V. Shah, S. Knappe, P.D.D Schwindt, and J. Kitching. Subpicotesla atomic magnetometry with a microfabricated vapour cell. *Nature Photonics*, 1:649–642, November 2007.
- [43] N. Garcia, L Yu, D. and Yao, and S. Xu. Optical atomic magnetometer at body temperature for magnetic particle imaging and nuclear magnetic resonance. *Optics Letters*, 35(5):661–663, 2010.
- [44] D. Maser, S. Pandey, H. Ring, M. P. Ledbetter, S. Knappe, J. Kitching, and D. Budker. Detection of a single cobalt microparticle with a microfabricated atomic magnetometer. *Review of Scientific Instruments*, 82(8):086112–1–086112–3, 2011.

- [45] M. Möhle, S. Han, W. R. Myers, S. K. Lee, N. Kelso, M. Hatridge, A. Pines, and J. Clarke. SQUID-detected microtesla MRI in the presence of metal. *Journal of Magnetic Resonance*, 179(1):146–151, 2006.
- [46] S. Appelt, H. Kühn, F.W. Häsing, and B. Blümich. Chemical analysis by ultrahigh-resolution nuclear magnetic resonance in the Earth’s magnetic field. *Nature Physics*, 2:105–109, 2006.
- [47] A. Mohorič, G. Planinšič, M. Kos, A. Duh, and J. Stepšnik. Magnetic resonance imaging system based on Earth’s magnetic field. *Instrumentation Science and Technology*, 32:655–667, 2004.
- [48] M.E. Halse, A. Coy, R. Dykstra, C. Eccles, M. Hunter, R. Ward, and P.T. Callaghan. A practical and flexible implementation of 3d mri in the Earth’s magnetic field. *Journal of Magnetic Resonance*, 182:75–83, 2006.
- [49] J. Clarke. *SQUID Sensors: Fundamentals, Fabrication, and Applications*, volume 44. Kluwer Academic, The Netherlands, 1996.
- [50] V. S. Zotey, A. N. Matlashov, P. L. Volegov, I. M. Savukov, M. A. Espy, J. C. Mosher, J. J. Gomez, and R. H. Kraus Jr. Microtesla MRI of the human brain combined with MEG. *Journal of Magnetic Resonance*, 194(1):115 – 120, 2008.
- [51] P. Volegov, A. N. Matlachov, M. A. Espy, J. S. George, and R. H. Kraus. Simultaneous magnetoencephalography and SQUID detected nuclear MR in microtesla magnetic fields. *Magnetic Resonance in Medicine*, 52(3):467–470, 2004.
- [52] R. McDermott, S. Lee, B. Haken, A. H. Trabesinger, A. Pines, and J. Clarke. Microtesla MRI with a superconducting quantum interference device. *Proceedings of the National Academy of Sciences USA.*, 101(21):7857–7861, 2004.
- [53] R. McDermott, A. H. Trabesinger, M. Mück, E. L. Hahn, A. Pines, and J. Clarke. Liquid-state NMR and scalar couplings in microtesla magnetic fields. *Science*, 295(5563):2247–2249, 2002.
- [54] F. Verpillat, M. P. Ledbetter, S. Xu, D. J. Michalak, C. Hilty, L.-S. Bouchard, S. Antonijevic, D. Budker, and A. Pines. Remote detection of nuclear magnetic resonance with an anisotropic magnetoresistive sensor. *Proceedings of the National Academy of Sciences*, 105(7):2271–2273, 2008.
- [55] P. Caravan. Strategies for increasing the sensitivity of gadolinium based MRI contrast agents. *Chemical Society Reviews*, 35(6):512–523, 2006.

- [56] S. Laurent, L. V. Elst, and R. N. Muller. Comparative study of the physicochemical properties of six clinical low molecular weight gadolinium contrast agents. *Contrast Media and Molecular Imaging*, 1(3):128–137, 2006.
- [57] P. Caravan, J. J. Ellison, T. J. McMurry, and R. B. Lauffer. Gadolinium(III) chelates as MRI contrast agents: Structure, dynamics, and applications. *Chemical Reviews*, 99(9):2293–352, 1999.
- [58] J. Granwehr, E. Harel, S. Han, S. Garcia, A. Pines, P. N. Sen, and Y.-Q. Song. Time-of-flight flow imaging using NMR remote detection. *Physical Review Letters*, 95:075503–1–075503–4, August 2005.
- [59] A. J. Moulé, M. M. Spence, S.-I. Han, J. A. Seeley, K. L. Pierce, S. Saxena, and A. Pines. Amplification of xenon NMR and MRI by remote detection. *Journal of Magnetic Resonance*, 100(16):9122–9127, 2003.
- [60] S. Xu, C. W. Crawford, S. Rochester, V. Yashchuk, D. Budker, and A. Pines. Submillimeter-resolution magnetic resonance imaging at the Earth’s magnetic field with an atomic magnetometer. *Physical Review A*, 78(1):013404–1–013404–4, Jul 2008.
- [61] D. Nishimura. *Principles of Magnetic Resonance Imaging*. Dwight Nishimura, 1996.
- [62] J. L. Major and T. J. Meade. Bioresponsive, cell-penetrating, and multimeric MR contrast agents. *Accounts of Chemical Research*, 42(7):893–903, 2009.
- [63] R. van Eldik. *Advances in Inorganic Chemistry: Relaxometry of H₂O interactions*. Elsevier, Netherlands, First edition, 2005.
- [64] M. Lowe. Activated MR contrast agents. *Current Pharmaceutical Biotechnology*, 5:519–528, 2004.
- [65] A. Jasanoff. MRI contrast agents for functional molecular imaging of brain activity. *Current Opinion in Neurobiology*, 17(5):593 – 600, 2007.
- [66] F. A. Gallagher, M. I. Kettunen, D.-E. Day, S. E. and Hu, J. H. Ardenkjær-Larsen, R. int Zandt, P. R. Jensen, M. Karlsson, K. Golman, M. H. Lerche, and K. M. Brindle. Magnetic resonance imaging of pH in vivo using hyperpolarized ¹³C-labeled bicarbonate. *Nature*, 453(7197):940–943, 2009.
- [67] L. M. De Leon-Rodriguez, A. J. M. Lubag, Craig R. Malloy, G. V. Martinez, R. J. Gillies, and A. D. Sherry. Responsive MRI agents for sensing metabolism in vivo. *Accounts of Chemical Research*., 42(7):948–957, 2009.

- [68] E. Pérez-Mayoral, V. Negri, J. Soler-Padró, S. Cerdán, and P. Ballesteros. Chemistry of paramagnetic and diamagnetic contrast agents for Magnetic Resonance Imaging and Spectroscopy: pH responsive contrast agents. *European Journal of Radiology*, 67:453–458, September 2008.
- [69] Y. Wu, T. C. Soesbe, G. E. Kiefer, P. Zhao, and A. D. Sherry. A responsive europium(III) chelate that provides a direct readout of pH by MRI. *Journal of the American Chemical Society*, 132(40):14002–14003, 2010.
- [70] F. K. Kálmán, M. Woods, P. Caravan, P. Jurek, M. Spiller, G. Tircsó, R. Király, E. Brücher, and A. D. Sherry. Potentiometric and relaxometric properties of a gadolinium-based MRI contrast agent for sensing tissue pH. *Inorganic Chemistry*, 46(13):5260–5270, 2007.
- [71] C. A. Chang, H. G. Brittain, J. Telser, and M. F. Tweedle. pH dependence of relaxivities and hydration numbers of gadolinium(III) complexes of linear amino carboxylates. *Inorganic Chemistry*, 29(22):4468–4473, 1990.
- [72] J. Mispelter, M. Lupu, and A. Briguet. *NMR Probeheads for Biophysical and Biomedical Experiments: Theoretical Principles & Practical Guidelines*. Imperial College, London, UK, 2006.
- [73] E. A. Donley, E. Hodby, L. Hollberg, and J. Kitching. Demonstration of high-performance compact magnetic shields for chip-scale atomic devices. *Review of Scientific Instruments*, 78(8):083102–1–083102–7, 2007.
- [74] S.J. Seltzer and M. V. Romalis. Unshielded three-axis vector operation of a spin-exchange-relaxation-free atomic magnetometer. *Applied Physics Letters*, 85(20):4804–4806, 2004.
- [75] V. Acosta, M. P. Ledbetter, S. M. Rochester, D. Budker, D. F. J. Kimball, D. C. Hovde, W. Gawlik, S. Pustelny, and J. Zachorowski. Nonlinear magneto-optical rotation with frequency-modulated light in the geophysical field range. *Physical Review A*, 73(5):053404–1–053404–8, 2006.
- [76] S. J. Seltzer, P. J. Meares, and M. V. Romalis. Synchronous optical pumping of quantum revival beats for atomic magnetometry. *Physical Review A*, 75:051407–1–051407–4, May 2007.
- [77] K. Jensen, V. M. Acosta, J. M. Higbie, M. P. Ledbetter, S. M. Rochester, and D. Budker. Cancellation of nonlinear Zeeman shifts with light shifts. *Physical Review A*, 79:023406–1–023406–5, Feb 2009.

- [78] T. W. Kornack, S. J. Smullin, S.-K. Lee, and M. V. Romalis. A low-noise ferrite magnetic shield. *Applied Physics Letters*, 90(22):223501–1–223501–3, 2007.
- [79] S. K. Lee, K. L. Sauer, S. J. Seltzer, O. Alem, and M. V. Romalis. Sub-femtotesla radio-frequency atomic magnetometer for detection of nuclear quadrupole resonance. *Applied Physics Letters*, 89(21):214106–1–214106–3, 2006.
- [80] P. D. D. Schwindt, B. Lindseth, S. Knappe, V. Shah, J. Kitching, and L-A. Liew. Chip-scale atomic magnetometer with improved sensitivity by use of the M_x technique. *Applied Physics Letters*, 90(8):081102–1–081102–3, 2007.
- [81] W. Debbage, P. and Jaschke. Molecular imaging with nanoparticles: giant roles for dwarf actors. *Histochemistry and Cell Biology*, 130:845–875, 2008.
- [82] D. Margolis. Eradication therapies for HIV infection: Time to begin again. *AIDS Research and Human Retroviruses*, 27(4):347–353, 2011.
- [83] C. Leuschner, C.S.S.R. Kumar, W. Hansel, W.O. Soboyejo, J. Zhou, and J. Hormes. LHRH-conjugated magnetic iron oxide nanoparticles for detection of breast cancer metastases. *Breast Cancer Research and Treatment*, 99(2):163–176, 2006.
- [84] G. d’Ettore, M. Paiardini, G. Ceccarelli, G. Silvestri, and V. Vullo. HIV associated immune activation: From bench to bedside. *Aids Research and Human Retroviruses*, 27(4):355–364, April 2011.
- [85] H. Shi, X. He, K. Wang, X. Wu, X. Ye, Q. Guo, W. Tan, Z. Qing, X. Yang, and B. Zhou. Activatable aptamer probe for contrast-enhanced in vivo cancer imaging based on cell membrane protein-triggered conformation alteration. *Proceedings of the National Academy of Sciences USA*, 108(10):3900–3905, 2011.
- [86] X. Nan, P. A. Sims, and X. S. Xie. Organelle tracking in a living cell with microsecond time resolution and nanometer spatial precision. *Physical Chemistry Chemical Physics*, 9(5):707–712, 2008.
- [87] M. Bates, B. Huang, G. T. Dempsey, and X. Zhuang. Multicolor super-resolution imaging with photo-switchable fluorescent probes. *Science*, 317(5845):1749–1753, September 2007.
- [88] M. V. Yezhelyev, X. Gao, Y. Xing, A. Al-Hajj, S. Nie, and R.M. O’Regan. Emerging use of nanoparticles in diagnosis and treatment of breast cancer. *Lancet Oncol.*, 7(8):657 – 667, 2006.

- [89] J. W. M. Bulte and D. L. Kraitchman. Iron oxide mr contrast agents for molecular and cellular imaging. *NMR Biomedicine*, 17(7):484–499, 2004.
- [90] R. D. K. Misra. Magnetic nanoparticle carrier for targeted drug delivery: perspective, outlook and design. *Materials Science and Technology*, 24(9):1011–1019, September 2008.
- [91] D.R. Leigh, S. Steinert, L.R. Moore, J. Chalmers, and M. Zborowski. Cell tracking velocimetry as a tool for defining saturation binding of magnetically conjugated antibodies. *Cytometry Part A*, 66A(2):103–108, August 2005.
- [92] V. Sivagnanam, B. Song, C. Vandevyver, J-C. G. Bünzli, and M. A. M. Gijs. Selective breast cancer cell capture, culture, and immunocytochemical analysis using self-assembled magnetic bead patterns in a microfluidic chip. *Langmuir*, 26(9):6091–6096, 2010.
- [93] H.E. Horng, S.Y. Yang, Y.W. Huang, W.Q. Jiang, C.-Y. Hong, and H.C. Yang. Nanomagnetic particles for squid-based magnetically labeled immunoassay. *IEEE Transactions on Applied Superconductivity*, 15(2):668 – 671, June 2005.
- [94] L. E. Fong, J. R. Holzer, K. K. McBride, E. A. Lima, F. Baudenbacher, and M. Radparvar. High-resolution room-temperature sample scanning superconducting quantum interference device microscope configurable for geological and biomagnetic applications. *Review of Scientific Instruments*, 76(5):053703–1–053703–9, 2005.
- [95] Y. R. Chemla, H. L. Grossman, Y. Poon, R. McDermott, R. Stevens, M. D. Alper, and J. Clarke. Ultrasensitive magnetic biosensor for homogeneous immunoassay. *Proceedings of the National Academy of Sciences USA*, 97(26):14268–14272, May 2000.
- [96] S. J. Osterfeld, H. Yu, R. S. Gaster, S. Caramuta, S-J. Xu, L. and Han, D. A. Hall, R. J. Wilson, S. Sun, R. L. White, R. W. Davis, N. Pourmand, and S. X. Wang. Multiplex protein assays based on real-time magnetic nanotag sensing. *Proceedings of the National Academy of Sciences USA*, 105(52):20637–20640, 2008.
- [97] D. Baumgarten, M. Liehr, F. Wiekhorst, U. Steinhoff, P. Mnster, P. Miethe, L. Trahms, and J. Haueisen. Magnetic nanoparticle imaging by means of minimum norm estimates from remanence measurements. *Medical and Biological Engineering and Computing*, 46:1177–1185, 2008.

- [98] E. Heim, F. Ludwig, and M. Schilling. Binding assays with streptavidin-functionalized superparamagnetic nanoparticles and biotinylated analytes using fluxgate magnetorelaxometry. *Journal of Magnetism and Magnetic Materials*, 321(10):1628 – 1631, 2009.
- [99] M. Nikitin, M. Yuriev, N. Brusentsov, P. Vetoshko, and P. Nikitin. Non-invasive in vivo mapping and long-term monitoring of magnetic nanoparticles in different organs of animals. *American Institute of Physics Conference Proceedings*, 1311(1):452 – 457, 2010.
- [100] L. Yao, A. C. Jamison, and S. Xu. Scanning imaging of magnetic nanoparticles for quantitative molecular imaging. *Angewandte Chemie International Edition*, 49(41):7493–7496, 2010.
- [101] B. Gleich and J. Weizenecker. Tomographic imaging using the nonlinear response of magnetic particles. *Nature*, 435:1214–1217, June 2005.
- [102] P.W. Goodwill and S.M. Conolly. Multidimensional x-space magnetic particle imaging. *IEEE Transactions on Medical Imaging*, 30:1581–1590, 2011.
- [103] J. B. Haun, C. M. Castro, R. Wang, V. M. Peterson, B. S. Marinelli, H. Lee, and R. Weissleder. Micro-NMR for rapid molecular analysis of human tumor samples. *Science Translational Medicine*, 3(71):1–10, 2011.
- [104] F. Vigneault, M. Woods, M.J. Buzon, C. Li, F. Pereyra, S.D. Crosby, J. Rychert, G. Church, J. Marinez-Picado, E.S. Rosenberg, A. Telenti, X.G. Yu, and M. Lichterfeld. Transcriptional profiling of CD4 T cells identifies distinct subgroup of HIV-1 elite controllers. *Journal of Virology*, 85:3015–3019, 2011.
- [105] P. Majewski and B. Thierry. Functionalized magnetite nanoparticle synthesis, properties, and bio-applications. *Critical Reviews in Solid State and Materials Sciences*, 32(3-4):203–215, 2007.
- [106] P. Tartaj, M. del Puerto Morales, S. Veintemillas-Verdaguer, T. González-Carreño, and C. J. Serna. The preparation of magnetic nanoparticles for applications in biomedicine. *Journal of Physics D: Applied Physics*, 36(13):R182–R197, 2003.
- [107] J. S. Kim, T.-J. Yoon, K. N. Yu, B. G. Kim, S. J. Park, H. W. Kim, K. H. Lee, S. B. Park, J.-K. Lee, and M. H. Cho. Toxicity and tissue distribution of magnetic nanoparticles in mice. *Toxicological Sciences*, 89(1):338–347, January 2006.

- [108] P. Tartaj, M.P. Morales, T. González-Carreño, S. Veintemillas-Verdaguer, and C.J. Serna. Advances in magnetic nanoparticles for biotechnology applications. *Journal of Magnetism and Magnetic Materials*, 290-291, Part 1(0):28 – 34, 2005.
- [109] T. Neuberger, B. Schöpf, H. Hofmann, M. Hofmann, and B. von Rechenberg. Superparamagnetic nanoparticles for biomedical applications: Possibilities and limitations of a new drug delivery system. *Journal of Magnetism and Magnetic Materials*, 293(1):483 – 496, 2005.
- [110] A. S. Lübbe, C. Bergemann, H. Riess, F. Schriever, P. Reichardt, K. Possinger, M. Matthias, B. Dörken, F. Herrmann, R. Gürtler, P. Hohenberger, N. Haas, R. Sohr, B. Sander, A.-J. Lemke, D. Ohlendorf, W. Huhnt, and D. Huhn. Clinical experiences with magnetic drug targeting: A phase I study with 4'-epidoxorubicin in 14 patients with advanced solid tumors. *Cancer Research*, 56(20):4686–4693, 1996.
- [111] N. Kohler, C. Sun, J. Wang, and M. Zhang. Methotrexate-modified superparamagnetic nanoparticles and their intracellular uptake into human cancer cells. *Langmuir*, 21(19):8858–8864, 2005.
- [112] H.-H. Yang, S.-Q. Zhang, X.-L. Chen, Z.-X. Zhuang, J.-G. Xu, and X.-R. Wang. Magnetite-containing spherical silica nanoparticles for biocatalysis and bioseparations. *Analytical Chemistry*, 76(5):1316–1321, 2004.
- [113] S. X. Wang, S.-Y. Bae, G. Li, S. Sun, R. L. White, J. T. Kemp, and C. D. Webb. Towards a magnetic microarray for sensitive diagnostics. *Journal of Magnetism and Magnetic Materials*, 293(1):731 – 736, 2005.
- [114] H. Ai, C. Flask, B. Weinberg, X.-T. Shuai, M. D. Pagel, D. Farrell, J. Duerk, and J. Gao. Magnetite-loaded polymeric micelles as ultrasensitive magnetic-resonance probes. *Advanced Materials*, 17(16):1949–1952, 2005.
- [115] L. Babes, B. Denizot, G. Tanguy, J. J. Le Jeune, and P. Jallet. Synthesis of iron oxide nanoparticles used as mri contrast agents: A parametric study. *Journal of Colloid and Interface Science*, 212(2):474 – 482, 1999.
- [116] A. Teja and Pei-Yoong Koh. Synthesis, properties, and applications of magnetic iron oxide nanoparticles. *Progress in Crystal Growth and Characterization of Materials*, 55(1):22 – 45, 2009.

- [117] S.C. Harrison. CD4: Structure and interactions of an immunoglobulin superfamily adhesion molecule. *Accounts of Chemical Research*, 26(8):449–453, 1993.
- [118] H.M. Shapiro. *Practical Flow Cytometry*. Wiley-Liss, New York, USA, Fourth edition, 2003.
- [119] Br. G. Saar, Y. Zeng, C.W. Freudiger, Y.-S. Liu, M.E. Himmel, X.-S. Xie, and S.-Y. Ding. Label-free, real-time monitoring of biomass processing with stimulated raman scattering microscopy. *Angewandte Chemie*, 122(32):5608–5611, 2010.
- [120] X. Cheng, D. Irimia, M. Dixon, K. Sekine, U. Demirci, L. Zamir, R. G. Tompkins, W. Rodriguez, and M. Toner. A microfluidic device for practical label-free CD4+ T cell counting of HIV-infected subjects. *Lab on a Chip*, 7:170–178, 2007.
- [121] H. B. Dang, A. C. Maloof, and M. V. Romalis. Ultra-high sensitivity magnetic field and magnetization measurements with an atomic magnetometer. *Applied Physics Letters*, 97(15):151110–1–151110–3, 2010.